

DIPLOMARBEIT

---

# One-Dimensional Model for Phonon Wavepacket Propagation in Ferroelectric Solids

---

September 2013

*Author:*  
Matthias GOHLKE  
*Student ID:*  
738602

*Supervisors:*  
Prof. Dr. Matias BARGHEER  
Prof. Dr. Arkady PIKOVSKY



DEPARTMENT OF PHYSICS AND ASTRONOMY  
UNIVERSITY OF POTSDAM

## **Zusammenfassung**

In der vorliegenden Diplomarbeit wird ein eindimensionales Modell für die Propagation von Schallpulsen in Festkörpern, die einen strukturellen Phasenübergang aufweisen, vorgestellt. Ein struktureller Phasenübergang tritt insbesondere bei vielen Ferroelektrika auf. Als Modell wird eine lineare Kette mit zwei Komponenten mit harmonischer Wechselwirkung zwischen übernächsten Nachbarn und anharmonische Wechselwirkung, gegeben durch ein Morse-Potential, zwischen nächsten Nachbarn angenommen. Auf Grund einer symmetrischen Anordnung dieser Morse-Potentiale kommt es zu einem kontinuierlichen Phasenübergang von zwei gleichwertigen Grundzuständen zu einem einzelnen Grundzustand. Desweiteren spiegelt das Modell diverse Eigenschaften von Ferroelektrika und deren Phasenübergang wider. Zum Beispiel können das Auftreten von Domänen in der ferroelektrischen Phase oder das Weichwerden einer optischen Schwingungsmode beim Phasenübergang beobachtet werden.

Der Hauptaspekt liegt auf der Untersuchung der Dynamik. Innerhalb der linearen Theorie werden die Stabilität und die Schwingungsmoden der Kette, als auch die Schallgeschwindigkeit analytisch berechnet. Numerische Simulation erweitern die Untersuchung auf nichtlineare Effekte, wie die zeitliche Veränderung der Pulseform und der Kopplung von verschiedenen Schwingungsmoden. Die letztgenannte Kopplung wird mit Hilfe einer Entropie des räumlichen Fourierspektrums analysiert. Sie kann auch eine Ursache chaotischer Dynamik sein, welche mittels des maximalen Lyapunov Koeffizienten genauer untersucht wird.

## **Abstract**

The thesis to hand investigates phonon propagation in solids exhibiting a structural phase transition with an one-dimensional model. These structural transitions mainly appear in ferroelectric solids with a permanent polarization below the Curie temperature. A two component linear chain with harmonic next-nearest and nearest neighbor interaction by a Morse potential will be introduced. Merging the interactions within one unit cell shows, that either two degenerate or one ground state exist depending on an external parameter. The occurring phase transition is of second order. Furthermore the model reflects properties of ferroelectric solids as for instance domains and the softening of an optical vibration mode.

This thesis focuses mainly on dynamical aspects. The vibration normal modes and the sound velocities will be derived within a linear theory. Numerical simulations will be used to confirm the linear theory, but also to extend the investigations into the nonlinear regime. Nonlinear effects as temporal change of the pulse shape and coupling of vibration modes will be revealed. Finally, strong coupling and nonlinearity give rise to chaotic dynamics, which will be characterized by means of the maximum Lyapunov Exponent. The strong coupling will be studied by an entropy of the spatial Fourier spectrum and its temporal evolution depending on the initial energy density.

# Contents

<b>1</b>	<b>Introduction</b>	<b>1</b>
<b>2</b>	<b>Basics</b>	<b>3</b>
2.1	Lattice Dynamics . . . . .	3
2.2	Ferroelectric Phase Transition . . . . .	7
2.3	Aubry Model . . . . .	12
2.4	Chaotic Dynamics . . . . .	15
<b>3</b>	<b>Model</b>	<b>17</b>
3.1	How to get to a 1D Model? . . . . .	18
3.2	Hamiltonian . . . . .	18
3.3	Ferrodistortion . . . . .	20
3.4	Small Amplitude Solution - Phonon Dispersion Relation . . . . .	28
3.5	Large Amplitude Solution - Domain Wall . . . . .	36
<b>4</b>	<b>Simulating Dynamics</b>	<b>39</b>
4.1	Simulation Procedure . . . . .	39
4.2	Initial Condition . . . . .	40
4.3	Pulse Propagation . . . . .	43
4.4	Numerical Dispersion Relation . . . . .	55
4.5	Lyapunov-Exponent Analysis . . . . .	59
4.6	Mode Interaction . . . . .	61
<b>5</b>	<b>Summary and Outlook</b>	<b>66</b>

# Chapter 1

## Introduction

A lot intriguing phenomena go beyond the linear theory. John Scott Russell did one of the first observations of a nonlinear effect in 1834. He noticed a water wave propagating a long distance without a significant change of its shape. Sixty years went by until a theoretical description was found, the Korteweg-de Vries equation. It shall need more than half a century again, until the real significance of this phenomenon awoke when Kruskal and Zabusky solved the Fermi-Pasta-Ulam problem analytically. They reduce the Fermi-Pasta-Ulam problem to the Korteweg-de Vries equation and got their solitonic solutions. The theory of solitons and solitonic waves was established and found several applications. A famous one is the lossless propagation of a light pulse within a waveguide, a so called envelope soliton, used for data transmission. Solitons can be found in all scales and types in nature: The Pororoca, a water wave, travels several hundred kilometers upstream the Amazonas River. The “Morning Glory Cloud” is a special cloud, which “rolls” about a horizontal axis without changing its size and speed. But solitons can also occur in proteins and DNA as a collective motion of protons, so called Davydov solitons [Dav73, Sco92].

What does that has to do with ferroelectric materials? Ferroelectricity is defined by its non-vanishing polarization. Due to energetic reasons, the whole bulk will not show a homogeneous polarization rather than different domains. Domains are characterized by having a homogeneously distributed polarization. Thus the polarization swaps at the border between two domains. These domain walls can be related to topological solitons. Furthermore, a transition from a ferroelectric to a paraelectric phase, exhibiting no permanent polarization, is known to occur together with a change of the microscopic structure of the material. This structural transition is the breeding ground for strongly nonlinear propagation of sound and could deliver the ingredients, dispersion and nonlinearity, of another type of solitons as for instance the one exhibited in the Korteweg-de Vries equation.

We know from thermal volume expansion, as well as pressure and temperature dependent elastic properties like the speed of sound, that interatomic forces within a solid have to be nonlinear. From a dynamical point of view, this nonlinearity has been observed experimentally in  $\text{SrTiO}_3$  [BHS<sup>+</sup>12] by op-

---

tical Brilluin scattering measurements in the GHz range. Even the detection of solitons in solids at low temperatures has been reported [HM01, vCD10].

Nonlinearity in general gives rise to different phenomena, on the one hand the set of possible solutions has to be extended to not only include phonons but also solitons and breather. On the other hand, nonlinearity allows for scattering of phonons and thus a relaxation towards thermal equilibrium or even chaotic dynamics.

The thesis to hand is sectioned as follows. The first part (chapter 2) summarizes what is known about lattice dynamics and phonons. Furthermore, a short description of the ferroelectric phase transition exhibiting some interesting phenomena like the softening of an optical phonon mode is given. The following chapter 3 introduces the investigated model and its Hamiltonian. The stability of a unit cell is analyzed and the linear theory is derived including the dispersion relation and the sound velocity. Chapter 4 uses numerical investigations to confirm the linear theory and extend the examination to the nonlinear regime. That includes a qualitative view on the propagation of a pulse, where also solitons and breathers will be observed. Exciting the chain with a homogeneous spatial energy distribution allows to study the dispersion relation from the linear limit, i.e. low energy density, up to the nonlinear regime, thus high energy densities, where chaotic dynamics occur. An analysis with the maximum Lyapunov exponent allows a quantitative characterization of chaos. This view will be extended by studying the relaxation of a far-from-equilibrium state towards thermal equilibrium by using an entropy of the spatial Fourier spectrum. Finally chapter 5 summarizes the results and gives some possible extensions and applications as an outlook.

# Chapter 2

## Basics

This chapter contains a short introduction to the important ideas and methods used throughout this thesis. It starts with the basic theory on lattice dynamics and shall give first insights in the physical phenomena of ferroelectricity. It also provides the used notation. The first section focuses on lattice dynamics and the derivation of normal vibration modes of a two component linear chain exhibiting an optical and an acoustic branch. The quantum mechanical analogue leads to the definition of a phonon as the elementary excitation of the chain.

Within the second section 2.2, the physical properties of ferroelectricity will be introduced as well as observations at the phase transition from the paraelectric to a ferroelectric state. One important feature is the softening of an optical mode. In simple terms this means, that the linear restoring force on at least one component of the unit cell vanishes. Higher orders in the interaction get important approaching the nonlinear regime. In section 2.2.2 one theory considering the local electric field influenced by the microscopic movement of ions and the macroscopic formation of a depolarization field due to surface charges is given.

One early model of ferroelectric solids is the Aubry model, which was simultaneously introduced by Aubry as well as Krumhansl and Schrieffer in 1975 [Aub75, KS75]. The basic results of this model will be summarized in 2.3. It exhibits thermodynamic as well as dynamic properties of ferroelectrics. In this model a domain wall is described as a topological soliton due to using a one dimensional chain with a quartic potential exhibiting two degenerate ground states.

A nonlinear chain is likely to possess chaotic dynamics. Hence, a theoretical method of describing chaos by using the Lyapunov exponent will be mentioned together with an outline of a computational method of calculating the maximal Lyapunov exponent.

### 2.1 Lattice Dynamics

A lattice is defined by its separability into translationally invariant smallest cells, the unit cells. The forces on the atoms in the unit cell is determined by

complex interactions between occupied and unoccupied orbitals or charges of each constituent. However, when investigating the lattice dynamics, the electrons only provide the potential which instantaneously adjusts to the positions of the nuclei. This is called the adiabatic approximation. During the much slower movement of the lattice, the electron system will adiabatically reach its corresponding electronic state. The second approximation, which is often assumed when studying lattice dynamics, uses the fact, that small deviations from an equilibrium state should only feel a linear restoring force and thus a quadratic potential, also known from the harmonic oscillator.

### 2.1.1 Classical Linear Chain

A most simplified and idealized view on a crystal is provided by the linear chain. Firstly it assumes propagation along an axis of high symmetry as for example one of the unit cell axes. The layer perpendicular to the propagation axis shall execute only collective motion. Thus, the motion can be described effectively as a one dimensional chain.

#### Unit Cell with One Component

The overview given here follows mostly [KH07]. Imagine a one component linear chain with harmonic interaction. The interaction shall be independent of the position of the chain. Hence, the total interaction force  $F_s$  acting on the oscillator  $s$  depends only on the relative position of its neighbor  $s - n$ :

$$F_s = \sum_n \kappa_n (q_{s-n} - q_s),$$

where  $q_s$  and  $q_{s-n}$  are the displacement of the oscillator  $s$  and  $s-n$ .  $\kappa_n$  denotes the coupling strength with its  $n^{\text{th}}$  neighbor. In the general case all interactions have to be taken into account and the sum ranges from  $-\infty$  to  $+\infty$ . Newtons second law then delivers

$$m\ddot{q}_s = \sum_n \kappa_n (q_{s-n} - q_s).$$

The plane wave has the general solution  $q_s = Ae^{i(ksa-\omega t)}$ , whereas  $k$  is the wavenumber, which depends via  $k = \frac{2\pi}{\lambda}$  on the wavelength, and  $\omega$  is the corresponding vibration frequency.  $a$  is the equilibrium distance between two neighboring oscillators. In this simple case it corresponds to the lattice constant. Using this plane wave solution as an ansatz gives the dispersion law

$$\omega^2 = \frac{2}{m} \sum_{n=1}^{\infty} \kappa_n (1 - \cos(kna)) = \frac{4}{m} \sum_{n=1}^{\infty} \kappa_n \sin^2 \frac{kna}{2}, \quad (2.1)$$

denoting a relation between a wave vector and the eigenfrequency, i.e. the dispersion relation. Independently of the used  $\kappa_n$ , the eigenfrequency of a small wave number goes linearly to zero. It is the characteristic feature of

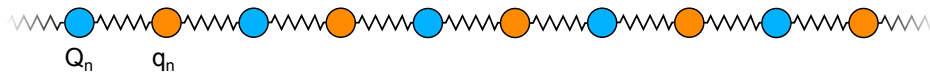


**Figure 2.1:** Sketch of the two component linear chain with nearest neighbor interaction.  $Q_n$  and  $q_n$  are the displacements of the two components in the  $n^{\text{th}}$  unit cell.

an acoustic phonon mode. In a small wavenumber limit  $\sin^2 \frac{kna}{2}$  simplifies to  $\frac{n^2 a^2}{4} k^2$  and therefore the group velocity can be given as

$$v^2 = \left( \frac{\partial \omega(k)}{\partial k} \right)^2 = \frac{a^2}{m} \sum_{n=1}^{\infty} n^2 \kappa_n. \quad (2.2)$$

The influence of  $n^{\text{th}}$  neighbor coupling increases quadratically, which implicates, that the spring constant has to decrease faster than  $\frac{1}{n^3}$  to ensure convergence of the sum. The situation changes if the  $\kappa_n$  are alternating, then convergence is sure if  $\kappa_n$  decreases with  $\frac{1}{n^2}$  or faster.

Taking only nearest neighbor interaction into account, (2.1) and (2.2) simplify to

$$\omega^2 = \frac{2}{m} \kappa_1 (1 - \cos(kna)) \quad (2.3)$$

and

$$v^2 = \frac{a^2 \kappa_1}{m} \rightarrow v = \pm a \sqrt{\frac{\kappa_1}{m}}. \quad (2.4)$$

### Unit Cell with Two Components

The previous chain will now be extended with a second constituent, which has to be distinguishable from the first one. This is done by assuming different masses  $m$  and  $M$ . Only nearest neighbor interactions are considered. Then, the equations of motion get:

$$m \ddot{q}_n = \kappa (Q_{n+1} - 2q_n + Q_n) \quad (2.5)$$

$$M \ddot{Q}_n = \kappa (q_{n+1} - 2Q_n + q_n), \quad (2.6)$$

where  $q_n$  and  $Q_n$  are the displacements of the components with mass  $m$  and  $M$ , respectively.  $\kappa$  is the spring constant of the harmonic nearest neighbor interaction. Using again a plane wave ansatz, but now extended to two sublattices shifted by  $\frac{a}{2}$  against each other

$$q_n = A e^{i(kna - \omega t)} \quad Q_n = B e^{i(k(n+\frac{1}{2})a - \omega t)},$$

one arrives at a dispersion relation with two solutions [KH07, (2.23), p. 88]:

$$\omega_{o,a}^2 = \kappa \frac{m+M}{mM} \pm \kappa \sqrt{\left( \frac{m+M}{mM} \right)^2 - \frac{4}{mM} \sin^2 \frac{kq}{2}}, \quad (2.7)$$

with  $k$  being the wavenumber. Now two frequencies  $\omega_o$  and  $\omega_a$  belong to each wavevector  $k$ .  $\omega_a$  shows the same linear behavior for small  $k$  as in the one component linear chain. It is the acoustic mode describing the same motion of neighboring oscillators. In the  $k \rightarrow 0$  limit it would approach a simple translation without any vibration. In contrast  $\omega_o$  reaches a finite value larger than zero for small  $k$ . It is the optical phonon mode, where neighboring oscillators perform opposite motion.

### 2.1.2 Phonons

By using a linear transformation, one can diagonalize the quantum mechanical Hamiltonian of a linear chain. That corresponds to a system of uncoupled harmonic oscillators. They do not belong to the dynamics of a single oscillator in the chain rather than to an elementary excitation called phonons. Phonons represent a collective oscillation of the whole chain. They have an energy  $E = \hbar\omega(k)$  and a momentum  $p = \hbar k$  similar to photons, but with different dispersion relation. In that sense phonons behave like particles. Similar to photons, they also follow the Bose-Einstein statistics.

From the classical point of view, phonons are the plane wave components of an arbitrary excitation, i.e. the Fourier transform of a spatial displacement distribution. These plane waves form an orthogonal basis. Hence, each excitation can be given as a superposition of plane waves. The dispersion relation  $\omega = \omega(k)$  determines the vibration frequency of a plane wave with wavevector  $k$ . It will also be derived for the investigated Double-Morse chain in section 3.4.

### 2.1.3 Phonon Excitation and Detection

Experimental methods are based on inelastic scattering of neutrons or photons at phonons. The inelastic scattering of photons at acoustic phonons is known as Brillouin scattering and as Raman scattering at optical phonons. The scattering events are inelastic due to the creation or annihilation of phonons. Energy (2.8) and momentum (2.9) conservation make it possible to draw conclusions on the excited phonon spectrum as well as the dispersion relation.

$$E_{q'} - E_q = \pm \hbar\omega_k \quad (2.8)$$

$$q' - q = \pm k \pm G, \quad (2.9)$$

where  $q$  is the wave number of the incoming neutron or photon and  $E_q$  the corresponding energy.  $q'$  and  $E_{q'}$  belong to the scattered neutron or light. In addition to the inelastic scattering on phonons, also an umklapp process with adding or subtracting the lattice wave vector  $G$  to the momentum equation can occur.  $G$  is determined by the periodicity of the lattice. However, without an inelastic scattering at phonons, this process would still conserve the energy but not the momentum.

Due to the different energy-wavenumber relations of neutrons and photons, both complement each other in detecting phonons in a wide frequency range.

For instance, Brillouin and Raman scattering of light covers small wavenumber phonons, i.e. around the Brillouin zone center.

## 2.2 Ferroelectric Phase Transition

Ferroelectricity is characterized by a switchable non-zero polarization without applying an external electric field. A spatial distribution of charges must exist, as is the case with ionic crystals, to form a microscopic electric dipole and thus a polarization. The ferroelectric property of a material gets lost by approaching a critical temperature named the Curie temperature. A phase transition to a paraelectric phase, which is characterized by a linear response of the polarization to an external electric field  $\vec{P} \propto \vec{E}$ , occurs. This transition can either be continuous or discontinuous. A continuous phase transition is also denoted as a second or higher order phase transition and analogously a discontinuous transition is denoted as a first order transition. A phenomenological model was introduced by Devonshire using the Landau theory of phase transitions. It is a mean field theory assuming that the free energy  $F_P$  depends polynomially on the mean polarization  $P$ , which serves as the order parameter:

$$F_P = \frac{a_0}{2} (T - T_0) P^2 + \frac{b}{4} P^4 + \frac{c}{6} P^6.$$

This choice of the first coefficient is used to reflect the critical behavior of most ferroelectric materials above the critical temperature, the Curie-Weiss law

$$\epsilon(T) \propto \frac{1}{T - T_C}.$$

Depending on the sign of the second coefficient  $b$ , either a continuous, if  $b > 0$ , or a discontinuous phase transition, if  $b < 0$ , is obtained. The figures 2.2 and 2.3 sketch the differences of the temperature dependent free energy. It is the most simplified Landau theory on ferroelectricity and further extensions exist. See [RAT07, ch. 3] for a review on that topic.

Furthermore, the ferroelectric transition is classified either as displacive or order-disorder depending on the respective microscopic mechanism.

In the former, no microscopic dipole moment of the unit cell exists above the critical temperature. Below the critical temperature, ions shift causing a permanent electric dipole. The displacive transition appears in crystals with a perovskite structure like  $\text{PbTiO}_3$  or  $\text{BaTiO}_3$ . Simultaneously with the ferroelectric phase transition, a structural phase transition appears, which is of special interest in this thesis as they give the motivation for the model which is introduced and investigated later. The structure is shown in figure 2.5, but a deeper view follows in the next section 2.2.1.

In the latter order-disorder transition the entropy plays a crucial role. Consider the free energy  $F = U - TS$ . Depending on the temperature  $T$ , it can either be minimized by minimizing the internal energy  $U$ , achieved by order, or by maximizing the entropy  $S$ , achieved by disorder. Examples exhibiting an order-disorder transition are crystals of polar molecules like Sodium Nitrite,

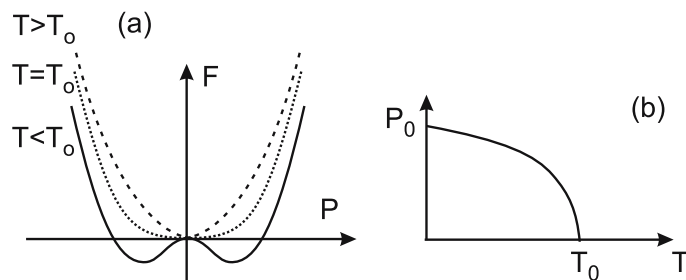


**Figure 2.2:** (a) Free energy over polarization in the Landau-Devonshire theory of a continuous phase transition [RAT07, p. 77]. (b) shows the corresponding temperature dependence of the polarization, which is zero in the paraelectric phase  $T > T_0$  and changes continuously to a finite value by lowering the temperature below  $T_0$  and reaching the ferroelectric phase.

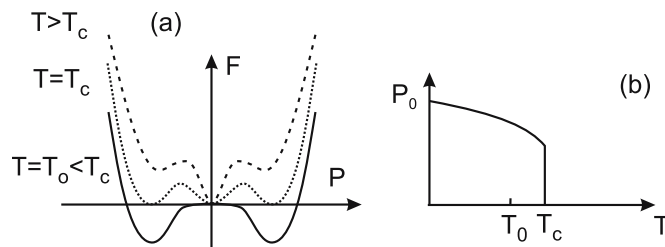


**Figure 2.3:** (a) Free energy over polarization in the Landau-Devonshire theory of a discontinuous phase transition [RAT07, p. 77]. (b) shows the corresponding temperature dependence of the polarization exhibiting a jump at the critical temperature  $T_0$ .

$\text{NaNO}_2$ , or caused by hydrogen bonds as for example potassium dihydrogen phosphate (KDP or  $\text{KH}_2\text{PO}_4$ ). The mechanism is sketched in figure 2.4. The proton has two possible positions between two phosphates. Either it is covalently bonded to one and forms a Hydrogen bond with a second neighboring phosphate or vice versa. In the paraelectric phase both positions are in average equally occupied, due to the thermal fluctuations and its ambition to maximize the entropy. Taking KDP as an example, this corresponds to randomly distributed  $\text{KHPO}_4^-$ ,  $\text{KH}_2\text{PO}_4$  and  $\text{KH}_3\text{PO}_4$  on the lattice giving rise to randomly oriented dipoles. In the ferroelectric phase the entropy has a lower influence on the free energy. The internal energy is minimized by approaching the ordered state with two protons sitting on each phosphate. Thus, only  $\text{KH}_2\text{PO}_4$  with a dipole pointing in a defined direction sits on each lattice point.

### 2.2.1 Perovskites

In the highest temperature state, the paraelectric phase, the perovskites exhibit a cubic structure with constituent  $A$ , for instance  $\text{Pb}^{2+}$  or  $\text{Ba}^{2+}$ , sitting

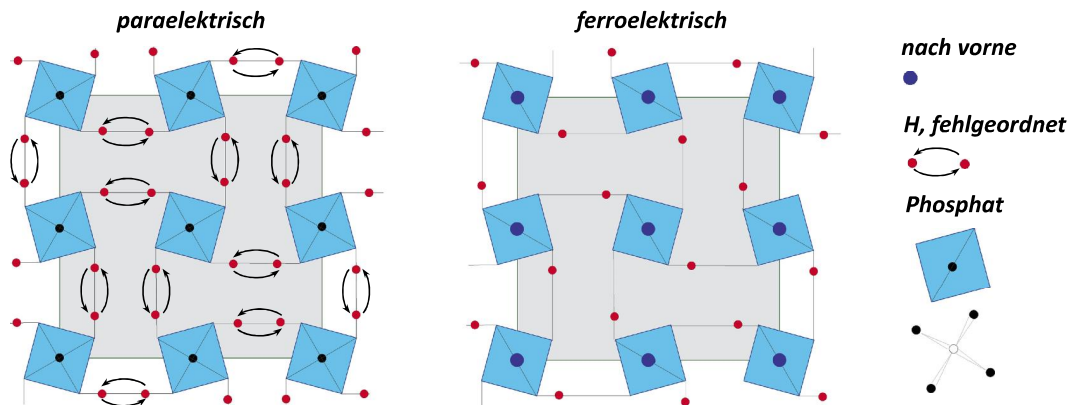


**Figure 2.4:** Schemata of order-disorder transition [GM12]. The left figure shows the paraelectric phase with disordered proton. Each proton has two possible positions. In the ferroelectric phase (right figure) the interaction between the protons mediated by the phosphate leads to a minimizing of the internal energy and to an ordered state.

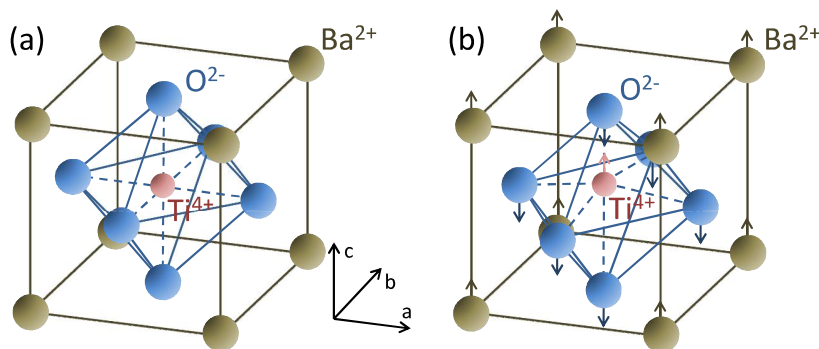


**Figure 2.5:** Perovskite structure of barium titanate  $\text{BaTiO}_3$  in the paraelectric phase (left) and in the ferroelectric phase (right) due to a displacement of the central ion against the Oxygen octahedron [GM12].

at the corners. The second constituent  $B$ , usually Oxygen ions, forms an octahedron centered around  $A$ . Right in the middle the third constituent  $C$ , often  $\text{Ti}^{4+}$ , can be found. When decreasing below the Curie temperature, the unit cell elongates along one of the primitive vectors. This particular one is then denoted as the  $c$ -axis. The octahedron shifts along the  $c$ -axis as does the central ion, but in the opposite direction. This leads to a net-dipole along the  $c$ -axis featuring the ferroelectric phase. The central ion has two equal positions determining the direction of the polarization. This behavior is sketched in figure 2.5.

Additional ferroelectric states exhibiting a different structure also exist. Just to mention one,  $\text{BaTiO}_3$  becomes rhombohedral, the central ion has eight equal positions along the space diagonals and no  $c$ -axis is allocated. However, not all perovskites exhibit a ferroelectric phase transition. For instance, it is suppressed in  $\text{SrTiO}_3$  by quantum fluctuations and in  $\text{SrRuO}_3$  by its metallic

character.

### 2.2.2 Two Component Linear Chain with Charges

The initial equations of motion used for the two component linear chain (2.5) and (2.6) can be extended by adding charges. One constituent gets the charge  $+ne$ , whereas the second one gets the opposite charge  $-ne$  maintaining a neutral chain of dipoles. Of special interest is the long wavelength limit, where  $|Q_{n+1} - Q_n|$  and  $|q_{n+1} - q_n|$  of the displacements  $Q_n$  and  $q_n$  are small. Therefore  $Q_{n+1} \approx Q_n$  and  $q_{n+1} \approx q_n$  holds. Thus, it is sufficient to examine the shift of both sublattices, each denoted with  $\vec{q}$  and  $\vec{Q}$ . The shift shall now be allowed to occur in any direction of the space and hence the vector notation is used. Following [KH07], equations (2.6) and (2.5) then change to:

$$m \frac{\partial^2 \vec{q}}{\partial t^2} = 2\kappa (\vec{Q} - \vec{q}) + ne\vec{E}_{loc} \quad (2.10)$$

$$M \frac{\partial^2 \vec{Q}}{\partial t^2} = 2\kappa (\vec{q} - \vec{Q}) - ne\vec{E}_{loc}, \quad (2.11)$$

where  $\vec{E}_{loc}$  is the locally acting electrical field. Defining the relative shift  $\vec{d} := \vec{q} - \vec{Q}$ , (2.10) and (2.11) can be combined to one differential vector equation for the relative shift  $\vec{d}$ :

$$\mu \ddot{\vec{d}} + \mu \omega_o^2 \vec{d} = ne\vec{E}_{loc}, \quad (2.12)$$

with the reduced mass  $\mu = \frac{mM}{m+M}$  and the frequency  $\omega_o$  of the optical mode at the small wave number limit  $k \rightarrow 0$  derived as  $\omega_o = \sqrt{2\kappa/\mu}$  from equation (2.7).

The local electric field  $\vec{E}_{loc}$  remains to be investigated. In general it is composed of the externally applied field, which shall be neglected, and the field caused by the surrounding dipole moments, which itself can be split in the following way. The first component is the depolarization field caused by surface charges. It strongly depends on the geometry of the sample. A derivation for a general ellipsoid can be found in [LL90a]. Here, the following two limits are necessary. When assuming a thin layer parallel to the polarization, the depolarization field becomes zero. In contrast it gets  $-\frac{1}{\epsilon_0}\vec{P}$  in the case of a thin layer perpendicular to the polarization. The second component is the Lorenz field of a fictive hollow sphere around the position of interest induced by surrounding dipoles. A third component would be the microscopic dipole moment of the unit cell, which vanishes for a cubic structure, but not for perovskites [KH07, p. 205]. This contribution will not be considered here, but by using a general ansatz at a later point.

As a result, the local field, still neglecting an external field, either adds to the linear response force and increases the frequency as for a longitudinal optical mode or counteracts and lowers the frequency as in the case of transverse

vibrations.

$$\vec{E}_{loc}^{\parallel} = +\frac{1}{3\epsilon_0}\vec{P} \quad (\text{longitudinal})$$

$$\vec{E}_{loc}^{\perp} = -\frac{2}{3\epsilon_0}\vec{P} \quad (\text{transversal})$$

The polarization contains the polarizability of the bounded electrons depending linearly on the local electric field and the ionic part due to displacements of the ions.

$$\vec{P} = \epsilon_0 N_V \alpha_{el} \vec{E}_{loc} + N_V n e \vec{d}$$

Finally by including the local electric field in the optical phonon frequency (2.7), one arrives at the corrected frequencies of the optical phonon mode in the limit of  $k \rightarrow 0$

$$\omega_T = \omega_0 \sqrt{1 - \frac{\frac{1}{3} N_V \alpha_{ion}(0)}{1 - \frac{1}{3} N_V \alpha_{el}(0)}}$$

$$\omega_L = \omega_0 \sqrt{1 + \frac{\frac{2}{3} N_V \alpha_{ion}(0)}{1 + \frac{2}{3} N_V \alpha_{el}(0)}}$$

On the time scale of optical phonon vibrations the motion of electrons can be seen as static, thus giving rise to the notation  $\alpha_{el}(0)$ . The static polarizability of the ionic part  $\alpha_{ion}(0)$  is obtained from (2.12) as:

$$\alpha_{ion}(0) = \frac{(ne)^2}{\epsilon_0 \mu \omega_0^2}$$

As already noted, the optical vibration modes get either softer or harder depending on the direction of vibration of the ions. The longitudinal optical phonon, denoted as  $\omega_L$ , has a higher frequency than in the case of two component chain without charges. The opposite is true for the frequency  $\omega_T$  of the transverse optical phonon mode giving rise to the following inequality:

$$\omega_T < \omega_o < \omega_L,$$

where  $\omega_o$  is the Brillouin zone center frequency of an optical vibration mode in a chain without charges.

It is worth noting, that a relation between  $\omega_T$  and  $\omega_L$  depending on the static dielectric constant  $\epsilon(0)$  and the dielectric constant  $\epsilon(\omega_S)$  within the visible spectrum exists

$$\frac{\omega_L^2}{\omega_T^2} = \frac{\epsilon(0)}{\epsilon(\omega_S)}, \quad (2.13)$$

which is known as the Lydane-Sachs-Teller relation.

### 2.2.3 Polarization Catastrophe

Consider the prior mentioned, but neglected, microscopic polarisation with the following general ansatz for the local electric field

$$\vec{E}_{loc} = \frac{\gamma}{\epsilon_0} \vec{P}, \quad (2.14)$$

where  $\gamma$  is a general factor.  $\gamma = \frac{1}{3}$  would resemble the usual Lorentz-field. By using (2.14), the polarization changes to [KH07, (4.91)]:

$$\vec{P} = \epsilon_0 \frac{N_V \alpha}{1 - \gamma N_V \alpha} \vec{E},$$

with  $\vec{E}$  being the macroscopic internal field  $\vec{E}_{ext} + \vec{E}_N$ , thus the sum of the externally applied field and the depolarization field, which is caused by surface charges.

The main contribution to the polarization field of a perovskite comes from the shift of the central ion against the Oxygen octahedron and leads to values of  $\gamma$  much larger than  $\frac{1}{3}$ . In the case of  $\gamma N_V \alpha$  approaching one, the denominator gets zero, and the polarization field diverges. In other words, an arbitrarily small external field would lead to infinitely large polarization, hence the name ‘‘polarization catastrophe’’. The central ion would shift significantly with respect to the Oxygen octahedron, thus leaving the limit of a linear restoring force. Only the higher than quadratic orders in the interaction term ensure an equilibrium state and the stability of the crystal. With decreasing the linear restoring force in the small amplitude approximation, used for phonons, also the frequency drops until it might even vanish. In conclusion, the optical phonon mode exhibits a softening in the small wavenumber limit, i.e. at the Brillouin zone center. This is called a soft mode. It was first mentioned by M. Born and K. Huang [BH54], that the stability of a crystal against small perturbations is given as long as the normal modes have real frequencies. The crystal would be unstable in the case of an imaginary frequency. The implication for ferroelectric materials exhibiting a polarization due to the displacement of ions is, that the involved normal mode(s) have to vanish. This implication was first mentioned by W. Cochran [Coc59]. He derived the polarization catastrophe and the soft mode behavior by using a core-shell model. The soft-mode behavior was found for a number of perovskites, for instance SrTiO<sub>3</sub> [Cow62], KTaO<sub>3</sub> [SNM66] and PbTiO<sub>3</sub> [BS73].

The consequence of the LST relation (2.13) is now, that for ferroelectrics exhibiting a soft mode, the static dielectric function approaches rather large values and leads to a strong reflectivity of low frequency light.

## 2.3 Aubry Model

A first classical model suitable for analytical and numerical studies of ferroelectric materials was introduced independently by S. Aubry [Aub75, Aub76] and by J. Krumhansl and R. Schrieffer [KS75] in 1975. [B82] gives an overview

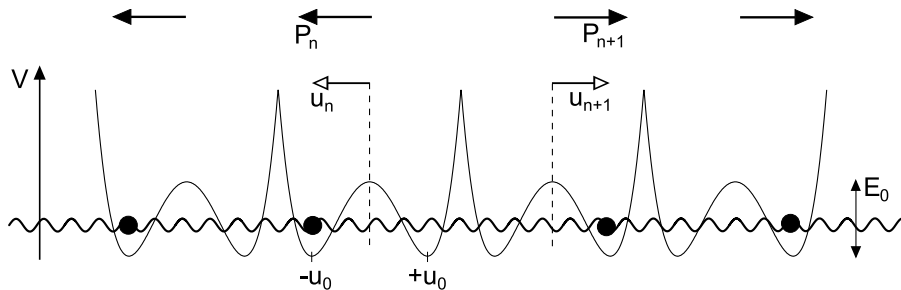


**Figure 2.6:** Sketch of the one component chain introduced by S. Aubry [Aub75]. The figure is adopted from [DP06]. The rigid lattice forms an on-site potential assumed to be of fourth order with two degenerate wells. Only harmonic nearest neighbor interaction is considered.  $u_n$  denotes the displacement of the central ion and the solid black arrows show the corresponding polarization  $P_n$ .

of the early work including a lot of references, whereas [DP06] is more suitable as an introduction to the model.

Here I follow the original view by S. Aubry. He assumes a two component chain formed by two sublattices  $A$  and  $B$ . Both are coupled via a double well potential with terms of quadratic and quartic order in the displacements  $u_n$  in order to achieve two degenerate ground states arranged symmetrically around  $u = 0$ . The sublattice  $A$  shall belong to the heavy background lattice and is assumed to be rigid. Thus, the chain simplifies to an effective one component chain with an on-site potential, i.e. a locally acting potential

$$V(u_n) = \frac{E_0}{u_0^4} (u_n^2 - u_0^2)^2.$$

Only harmonic nearest neighbor interaction with a coupling strength  $C$  is considered. The model is further simplified by taking only one degree of freedom per oscillator into account. Accordingly, the Hamiltonian is written as [Aub75]

$$H = \sum_n \frac{p_n^2}{2m} + \sum_n V(u_n) + \frac{C}{2} \sum_n (u_n - u_{n+1})^2.$$

The interactions, the displacements  $u_n$  and the corresponding polarization direction are illustrated in figure 2.6.

Landau gave an argument, why any one dimensional system with finite range interactions cannot undergo a phase transition at finite temperatures [LL90b]. However, Aubry allocated different thermodynamic regimes corresponding to the higher dimensional case, but did not find a transition exhibiting critical behavior [Aub75].

It is obvious that in the lowest energy state, all oscillators will sit in the same well, either left or right. This corresponds to a left or right polarization and resembles the ferroelectric phase. At higher temperatures, but still in the ferroelectric phase, thermal excitations arise. They can either be phonons, small amplitude solutions, or domain walls, large amplitude solutions. Getting

more specific, two limits depending on the coupling strength relative to the barrier height  $E_0$  exist.

In the case of low coupling strength ( $Cu_0^2 \ll E_0$ ), Aubry found an order-disorder transition. At lowest temperatures  $k_B T \ll E_0$  the central ion sits in one of the two wells. It can thus be described as a quasi-spin in an Ising chain with an Ising transition occurring at around  $T_I \approx 0.844 \frac{Cu_0^2}{k_B}$ . A phonon description is valid in this regime. At higher temperatures the model reaches the limit of uncoupled oscillators in a double well potential. A characteristic temperature  $T_0$  is given by the temperature exhibiting oscillations above the barrier from one well to the other. It would correspond to the phase transition temperature in order-disorder ferroelectrics.

For large coupling strengths ( $Cu_0^2 \gg E_0$ ) the model describes the displacive regime. The energy to place one oscillator on the barrier is lower than the energy necessary for expansion or tension in the nearest neighbor interaction if the polarization of neighboring oscillators swaps. Hence, the domain wall spreads over several unit cells and the difference  $|u_n - u_{n-1}|$  is small. Large wavenumber excitations will be solely due to phonons, whereas small wavenumber will have a contribution from domain walls and thus, they depend more on temperature. In contrast to the order-disorder transition, only one characteristic temperature  $T_S$  has been found. By decreasing the temperature towards  $T_S$ , the small wavenumber vibrations decrease their frequency and a central peak occurs. This central peak denotes a peak in the frequency spectrum at low wavenumbers. It has been observed by doing neutron scattering close to temperatures at which the material exhibits a structural phase transition, for instance in SrTiO<sub>3</sub> [SASR72].

Furthermore, the domain walls are studied and an analytical expression has been derived using a continuous approximation [Aub76, (2.8)]:

$$u(x, t) = \pm u_0 \tanh \left( \sqrt{\frac{2E_0}{Cl^2 u_0^2 (1 - \frac{v^2}{c^2})}} (x - vt) \right).$$

Where “+” is called a kink and “-” an antikink domain wall.  $l$  denotes the length of the unit cell and  $v$  the propagation velocity of the domain wall. The solutions are Lorentz-invariant and thus the domain walls exhibit a relativistic behavior with an upper velocity limit given by the sound velocity  $c$ . They are stable against small perturbations. However, they do not show a complete solitonic behavior, as the collision of a kink and an antikink soliton can either lead to an annihilation and excitation of optical phonons or they pass each other with a phase shift, but with a small damping lowering the propagation velocity of the kink and antikink [Aub76].

Studies of the displacive case in higher dimensions generally confirm the different temperature regimes and exhibit the predicted phase transition. Schneider and Stoll did molecular dynamics simulations on a two dimensional lattice with a similar on-site potential and harmonic nearest neighbor interaction as in the one dimensional Aubry model [SS78]. They attribute the central peak to be either caused by heat diffusion or by domain wall dynamics. The latter one

increases towards the critical temperature and takes over at higher temperatures. Dauxois and Peyrard give the following more descriptive explanation for the central peak [DP06]: The low frequency field induces a motion of kink and antikink solitons, the domain walls. The lower the frequency is, the higher is the displacement of the domain walls. As kink and antikink move in different directions, this leads to a larger macroscopic polarization. One can also say, the external field induces a growth of the domains with a polarization parallel to the external field or it induces a shrinking if the polarization is antiparallel. This leads to a central peak in the susceptibility. Additional to the central peak, Schneider and Stoll [SS78] observed an envelope soliton-like heat-pulse at low temperatures, also known as second sound.

These investigations are done at thermal equilibrium. Besides relaxation processes due to the nonlinear interaction, it is worth to study how regular or irregular the dynamics in such a system are. This is a part of chaos theory and some basic ideas shall be introduced in the following section.

## 2.4 Chaotic Dynamics

In a very simplified manner, one speaks of chaos, if a dynamical system is sensitive to initial conditions and small perturbations. More mathematical definitions can be found in the lecture notes of Ch. Skokos [Sko10] and references therein.

Getting back to lattice dynamics, one is mostly interested in the frequency or wavenumber spectrum of phonons. In an ideal solid the observed wavenumber and frequency distribution would be sharply distributed around the dispersion relation. However, either due to impurities or nonlinearity, this distribution will spread. As only the last case is considered here, a numerically obtained Fourier spectrum and the linewidth around an eigenfrequency would also allow to study the influence of the nonlinearity and if the dynamics are regular or chaotic. But a quantitative measure would be favorable and can be obtained by using the Lyapunov exponent.

### 2.4.1 Characterizing Chaos - Lyapunov Exponent

The Lyapunov exponents are a measure of the exponential growth of a small perturbation to an initial condition and how fast two trajectories in the phase space, initially close together, start to deviate. For each dimension of the phase space exists one Lyapunov exponent, but the largest one, the maximum Lyapunov exponent, is sufficient to distinguish between regular and chaotic dynamics [Sko10].

Let a dynamical system be denoted as  $\dot{x} = f(x, t)$  and introduce a small perturbation to the initial condition  $x(0)$  as  $\delta x_0$ . Then, the maximal Lyapunov exponent (mLE)  $\lambda_m$  can be defined as:

$$\lambda_m = \lim_{t \rightarrow \infty} \lim_{\delta x_0 \rightarrow 0} \left| \frac{\delta x(t)}{\delta x_0} \right|. \quad (2.15)$$

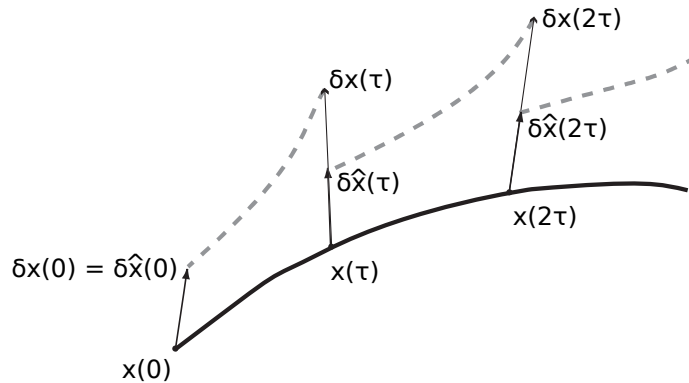


**Figure 2.7:** Schemata of the numerical method for determining the maximal Lyapunov exponent [Sko10]. The time is sliced in equidistant intervals in which the linear evolution of the perturbation  $\delta x$  is calculated. At the end of each slice the exponential growth is stored and the perturbation is subsequently normalized to unity.

If  $\lambda_m$  is larger than zero, exponential growth of the perturbation is indicated and chaotic behavior displayed. The opposite case of  $\lambda_m < 0$  denotes a stable trajectory, the phase space shrinks. The system must be dissipative to achieve this.

### 2.4.2 Maximal Lyapunov Exponent - Computational Method

Numerical computations have to deal with discreteness in time and finiteness of variables. That is why the definition (2.15) is not directly applicable and has to be modified. Figure 2.7 sketches the general idea to separate the time in slices. The initial condition is  $x(0)$  and the initial perturbation is randomly assigned with norm unity. Then, the trajectory and the perturbation are calculated by a numerical integration method. At each integer multiple  $j\tau$ , the obtained norm of the perturbation is saved as  $\alpha_j = \delta x(j\tau)$  followed by a renormalization of  $\delta x$  to unity. This is repeated until a predefined finishing time is reached. The temporal evolution of the mLE can now be calculated with the recorded  $\alpha_j$  as

$$\lambda_m(n\tau) = \frac{1}{n\tau} \sum_{j=1}^n \ln(\alpha_j).$$

Still, this method can only run a finite time, and thus the mLE differs from cycle to cycle. Additionally caused by the finite runtime, such a mLE would correspond to a specific initial condition. To get a complete view on the behavior of a dynamical system in its phase space, the initial condition can also be randomly assigned. A constraint like the total energy might be used.

A detailed description of the method can also be found in the lecture notes of Ch. Skokos [Sko10, p. 95].

# Chapter 3

## Model

The model of the two component linear chain with harmonic next-nearest and anharmonic nearest neighbor interaction by a Morse potential will be introduced (3.2) in this chapter and analytical results presented. First it is important to show that the model exhibits the requested phase transition. This will be done in section 3.3. Some crucial differences to the Aubry model exist: The thesis on hand will investigate dynamical phenomena and neglects the thermodynamical point of view. The phase transition will therefore be driven by an external parameter. This is conceived to be altered by temperature without specification of details. An external parameter for driving the transition avoids the fact, that a thermodynamic phase transition cannot occur in a one dimensional chain at finite temperatures. Another crucial difference is the translational invariance of investigated model. This gets important when looking for small amplitude solutions in the sense of phonons. Generally the phonon dispersion relation will exhibit two branches, because the unit cell has two components. Only due to the translational invariance one ensures the existence of an acoustic branch with a linear behavior for small wavenumbers. The derivation of the dispersion relation including a study of the sound velocity is part of section 3.4. Especially their behavior at the phase transition is of interest, as experimentally observed features like the softening of an optical phonon mode at the Brillouin zone center exist within this model despite of studying only the linearized problem.

Due to the topology of the effective potential of the central ion, in particular two degenerate ground states, caused by the unit cell lattice, one expects to observe topological solitons. These are also known as kink and antikink solitons and can be related to domain walls. An analytical derivation of them is sketched in section 3.5. Similar to the Aubry model, one expects that a maximal propagation velocity for these kink and antikink solitons exists.

It shall be noted that the same chain was used in the context of hydrogen bonded chains [SZ91, ZPS91, ZPS00, KZ04]. Especially the existence of topological solitons and their stability as well as their energy spectrum was studied.

Before starting with the model, a few thoughts shall be spent on why and when a one-dimensional model could reflect a realistic behavior of solids.

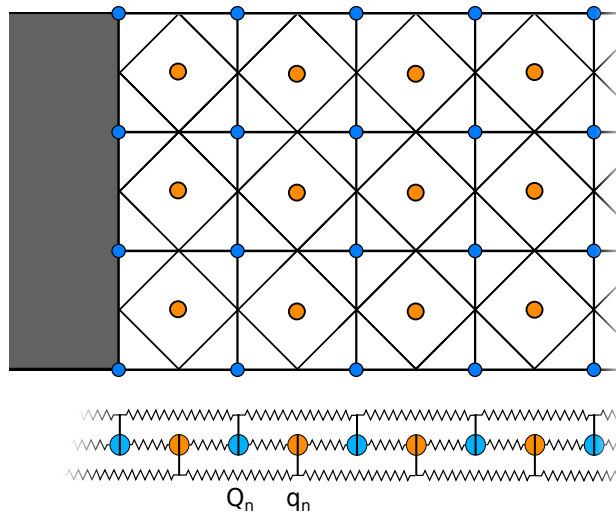


**Figure 3.1:** *Sketch of the two-component linear chain with anharmonic nearest neighbor and harmonic next-nearest neighbor interaction, each oscillator corresponds to one layer of atoms perpendicular to the sound propagation.*

### 3.1 How to get to a 1D Model?

Assume that you have a bulk and excite a thin layer at its surface leading to an expansion or contraction of this layer. This is illustrated as a gray layer in figure 3.1. A strain or stress pulse is initiated. As long as the propagation length  $d$  of the pulse is much smaller than the diameter  $r$  of the excited area  $d \ll a$ , the pulse will exhibit a planar wavefront, which is parallel to the surface and perpendicular to its propagation direction. Thus, the dynamics are effectively one dimensional. Each layer of atoms perpendicular to the wave propagation can be seen as one component of a one dimensional chain. Look again at figure 3.1. The central ions marked in orange add up to one orange oscillator within the chain. The blue ions sitting in the corner of the cubic unit cell form a second layer and reduce to the blue oscillator in the chain. Doing this for the whole substrate gives a chain of alternating blue and orange oscillators. Each oscillator shall interact with its nearest neighbor of the same type and with its nearest neighbor of the other type. Thus nearest neighbor and next-nearest neighbor springs are added as shown in the same figure.

### 3.2 Hamiltonian

The chain consists of two components coupled via a Morse potential, which is widely used within molecular and atomic physics. Additionally, next-nearest neighbors are coupled via a harmonic potential, hence an ideal spring. The couplings are illustrated in figure 3.1. Alternatively, the chain can be seen as a composition of two chains, one for each component, with an additional interaction term. One subchain describes the dynamics of the more rigid unit

cell, thus it has heavier components and a larger spring constant. It will be denoted as the Q-subchain. The q-subchain describes the dynamics of the central ions. With these assumptions and notations, the Hamiltonian can be introduced as [ZPS00]:

$$H = \sum_n \left[ \frac{p_n^2}{2m} + \frac{P_n^2}{2M} + \frac{k}{2}(q_{n+1} - q_n)^2 + \frac{K}{2}(Q_{n+1} - Q_n)^2 + V_M(Q_{n+1} - q_n) + V_M(q_n - Q_n) \right], \quad (3.1)$$

where  $q_n$  and  $Q_n$  are the displacements of the components with its point of origin at  $(n + \frac{1}{2})a$  and  $na$  respectively. Hence, the distance between the ions in each subchain is given by the lattice constant  $a$ . Furthermore  $m$ ,  $M$ ,  $k$  and  $K$  are the masses and spring constants of the central ion and the rigid unit cell subchain. The Hamilton equations  $\dot{q}_n = \frac{\partial H}{\partial p_n}$  and  $\dot{Q}_n = \frac{\partial H}{\partial P_n}$  determine the relations between the momenta and the velocities of each component:

$$p_n = m\dot{q}_n \qquad P_n = M\dot{Q}_n.$$

The momenta will be replaced by this relation in all further derivations.

The central ion subchain is shifted by  $a/2$  with respect to the heavier Q-subchain reflecting the unit cell dynamics. The Morse potential is thus given as:

$$V_M(x) = D \left( 1 - \exp \left( -\beta \left( x + \frac{a}{2} - r_0 \right) \right) \right)^2,$$

with the dissociation energy  $D$  and the equilibrium distance  $r_0$ , when considering only two atoms.  $\beta$  determines the curvature at the minimum  $x_0 = r_0 - \frac{a}{2}$ .  $x$  has to be the difference of the displacements of two neighboring oscillators. This use of two Morse potentials back-to-back with respect to  $q_n$  was first mentioned by Baker in 1954 [Bak54] and later in 1980 used by Lawrence and Robertson [LR80] in the context of Hydrogen bonded ferroelectrics. It is now worth rescaling the variables and eliminating some parameters for the purpose of simplifying all further analytic investigations.

### 3.2.1 Rescaling of Hamiltonian

One has the freedom to rescale  $q_n$ ,  $Q_n$ , time and energy. In this section this freedom is used to minimize the number of parameters. Let us start with a general linear transformation of the displacements

$$q_n \rightarrow Aq_n \qquad Q_n \rightarrow BQ_n,$$

leading to the following Hamiltonian

$$H = \sum_n \left[ \frac{A^2 m \dot{q}_n^2}{2} + \frac{B^2 M \dot{Q}_n^2}{2} + \frac{kA^2}{2}(q_{n+1} - q_n)^2 + \frac{KB^2}{2}(Q_{n+1} - Q_n)^2 + D \left( 1 + \eta e^{-\beta(Aq_n - BQ_n)} \right)^2 + D \left( 1 + \eta e^{-\beta(BQ_{n+1} - Aq_n)} \right)^2 \right],$$

whereas  $\eta$  has been introduced as  $\eta = e^{-\beta(a/2-r_0)}$ . As  $q_n$  and  $Q_n$  appear together in the exponent, the same scaling  $A = B = 1/\beta$  for  $A$  and  $B$  is chosen. It then follows

$$\frac{H}{D} = \sum_n \left[ \frac{m\dot{q}_n^2}{2\beta^2 D} + \frac{m\dot{Q}_n^2}{2\beta^2 D} + \frac{k}{2\beta^2 D} (q_{n+1} - q_n)^2 + \frac{K}{2\beta^2 D} (Q_{n+1} - Q_n)^2 + (1 + \eta e^{-(q_n - Q_n)})^2 + (1 + \eta e^{-(Q_{n+1} - q_n)})^2 \right].$$

Note that the whole Hamiltonian has additionally been divided by  $D$  to obtain a dimensionless energy and to leave only the parameter  $\eta$  within the nonlinear interaction. Thus, one reasonable choice for rescaling the time would be

$$t \rightarrow \frac{1}{\beta} \sqrt{\frac{m}{D}} t \quad \Rightarrow \quad \frac{d}{dt} \rightarrow \beta \sqrt{\frac{D}{m}} \frac{d}{dt}.$$

This eliminates  $\beta$  and  $D$  within the kinetic energy and lets one introduce the mass ratio  $\mu = \frac{M}{m}$ . Finally, the Hamiltonian gets

$$\frac{H}{D} = \sum_n \left[ \frac{\dot{q}_n^2}{2} + \frac{\mu \dot{Q}_n^2}{2} + \frac{\bar{k}}{2} (q_{n+1} - q_n)^2 + \frac{\bar{K}}{2} (Q_{n+1} - Q_n)^2 + (1 + \eta e^{-(q_n - Q_n)})^2 + (1 + \eta e^{-(Q_{n+1} - q_n)})^2 \right], \quad (3.2)$$

with substituted  $\bar{k} := \frac{k}{\beta^2 D}$  and  $\bar{K} := \frac{K}{\beta^2 D}$ . By applying this rescaling, one ends up with four independent parameters.  $\bar{k}$  and  $\bar{K}$  determine a weighting between the three interactions, namely the harmonic interaction in each subchain and the interaction between both subchains by the two Morse potentials.  $\mu = \frac{M}{m}$  is the mass ratio of the two components.  $\eta$  ascertains the shape of the Morse potential and, as it will become clear in the next section, will be the crucial parameter for tuning the phase-transition.

Other scalings could have been used, but the main goals here are to eliminate as many parameters within the nonlinear interaction as possible and to assure that the scaling does not diverge at any  $\eta$ . In the literature rescalings can be found which do not satisfy the last criterion [KZ04].

### 3.3 Ferrodistorion

The notion of ferrodistorion is used here in the sense, that for the central ion two degenerate ground states exist. If one now assumes, that both constituents have a positive and a negative charge, one gets ferroelectric behavior. The two Morse potential can be added to one so called Double-Morse potential exhibiting this feature depending on a phase transition parameter. To my knowledge, the first application within a one dimensional chain can be found in the work of Savin, Zolotaryuk and Pnevmatikos [SZ91, ZPS91].

### 3.3.1 Double-Morse Potential

The ferrodistortive nature of this chain is revealed by considering only one unit cell, thus the last three terms of (3.2). They contain the harmonic coupling of the oscillators at  $Q_{n+1}$  and  $Q_n$  and the two Morse potentials. Equation (3.3) also includes the coupling between the central ions. Consider the ground state, where all central ions sit together either in the left or the right well, thus the distance  $q_{n+1} - q_n$  is equal to  $Q_{n+1} - Q_n$ .

$$V_{uc}(Q_{n+1}, Q_n, q_{n+1}, q_n) := \frac{\bar{K}}{2}(Q_{n+1} - Q_n)^2 + \frac{\bar{k}}{2}(q_{n+1} - q_n)^2 + (1 - \eta e^{-(Q_{n+1} - q_n)})^2 + (1 - \eta e^{-(q_n - Q_n)})^2 \quad (3.3)$$

$$V_{uc}(\rho_n, u_n) = \frac{(\bar{K} + \bar{k})\rho^2}{2} + \left(1 - \eta e^{-\left(\frac{\rho_n}{2} - u_n\right)}\right)^2 + \left(1 - \eta e^{-\left(\frac{\rho_n}{2} + u_n\right)}\right)^2 \quad (3.4)$$

The transition from equation (3.3) to (3.4) includes extending the exponent within the Morse potentials by  $+\frac{Q_n}{2} - \frac{Q_n}{2}$  and  $+\frac{Q_{n+1}}{2} - \frac{Q_{n+1}}{2}$  accordingly and introducing the two new variables

$$\rho_n = Q_{n+1} - Q_n \quad (3.5)$$

$$u_n = q_n - \frac{1}{2}(Q_{n+1} + Q_n), \quad (3.6)$$

where  $\rho_n$  describes the unit cell deformation and  $u_n$  the central ion displacement. Further transposing and replacing  $\eta$  by  $\eta = \frac{1}{2\alpha}$  leads to

$$V_{uc}(\rho_n, u_n) = \frac{(\bar{K} + \bar{k})\rho_n^2}{2} - \frac{e^{-\rho_n}}{2\alpha^2} + 1 + \left(1 - \frac{e^{-\frac{\rho_n}{2}}}{\alpha} \cosh(u_n)\right)^2. \quad (3.7)$$

The first two terms show, that  $\rho_n$  decreases with smaller  $(\bar{K} + \bar{k})$ . In other words: the chain contracts, if the harmonic next-nearest neighbor interactions are weak. This contraction depends on  $\alpha$ . The implications of that will be part of the next subsection.

The last term is the so called Double-Morse potential. Depending on  $\frac{1}{\alpha} e^{-\frac{\rho_n}{2}}$ , for convenience called  $\xi_n$ , it shows two regimes. For  $\xi_n < 1$  two degenerate wells arranged symmetrically around the middle of the unit cell exist. Their position can be calculated exactly as

$$u_0 = \pm \operatorname{arccosh}\left(\frac{1}{\xi_n}\right). \quad (3.8)$$

This regime corresponds to a ferrodistortive phase, which causes, under consideration of positive and negative charges for each component, a dipole and hence a polarization. Thus it can also be seen as a ferroelectric phase. For  $\xi_n > 1$  only one well in the middle of the unit cell  $u_0 = 0$  exists. This regime is called the paraelectric phase. The potential for different  $\xi_n$  is shown in the left

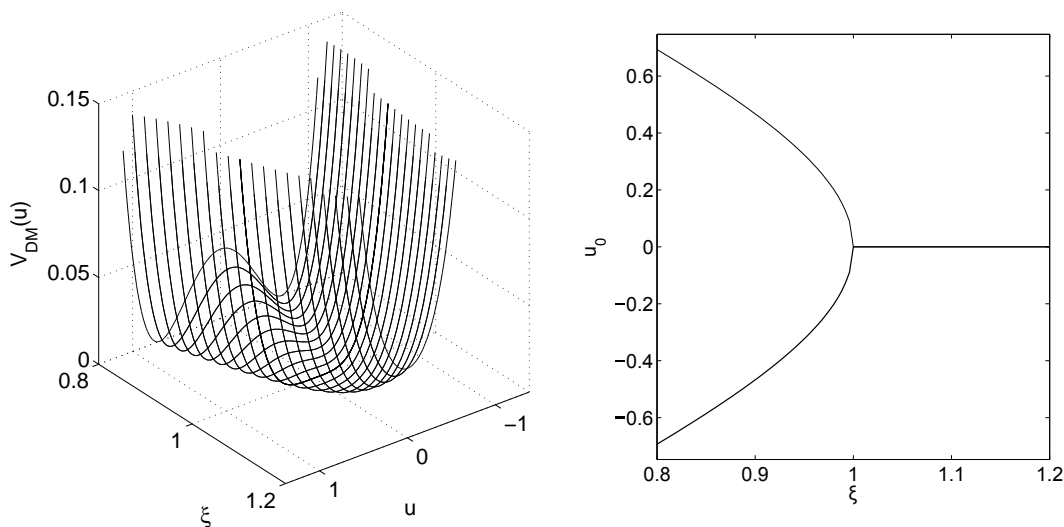


**Figure 3.2:** The Double-Morse potential given by equation (3.7) with  $\rho_n = 0$  for different  $\xi$  (left) and its bifurcation diagram for the equilibrium positions (right) according to equation (3.8). The phase transition from two degenerate ground states to only one occurs at  $\xi = 1$ .

figure of 3.2. The corresponding bifurcation plot for the equilibrium position for the central ion  $u_0$  can be seen in the right figure. It illustrates the phase transition from the ferroelectric to the paraelectric phase. Considering the Landau theory of phase transitions and  $u_0$  as the corresponding order parameter of the displacive transition,  $u_0$  changes continuously from a finite value to zero implying a continuous or second order phase transition.

Note, that the phase transition from the ferroelectric to the paraelectric phase can be achieved either by contracting the whole chain or by changing  $\alpha$ . The first case could experimentally be done by applying a pressure. Secondly,  $\alpha$  could be temperature dependent and would correspond to driving a phase transition by heating or cooling the sample. Yet both can be applied, which is illustrated in figure 3.3. The line of the transition is calculated by setting  $\xi_n = 1$  leading to relation  $\alpha = e^{-\rho_n/2}$

A similar, but slightly different, derivation of the Double-Morse potential can be found in [ZPS00]. They initially assume, that the pure Q-chain has an equilibrium distance  $R_0 > \rho_0$  between two neighbors. By adding one constituent in between two neighboring Q-chain constituents interacting via a Morse potential with each other, the chain contracts until this interaction cancels the linear part of  $\frac{1}{2\alpha^2}e^{-\rho_n}$ . That implies an equilibrium distance  $R_0$ , which is chosen depending on  $\alpha$  to maintain a constant  $\rho_0$ .

### 3.3.2 Contraction of the Unit Cell

In the case of a free chain, that is with open boundaries condition, the total length of the chain may vary due to the Morse interaction. Depending of

the state of the chain, i.e. the equilibrium position of the central ion, the Double-Morse potential in equation (3.7) either vanishes, as in the ferroelectric case, or reduces to  $\left(1 - \frac{1}{\alpha}e^{-\frac{\rho n}{2}}\right)^2$  in the paraelectric phase. This requires a differentiation in the following calculation. As only one unit cell is considered, the index  $n$  will be omitted.

### Ferroelectric Phase

In the ferroelectric phase the central ion sits in one of the wells and therefore  $u_0 = \operatorname{arccosh}\left(\frac{\alpha}{e^{-\rho/2}}\right)$  will be plugged into (3.7). This gives

$$V(\rho)|_{u=u_0} = \frac{(\bar{K} + \bar{k})\rho^2}{2} + 1 - \frac{e^{-\rho}}{2\alpha^2}.$$

The minimum of this energy with respect to  $\rho$  determines the equilibrium unit cell deformation  $\rho_0$

$$\rho_0 = -\frac{e^{-\rho_0}}{2\alpha^2(\bar{K} + \bar{k})}. \quad (3.9)$$

Unfortunately, equation (3.9) is transcendental and no simple analytic solution can be given.

$$\xi := \frac{e^{-\frac{\rho_0}{2}}}{\alpha} \quad (3.10)$$

But instead, the definition of  $\xi$ , see equation (3.10), can be reused here to get a simple quadratic dependence of  $\rho_0$  on  $\xi$

$$\rho_0 = -\frac{\xi^2}{2(\bar{K} + \bar{k})}. \quad (3.11)$$

### Paraelectric Phase

In the paraelectric phase, the central ion sits in the middle and  $u_0 = 0$  holds. Applied to (3.7), this leads to

$$V(\rho)|_{u=u_0} = \frac{(\bar{K} + \bar{k})\rho^2}{2} + 2 + \frac{e^{-\rho}}{2\alpha^2} - 2\frac{e^{-\frac{\rho}{2}}}{\alpha}.$$

The equilibrium unit cell deformation  $\rho_0$  gets, by using the same method, again a transcendental conditional equation (3.12). Similar to the ferroelectric phase, the definition (3.10) can be used to get the simplified expression (3.13).

$$\rho_0 = \frac{e^{-\rho_0}}{2\alpha^2(\bar{K} + \bar{k})} - \frac{e^{-\frac{\rho_0}{2}}}{\alpha(\bar{K} + \bar{k})} \quad (3.12)$$

$$\rho_0 = \frac{\xi^2 - 2\xi}{2(\bar{K} + \bar{k})} \quad (3.13)$$

In summary, a free chain contracts towards the phase transition. Calculating  $\rho_0$  as a function of  $\alpha$  is analytically not feasible, but the expression simplifies significantly by using  $\xi$ . The  $\rho_0$ - $\xi$  dependence is shown in figure

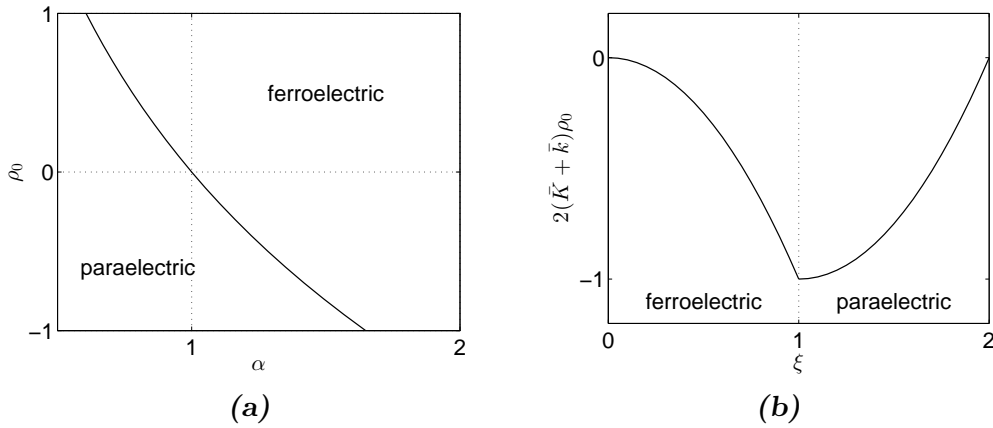


**Figure 3.3:** The phase diagram dependent on the unit cell deformation  $\rho_0$  and the Double-Morse parameter  $\alpha$  (a) and the dependence of the  $\rho_0$  on  $\xi$  for a free chain (b).

3.3b. The chain is most contracted at the phase transition with a contraction depending on the strength of the next-nearest neighbor interactions. Hence,  $\rho = 0$  does not seem to be a valid equilibrium point for a Taylor expansion, that will be needed in the small amplitude approximation for calculating the phonon dispersion relation. This will be done in section 3.4. But adding the constraint of constant total length (3.14) changes this situation.

$$\sum_n \rho_n = 0 \quad (3.14)$$

This constraint is necessary in the case of periodic boundaries.

### Periodic Boundaries

Introducing a small perturbation  $\delta\rho$  to the  $i^{\text{th}}$  unit cell combined with the constraint (3.14) gives the following total perturbation:

$$\rho_i = \delta\rho \quad \forall k \setminus i : \rho_i = -\frac{\delta\rho}{N-1}, \quad (3.15)$$

where  $N$  is the total number of unit cells in the chain. Plugging (3.15) into the unit cell potential (3.7), where  $u_n$  is assumed to be in the equilibrium position  $u_0$ , thus neglecting the last term, gives:

$$V + \delta V = \sum_{\forall k \setminus i} \left( \frac{(\bar{K} + \bar{k})\delta\rho_k^2}{2(N-1)^2} - \frac{e^{\frac{\delta\rho_k}{N-1}}}{2\alpha^2} + 1 \right) + \frac{(\bar{K} + \bar{k})\delta\rho_i^2}{2} - \frac{e^{-\delta\rho_n}}{2\alpha^2} + 1.$$

Transposing and subtracting the potential energy  $V$  without perturbation leads to

$$\delta V = \frac{N}{N-1} \left( \frac{\bar{K} + \bar{k}}{2} - \frac{1}{4\alpha^2} \right) \delta\rho^2. \quad (3.16)$$

This gives a threshold of stability against a collapse of the unit cell for the situation, where all  $\rho_n$  are set to 0 and all  $u_n$  are set together to one of the wells  $\pm u_0$ .

$$\begin{aligned} \bar{K} + \bar{k} > \frac{1}{2\alpha^2} &\Rightarrow \delta V > 0 && \text{(stable)} \\ \bar{K} + \bar{k} < \frac{1}{2\alpha^2} &\Rightarrow \delta V < 0 && \text{(unstable)} \end{aligned}$$

One reason for the instability is, that the both Morse potentials added back-to-back overcompensate the harmonic next-nearest neighbor coupling and their minima overlap instead of forming a Double-Morse potential. Due to that overlap, the unit cell shrinks to the size of approximately two times the equilibrium distance  $r_0$  in the Morse potential. This must also overcompensate, that in the case of periodic boundaries the unit cell has to be elongated in order to satisfy the constraint (3.14).

### Softening of the Next-Nearest Neighbor Interaction

The possible contraction in the case of a free chain, avoided in the case of periodic boundaries, is not the only effect of adding two Morse potentials arranged back-to-back. The other implication of the Double-Morse potential on the unit cell is a softening of the spring constant  $\bar{K}$  obtained by rescaling the original Hamiltonian. This softened spring constant  $\chi$  can be read out from (3.16) as

$$\chi = \bar{K} - \frac{1}{2\alpha^2}$$

assuming that the much softer q-subchain does not experience this softening.

### 3.3.3 Final Hamiltonian

It is time to summarize the applied rescaling of the initial Hamiltonian (3.1) and write the final Hamiltonian, that will be used for in the following analytic calculations and simulations. The displacements are rescaled by

$$q_n \rightarrow \frac{1}{\beta} q_n \qquad Q_n \rightarrow \frac{1}{\beta} Q_n.$$

While the time and energy are changed as follows:

$$t \rightarrow \frac{1}{\beta} \sqrt{\frac{m}{D}} t \qquad H \rightarrow DH.$$

The rescaled Hamiltonian becomes thereby

$$\begin{aligned} H = \sum_n \left[ \frac{\dot{q}_n^2}{2} + \frac{\mu \dot{Q}_n^2}{2} + \frac{\kappa}{2} (q_{n+1} - q_n)^2 + \frac{\chi}{2} (Q_{n+1} - Q_n)^2 \right. \\ \left. + \left( 1 - \frac{e^{-\frac{\rho n}{2}}}{\alpha} \cosh(u_n) \right)^2 \right]. \end{aligned} \tag{3.17}$$

New spring constants  $\kappa$  and  $\chi$ , determining the weighting between the interaction terms, have been introduced and depend in the following way on the originally introduced parameter  $k$  and  $K$  as the originally introduced spring constants of the central ions and the unit cell, respectively:

$$\kappa = \frac{k}{\beta^2 D} = \bar{k} \qquad \chi = \frac{K}{\beta^2 D} - \frac{1}{2\alpha^2} = \bar{K} - \frac{1}{2\alpha^2}.$$

$\chi$  also includes the prior mentioned softening due to adding two Morse potentials back-to-back, which is assumed to not occur in the much softer subchain of the central ions.  $D$  denotes the dissociation energy and  $\beta$  the curvature of the Morse potential. The last term of (3.17) is the Double-Morse potential, that has been derived in section 3.3. Furthermore, the masses have been merged into the mass ratio  $\mu = \frac{M}{m}$ .

Let us now focus on the Double-Morse potential and what can already be noticed by approximating it.

### 3.3.4 Approximation of the Double-Morse Potential

In this subsection a Taylor expansion of the Double-Morse potential in  $u$  around two possible  $u$  will be made to get a few insights of its behavior. The potential shall be written in the following way to emphasize, that a variation of  $\rho$  is not of interest here. The starting point is

$$V_\rho(u) := (1 - \xi \cosh(u))^2 \quad \text{with} \quad \xi := \frac{e^{-\frac{\rho}{2}}}{\alpha}.$$

As considering only one unit cell, without loss of generality it could be any unit cell of the chain, the subscripts  $n$  are neglected. In the paraelectric phase the Taylor expansion is performed around  $u = 0$ :

$$V_\rho(u)|_0 \approx (\xi - 1)^2 + \xi(\xi - 1)u^2 + \frac{(4\xi^2 - \xi)}{12}u^4 + \mathcal{O}(u^6).$$

The same expansion can be performed in the ferroelectric phase. Then it reveals the barrier height  $(\xi - 1)^2$  between both ground states.

In the ferroelectric phase exhibiting two minima it does make sense to Taylor-expand around  $u = u_0 = \text{arccosh}(\frac{1}{\xi})$ . This gives a good approximation of what happens with small oscillations of the central ion around one of the two wells:

$$\begin{aligned} V_\rho(u)|_{u_0} \approx & (1 - \xi^2)(u - u_0)^2 + \sqrt{1 - \xi^2}(u - u_0)^3 \\ & + \left( \frac{1}{4} + \frac{1}{3}(1 - \xi^2) \right) (u - u_0)^4 + \mathcal{O}((u - u_0)^6). \end{aligned}$$

The existence of a third order term indicates, that the symmetry and degeneracy of both ground states is broken. Additionally, due to the third order term, this would be the limit of the successful used anharmonic linear chain model

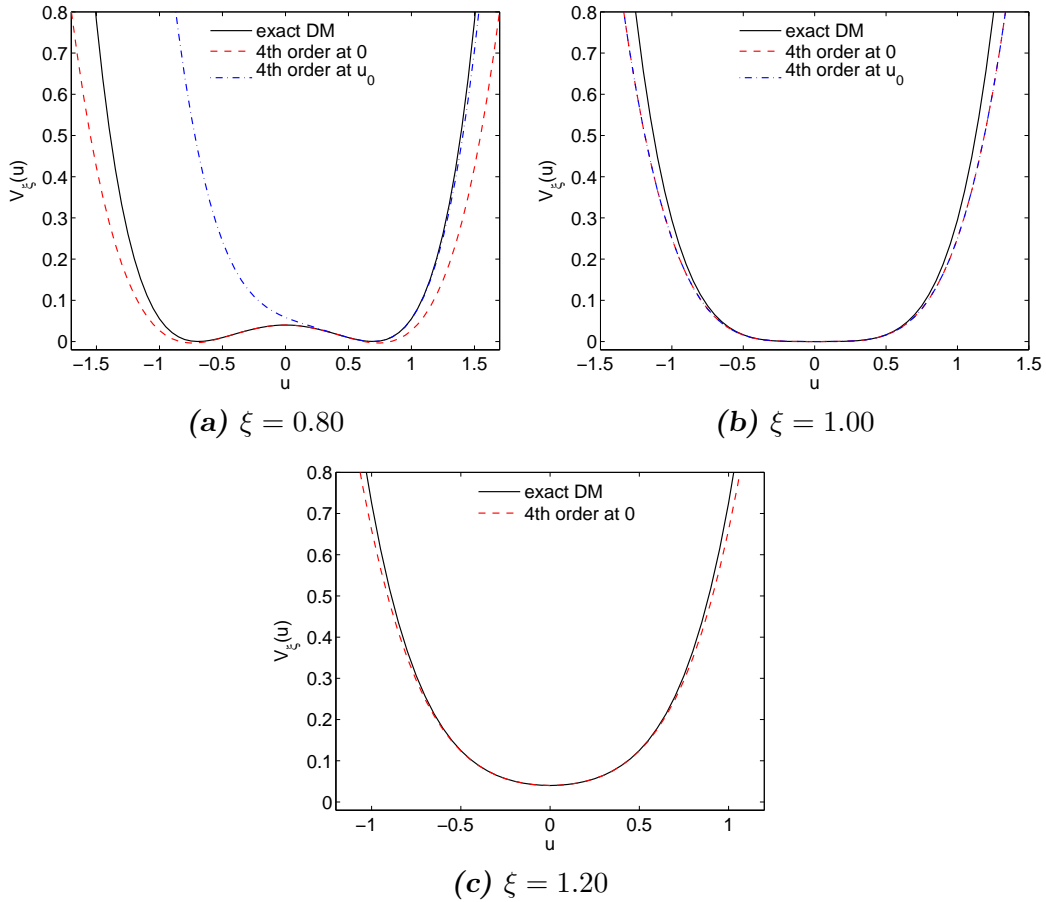


**Figure 3.4:** The 4<sup>th</sup> order approximation of the Double-Morse potential for three different  $\xi$  in comparison to the exact solution. The following  $\xi$  are used beginning from (a) to (c):  $\xi = \{0.80; 1.0; 1.2\}$ . Please refer to the text for more explanations.

[BHS<sup>+</sup>12]. Even though additional harmonic next-nearest neighbor coupling still exists.

The three plots in 3.4 compare the approximations with the exact solution for three different  $\xi = \{0.9, 1.0, 1.1\}$ . Directly at the phase-transition (b) both approximations match and the second order term vanishes. Thus the leading interaction is of fourth order. This means, that for very small oscillations the Double-Morse potential is negligible and the whole dynamics are given by two independent linear chains. For  $\xi = 0.9$  (a), i.e. in the ferroelectric phase, both approximations differ. The expansion around  $u = 0$  keeps the symmetry, but does not yield the exact position of the degenerate ground states. Thus the expansion around  $u = u_0$  is a better option, when studying phonons. For completeness (c) contains the symmetric approximations at  $\xi = 1.1$ , which nicely reflects the potential surface around  $u = 0$ .

Especially the second approximation helps to understand the following small amplitude solutions based on a linearized theory, i.e. only up to second order in the interaction potential is used. Two acoustic modes, one for

each subchain, should be seen at the phase transition. One acoustic and one optical branch is expected to occur otherwise. In contrast, the first approximation reflects the topology of the Double-Morse potential and can be useful when studying large amplitude solutions.

### 3.4 Small Amplitude Solution - Phonon Dispersion Relation

The small amplitude solutions will be derived in this section. This involves deriving the equations of motion from the Hamiltonian with the use of the Hamiltonian equations and approximating the Double-Morse potential to second order around the equilibrium position. In section 3.3.2 it has been shown, that the boundary condition influences the ground state of the chain. In particular the chain contracts depending on the phase transition parameter  $\alpha$ , which is suppressed in the case of periodic boundaries, hence  $\rho_n = 0$ . The equilibrium position of  $u_n$  is  $u_n = 0$  in the paraelectric phase and  $u_n = \pm \operatorname{arccosh}\left(\frac{\alpha}{e^{-\rho_n/2}}\right)$  in the ferroelectric phase.

The equations of motion will then be solved by using a plane wave ansatz corresponding to phonons. The solveability condition gives the phonon dispersion relation  $\omega = \omega(k)$  between frequency  $\omega$  and wavenumber  $k$ , which will be studied around the phase transition. This includes also an investigation of the sound velocity. As mentioned previously, the optical mode will vanish at the phase transition and two acoustic modes occur. This is called a soft mode and will be studied in more detail.

A similar calculation was carried out in [KZ04] for the ferroelectric phase, but in another context and thus with different purposes of the scaling.

#### 3.4.1 Equations of Motion

As summarized in section 3.3.3, the rescaled Hamiltonian (3.17) with Double-Morse potential looks like

$$H = \sum_n \left[ \frac{\dot{q}_n^2}{2} + \frac{Q_n^2}{2\mu} + \frac{\kappa}{2}(q_{n+1} - q_n)^2 + \frac{\chi}{2}(Q_{n+1} - Q_n)^2 + \left( 1 - \frac{e^{-\rho_n}}{\alpha} \cosh(u_n) \right)^2 \right]. \quad (3.18)$$

The dynamic variables  $\rho_n$ , which can be seen as the unit cell deformation, and  $u_n$  denoting the displacement of the central ion with respect to the middle of the unit cell are given as

$$\begin{aligned} \rho_n &= Q_{n+1} - Q_n \\ u_n &= q_n - \frac{1}{2}(Q_{n+1} + Q_n). \end{aligned}$$

They have been initially introduced in section 3.3. The Hamilton equations

$$\dot{p}_n = \ddot{q}_n = -\frac{\partial H}{\partial q_n} \quad \dot{P}_n = \mu\ddot{Q}_n = -\frac{\partial H}{\partial Q_n}$$

with the momentum velocity relation already shown in section 3.2, give the equations of motion

$$\ddot{q}_n = \kappa (q_{n+1} - 2q_n + q_{n-1}) - \frac{\partial}{\partial q_n} \sum_m V_{DM}(u_m, \rho_m) \quad (3.19)$$

$$\ddot{Q}_n = \frac{\chi}{\mu} (Q_{n+1} - 2Q_n + Q_{n-1}) - \frac{\partial}{\mu \partial Q_n} \sum_m V_{DM}(u_m, \rho_m). \quad (3.20)$$

In both cases, the first term is equal to the harmonic linear chain and belongs to the harmonic intra-subchain coupling. The second term, representing the nonlinear inter-subchain coupling, will be approximated separately for each phase. This will be done in the following starting with the ferroelectric phase.

### 3.4.2 Ferroelectric Phase

The ferroelectric phase is characterized by two degenerate positions for the central ion. Without loss of generality the approximation is done only at the right well  $u_0 = \text{arccosh}\left(\frac{\alpha}{e^{-\rho_n/2}}\right)$ . A general  $\rho_0$  is chosen as the equilibrium unit cell deformation. The Taylor-expansion of the Double-Morse potential up to second order looks formally as

$$V(u, \rho) = V(u_0, \rho_0) + \vec{\nabla} V|_{(u_0, \rho_0)} \cdot \begin{pmatrix} u - u_0 \\ \rho - \rho_0 \end{pmatrix} + \frac{1}{2} \begin{pmatrix} u - u_0 \\ \rho - \rho_0 \end{pmatrix}^T \hat{H}|_{(u_0, \rho_0)} \begin{pmatrix} u - u_0 \\ \rho - \rho_0 \end{pmatrix}. \quad (3.21)$$

The second term containing  $\vec{\nabla} V|_{(u_0, \rho_0)}$  vanishes due to expanding around a local extreme. The Hesse-Matrix  $\hat{H}|_{(u_0, \rho_0)}$  containing all second derivatives at the ground state  $\rho = \rho_0$  and  $u = u_0(\rho_0)$  gets

$$\hat{H}|_{(u_0, \rho_0)} = \begin{pmatrix} 2(1 - \xi^2) & -\sqrt{1 - \xi^2} \\ -\sqrt{1 - \xi^2} & \frac{1}{2} \end{pmatrix}.$$

Here,  $\xi = \frac{e^{-\rho/2}}{\alpha}$  is reused. It generalizes the phase transition parameter to account for the two reasons leading to the phase transition as described in section 3.3. The phase transition can either occur due to contracting the chain by external pressure or by varying  $\alpha$ , which determines the form of the Morse potentials and can thus be seen in a real system as temperature dependent. Plugging (3.22) into (3.21) and transposing leads finally to the approximation of the potential  $V(u, \rho)$  around the ground state

$$V(u, \rho) = \frac{1}{2} \left( 2\sqrt{1 - \xi^2}(u - u_0) - (\rho - \rho_0) \right)^2.$$

The sums  $\frac{\partial}{\partial q_n} \sum_m V_{DM}(u_m, \rho_m)$  and  $\frac{\partial}{\partial Q_n} \sum_m V_{DM}(u_m, \rho_m)$  occurring in (3.19) and (3.20) can now be calculated directly. Applying them gives the approximated equations of motion:

$$\begin{aligned} \ddot{q}_n &= \kappa(q_{n+1} - 2q_n + q_{n-1}) \\ &\quad - 4(1 - \xi^2) \left( q_n - \frac{1}{2}(Q_{n+1} + Q_n) - u_0 \right) + 2\sqrt{1 - \xi^2}(Q_{n+1} - Q_n - \rho_0) \\ \ddot{Q}_n &= \frac{1}{\mu}(\chi + 1)(Q_{n+1} - 2Q_n + Q_{n-1}) \\ &\quad + 2\frac{1 - \xi^2}{\mu} \left( q_n + q_{n-1} - \frac{1}{2}(Q_{n+1} + 2Q_n + Q_{n-1}) - 2u_0 \right) \\ &\quad - 2\frac{\sqrt{1 - \xi^2}}{\mu}(q_n - q_{n-1} - \rho_0). \end{aligned}$$

They can be solved by using the plane wave ansatz as done for the simple one and two component linear chain in chapter 2.1, but it has to be modified in two ways. In the first place, it was assumed that the central ion oscillates around the right well. This leads to the additional  $u_0$  term. Secondly, the equilibrium unit cell deformation changes the distance between neighboring oscillators, which can be accounted for by adding  $(n + \frac{1}{2})$  or  $(n\rho_0)$ , respectively.

$$q_n = qe^{i(n+\frac{1}{2})k-i\omega t} + u_0 + \left(n + \frac{1}{2}\right)\rho_0 \quad Q_n = Qe^{ink-i\omega t} + n\rho_0 \quad (3.22)$$

Using the ansatz (3.22) leads to a system of two linear equations with the two variables  $q$  and  $Q$ , which can be written in matrix form

$$\begin{pmatrix} 0 \\ 0 \end{pmatrix} = M_f \begin{pmatrix} q \\ Q \end{pmatrix} = \begin{pmatrix} m_{11}^f & m_{12}^f \\ m_{21}^f & m_{22}^f \end{pmatrix} \begin{pmatrix} q \\ Q \end{pmatrix}, \quad (3.23)$$

where the matrix elements are

$$\begin{aligned} m_{11}^f &= 2\kappa(\cos k - 1) - 2(1 - \xi^2) + \omega^2 \\ m_{22}^f &= \frac{2\chi + \xi^2}{\mu}(\cos k - 1) - 2\frac{1 - \xi^2}{\mu} + \omega^2 \\ m_{12}^f &= \mu \left(m_{21}^f\right)^* = \sqrt{1 - \xi^2}(e^{ik} - 1) \left(\sqrt{1 - \xi^2} + 1\right) + 2(1 - \xi^2). \end{aligned}$$

The super- and subscript  $f$  shall emphasize, that we are in the ferroelectric phase. This system can be solved if  $0 = \det(M_f)$  exists. By calculating this, one gets

$$\begin{aligned} 0 &= \omega^4 + 2 \underbrace{\left[ \left( \kappa + \frac{\chi}{\mu} + \frac{\xi^2}{2\mu} \right) (\cos k - 1) - \frac{1 - \xi^2}{\mu} (1 + \mu) \right]}_{A_f} \omega^2 \\ &\quad + \underbrace{\left( \frac{2\kappa}{\mu} (2\chi + \xi^2) \right) (\cos k - 1)^2 - 4(\chi + \kappa) \frac{1 - \xi^2}{\mu} (\cos k - 1)}_{B_f}. \end{aligned} \quad (3.24)$$

Hence, the dispersion relation can be written in terms of the currently introduced variables  $A_f$  and  $B_f$ :

$$(\omega_{a,o}^f)^2 = -A_f \pm \sqrt{A_f^2 - B_f}.$$

Deeper discussions on that will follow after deriving the dispersion relation within the paraelectric phase.

### 3.4.3 Paraelectric Phase

Only one minimum in the middle of the Double-Morse potential exists for the central ion when considering the paraelectric phase. The Double-Morse potential will therefore be approximated around  $u_0 = 0$ , but still with the same equilibrium unit cell deformation  $\rho_0$  as for the ferroelectric phase. The general procedure remains the same. By doing the same expansion via the Hesse-matrix one arrives at the approximated potential

$$V(u, \rho) \approx \xi(\xi - 1)u^2 + \frac{1}{4}\xi(2\xi - 1)(\rho - \rho_0)^2.$$

The equations of motion become then

$$\begin{aligned} \ddot{q}_n &= \kappa(q_{n+1} - 2q_n + q_{n-1}) - 2\xi(\xi - 1) \left( q_n - \frac{1}{2}(Q_{n+1} + Q_n) \right) \\ \ddot{Q}_n &= \left( \frac{\chi}{\mu} + \frac{\xi(2\xi - 1)}{2\mu} \right) (Q_{n+1} - 2Q_n + Q_{n-1}) \\ &\quad + \frac{\xi(\xi - 1)}{\mu} \left( q_n + q_{n-1} - \frac{1}{2}(Q_{n+1} + 2Q_n + Q_{n-1}) \right). \end{aligned} \quad (3.25)$$

By using the same modified discrete plane wave ansatz (3.22) used for the ferroelectric phase

$$q_n = q e^{i(n+\frac{1}{2})k-i\omega t} + \left( n + \frac{1}{2} \right) \rho_0 \quad Q_n = Q e^{ink-i\omega t} + n\rho_0,$$

but now without  $u_0$  because the central ion oscillates around the middle of the unit cell. Rewriting in matrix form analog to (3.23) gives

$$\begin{pmatrix} 0 \\ 0 \end{pmatrix} = M_p \begin{pmatrix} q \\ Q \end{pmatrix} = \begin{pmatrix} m_{11}^p & m_{12}^p \\ m_{21}^p & m_{22}^p \end{pmatrix} \begin{pmatrix} q \\ Q \end{pmatrix}. \quad (3.26)$$

The matrix elements are now:

$$\begin{aligned} m_{11}^p &= 2\kappa(\cos k - 1) - 2\xi(\xi - 1) + \omega^2 \\ m_{22}^p &= \frac{2\chi + \xi^2}{\mu}(\cos k - 1) - \frac{2\xi(\xi - 1)}{\mu} + \omega^2 \\ m_{12}^p &= \mu(m_{21}^p)^* = \xi(\xi - 1)(1 + e^{ik}) \end{aligned}$$

Finally, by calculating  $0 = \det(M_p)$  one arrives at

$$\begin{aligned}
 0 = \omega^4 + 2 & \underbrace{\left[ \left( \kappa + \frac{\chi}{\mu} + \frac{\xi^2}{2\mu} \right) (\cos k - 1) - \frac{\xi(\xi - 1)}{\mu} (1 + \mu) \right]}_{A_p} \omega^2 \\
 & + \underbrace{\frac{2\kappa(2\chi + \xi^2)}{\mu} (\cos k - 1)^2 - 2 \frac{\xi(\xi - 1)}{\mu} (2\chi + 2\kappa + 2\xi^2 - \xi) (\cos k - 1)}_{B_p}.
 \end{aligned} \tag{3.27}$$

Analogous to the ferroelectric phase the dispersion relation is given as

$$(\omega_{a,o}^p)^2 = -A_p \pm \sqrt{A_p^2 - B_p},$$

where the index  $p$  indicates the paraelectric phase.

Like in the case of a general linear chain with two constituents per unit cell, the dispersion relation shows two branches. One of them is an acoustic branch with a linear behavior for small wavenumber. This branch decreases linearly to zero frequency by decreasing the wavenumber down to zero. This is due to the claimed translational invariance of the chain. Shifting the whole chain shall not change its behavior, nor shall there be any restoring force. The second branch, the optical one, shows a finite frequency at small wavenumber caused by the opposed movement of both constituents in an unit cell.

### 3.4.4 Dispersion Relation

Figure 3.5 shows the dispersion relations at three different  $\xi = \{0.8, 1.0, 1.2\}$  starting from the left column and two different weightings of the interaction terms, one in each row. The coupling constants are  $\bar{K} = \{1, 10\}$  and  $\bar{k} = \{0.2, 2\}$ , where the first value corresponds to the first row and the second value to the second row of plots. Both chains use a mass ratio of  $\mu = 2$ . The second chain has a more rigid next-nearest neighbor coupling. The frequencies at the Brillouin zone center are determined purely by the Double-Morse potential as it is the limit of two non-excited subchains shifted against each other. This gives the opportunity to experimentally determine the curvature  $V''|_{(u_0, \rho_0)}$  of the wells of the Double-Morse potential. All interactions contribute to the vibration frequencies at higher wavenumbers and by approaching the opposite limit at the Brillouin zone boundary, the influence of the interaction within its subchains on the frequencies increases, but the Double-Morse potential still contributes to the frequencies.

The dispersion relation also reveals an avoided crossing of the optical and the acoustic branch. This is not obvious a priori, but will be demonstrated in section 4.4 by simulations.

Directly at the phase transition exist two acoustic modes. The optical branch softens at the Brillouin zone center. This softening will be discussed in more detail in the following.

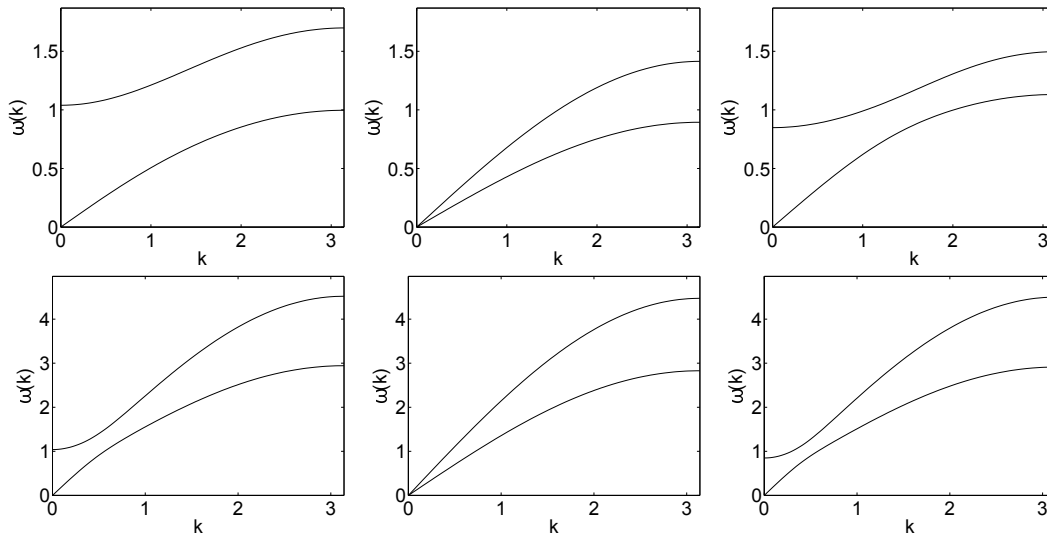


**Figure 3.5:** Dispersion relation at three different  $\xi$  and two different next-nearest coupling constants. The first row belongs to the chain with  $\bar{K} = 1$ ,  $\bar{k} = 0.2$  and  $\mu = 2$ , whereas the second row belongs to  $\bar{K} = 10$ ,  $\bar{k} = 2$  and  $\mu = 2$ . The second chain has a higher influence of the intra-subchain couplings, which leads to higher frequencies at  $k > 0$ .

### Soft Mode Behavior

A typical property of a displacive ferroelectric phase transition is the softening of an optical phonon mode at the Brillouin zone center, see chapter 2.2 or for instance [GM12]. Exactly the same behavior can be found in this model and is shown in figure 3.6 using the same parameters as before. Towards the phase transition at  $\xi = 1$ , either from above or below, the frequency  $\omega(k)$  at the Brillouin zone center  $k \rightarrow 0$  decreases until it reaches zero.

Right at the phase transition, two acoustic modes exist due to the small amplitude approximations done. In section 3.3.4 has been shown, that the leading order of the interaction between both subchains is of fourth order. This implies, that the interaction between both subchains are negligible for small amplitudes. The approximation up to second order does not contribute an inter-subchain interaction and therefore two independent linear chains with one acoustic mode per chain are revealed. This can be demonstrated by setting  $\xi = 1$  either in (3.26) or in (3.23). In both cases the same diagonalized matrix occurs and its eigenvalues can be read off as

$$\omega_q^2 = 2\bar{k}(1 - \cos(k)) \quad \omega_Q^2 = 2\frac{\bar{K}}{\mu}(1 - \cos(k)). \quad (3.28)$$

The dynamics are thus determined by the mass ratio  $\mu$  and by the spring constants  $\bar{k}$  and  $\bar{K}$  introduced previously as the rescaled harmonic next-nearest neighbor interaction. Note, that the softening of the more rigid unit cell chain does not show up here. The dispersion relations (3.28) are similar to the ones derived for the one component linear chain assuming only nearest neighbor interaction (2.3).

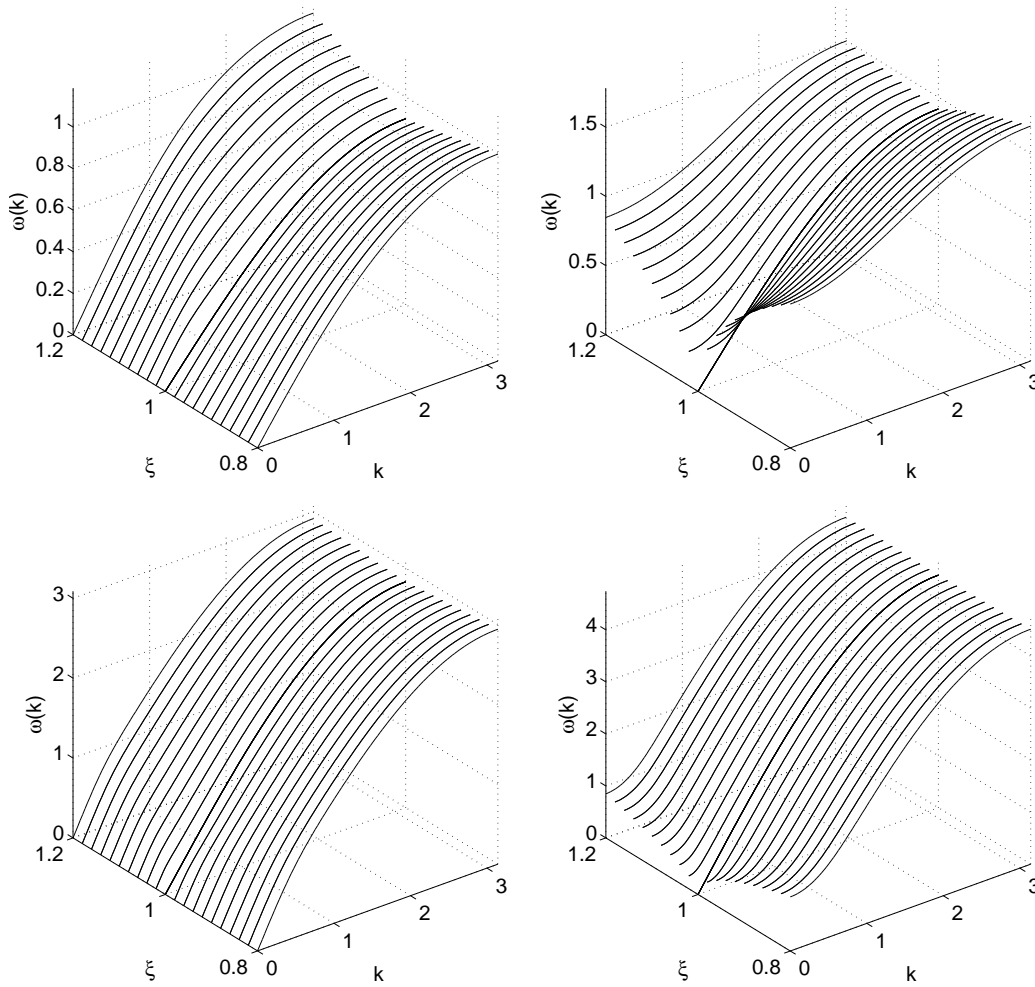


**Figure 3.6:** Lower branch (left) and upper branch (right) of the dispersion relation for various  $\xi$ . The upper row belongs to the chain with  $\bar{K} = 1$ ,  $\bar{k} = 0.2$  and  $\mu = 2$ , whereas the lower row belongs to  $\bar{K} = 10$ ,  $\bar{k} = 2$  and  $\mu = 2$ .

In summary, a softening of an optical mode occurs even at low phonon amplitudes and is thus intrinsically included in this model and its Hamiltonian (3.1) and (3.17), respectively. As a cause of this softening, the avoided crossing moves to smaller wavenumbers and frequencies until it reaches the regime of sound frequencies. Hence, it will influence the measured sound velocity and attenuation around the phase transition. Thus, the following section shall focus on the sound velocity.

### 3.4.5 Sound Velocity

For acoustic phonons with a small wavenumber  $k \rightarrow 0$  the group and the phase velocity are the same, which is caused by its linear dispersion. Sound waves lie in this regime and they therefore correspond to the sound velocity, which is experimentally measurable. The sound velocity can be derived from the

dispersion relation and is slightly different for each phase. Starting point for the derivation is the definition of the group velocity

$$v_s^2 = \frac{\omega^2}{k^2}$$

and the dispersion relation

$$\omega_a^2 = -A + \sqrt{A^2 - B}, \quad (3.29)$$

where  $A$  and  $B$  have the general structure

$$\begin{aligned} A &= a(\cos k - 1) + b \\ B &= c(\cos k - 1)^2 + d(\cos k - 1). \end{aligned}$$

For a small wavenumber  $A$  reaches the finite value  $b$  and  $B$  goes to zero. This allows applying a Taylor series of the square root in (3.29) around  $A$ :

$$\omega_a^2 \approx -A + A - \frac{1}{2A}B. \quad (3.30)$$

In the same sense,  $(\cos k - 1)$  can be approximated up to second order. The leading order of  $(\cos k - 1)^2$  is four and this term will thus be neglected. Collecting all terms of lowest order independently in nominator and denominator leads to

$$v_s^2 = \frac{\omega_a^2}{k^2} \approx \frac{d}{4b}.$$

Note, that the velocity is also dimensionless due to the rescaling of the Hamiltonian. It corresponds to the number of unit cells per dimensionless time.

The equations (3.24) and (3.27) give the expressions for  $d$  and  $b$  for each phase, so that the sound velocities for both phases in the  $k \rightarrow 0$  limit are obtained as

$$\begin{aligned} v_{s,f} &= \sqrt{\frac{\chi + \kappa}{\mu + 1}} = \sqrt{\frac{\bar{K} + \bar{k} - \frac{\xi^2}{2}}{\mu + 1}} \\ v_{s,p} &= \sqrt{\frac{\chi + \kappa + \xi^2 - \frac{\xi}{2}}{\mu + 1}} = \sqrt{\frac{\bar{K} + \bar{k} + \frac{\xi^2 - \xi}{2}}{\mu + 1}}. \end{aligned} \quad (3.31)$$

The velocities within both phases decrease slightly when going towards the phase transition and exhibit a jump right at the phase transition. Special care is necessary at that point. The phase transition occurs at  $\xi = 1$  and simultaneously  $A$  vanishes. That negates the validity of the approximation of the square root done to get from equation (3.29) to (3.30). But from section 3.4.4 is known, that exactly at the phase transition the chain behaves like two independent chains with its corresponding dispersion relations (3.28). Hence, two distinct sound velocities  $v_{s,q} = \sqrt{\bar{k}}$  and  $v_{s,Q} = \sqrt{\bar{K}/\mu}$  exist. They are similar to (2.4) derived for the one component linear chain.

In conclusion, it has been shown that a discontinuity at the phase transition exists in two respects. The left limit as well as the right limit are distinct from

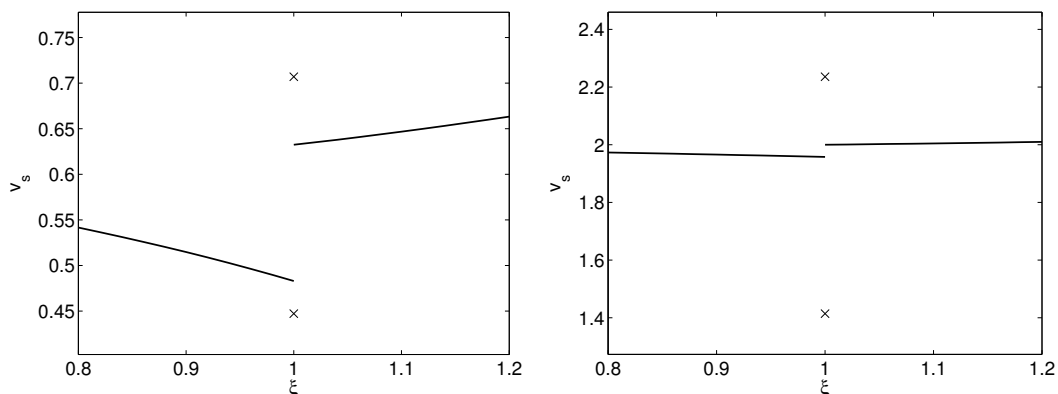


**Figure 3.7:** Analytically calculated phonon sound velocities and their dependence on  $\xi$ . Directly at  $\xi = 1$  two independent linear harmonic chains exist and thus two sound velocities marked with a cross. The upper cross belongs to the  $Q$ -subchain and the lower one to the  $q$ -subchain. The left plot is calculated for  $\bar{K} = 1$ ,  $\bar{k} = 0.2$  and  $\mu = 2$ , whereas for the right plot  $\bar{K} = 10$ ,  $\bar{k} = 2$  and  $\mu = 2$  is chosen. Stronger intra-subchain coupling leads generally to higher velocities and the jump at the phase transition is smaller due to a lower influence of the Double-Morse potential.

each other and additionally they differ from the value directly at the phase transition. This behavior is shown in Figure 3.7. The two sound velocities at  $\xi = 1$  are marked with a cross. Two same two sets of parameter for the chain as for the dispersion relation are used. The left picture belongs to the soft next-nearest neighbor couplings and a strong influence of the nonlinear Double-Morse potential. This shows up in a more pronounced difference between the sound velocity in each phase as well as in the steepness within each phase. For the more rigid chain, the sound velocity is almost constant within the plotted  $\xi$  range except at the phase transition. Here, both subchains have the same ratio between the velocities within each subchain. The Double-Morse potential has no influence on that.

### 3.5 Large Amplitude Solution - Domain Wall

Large amplitude solutions have been studied extensively in the literature including mostly numerical investigations [ZPS91, SZ91, KZ02, KZ04]. Here I want to follow briefly the analytical derivation of [ZPS00]. The equations are slightly modified in order to account for the scaling and nomenclature used in this thesis. The equations of motion (3.19) and (3.20) serve as the starting point. Applying a continuum approximation to the equations of motion and changing to the moving reference frame  $\phi = x - vt$ , thus the time derivatives

transform as  $\ddot{q} \rightarrow v^2 q_{xx}$  and  $\ddot{Q} \rightarrow v^2 Q_{xx}$ , leads to [ZPS00, (14)]

$$\begin{aligned} (c_0^2 - v^2)q_{xx} &= \frac{\partial}{\partial u} V(u, \rho) \\ (v^2 - c_0^2)q_x + \mu(v^2 - v_0^2)\rho &= \frac{\partial}{\partial \rho} V(u, \rho), \end{aligned}$$

where  $c_0 = \sqrt{\kappa}$  and  $v_0 = \sqrt{\chi/\mu}$  denote the sound velocity in the q- and the Q-sublattice, respectively. This set of ordinary differential equations can be solved analytically by simplifying the Double-Morse potential with a potential of fourth order [ZPS00, (9)]

$$V(u, \rho) = \underbrace{(1 - \xi)^2}_{\epsilon_0} \left( 1 - \frac{u^2}{u_0^2} + \frac{\rho}{u_0^2} \right)^2,$$

where  $u_0 = u_0(\rho)|_{\rho=0} = \text{arccosh}(1/\xi)$  is the position of the well when the chain is neither contracted nor expanded.  $\epsilon_0$  is the barrier height separating the two wells of the Double-Morse potential. The analytical solution is a two-component topological soliton and either a kink or an antikink [ZPS00, (18)]

$$u(\phi) = \pm u_0 \tanh(\gamma\phi) \quad \rho = \rho_0 \cosh^{-2}(\gamma\phi) \quad (3.32)$$

with the substitutions

$$\begin{aligned} \gamma^2 &= \frac{1}{u_0^2} \frac{1 + \mu \frac{v_0^2 - v^2}{c_0^2 - v^2}}{\frac{1}{u_0^4} + \frac{\mu}{2\epsilon_0}(v_0^2 - v^2)} \\ \rho_0 &= u_0^2 \frac{2\epsilon_0 + u_0^2 \gamma^2 (v^2 - c_0^2)}{2\epsilon_0 \pm u_0^3 \gamma (v^2 - c_0^2)} \end{aligned} \quad (3.33)$$

The plus (minus) sign in equation (3.32) and (3.33) correspond to the kink (antikink) solution. They are plotted for three different velocities in figure 3.8.

Several important features show up in this solution. The first one to notice is, that the width of a kink, thus a domain wall, depends on its velocity. Secondly, these solitons exist only within two velocity regimes:

$$\begin{aligned} 0 \leq v &\leq \sqrt{\frac{\chi + \kappa}{1 + \mu}} \\ v_0 \leq v &\leq \sqrt{\frac{\chi}{\mu} + \frac{2\epsilon_0}{\mu u_0^4}} \end{aligned}$$

The upper boundary of the first band occurred already in (3.31) as the sound velocity within the ferroelectric phase. The second velocity regime allows velocities larger than the velocity in the more rigid Q-sublattice. It corresponds to supersonic solitons, i.e. domain walls which propagate faster than the sound in an isolated Q-sublattice. For subsonic domain walls, the unit cell is either strained around the kink soliton or compressed around the antikink soliton. In the case of supersonic domain walls, the unit cell is compressed in either of them.

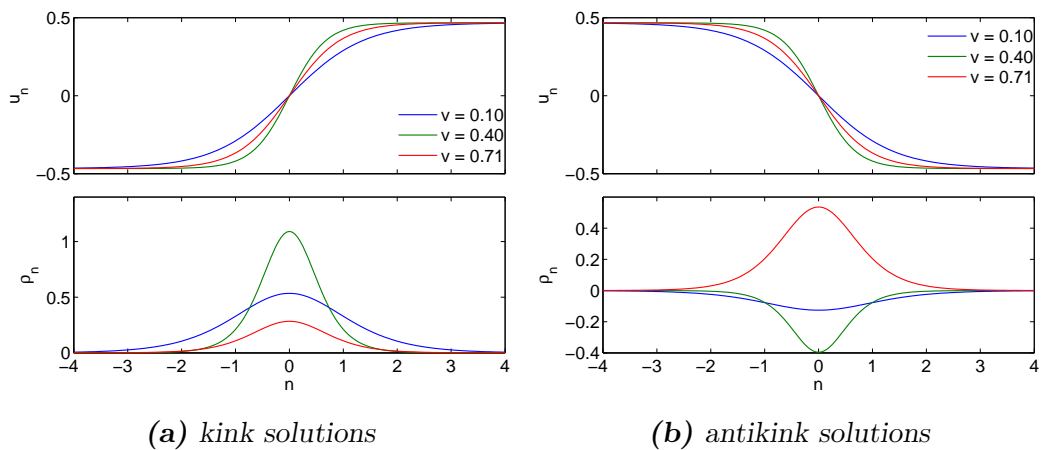


**Figure 3.8:** Analytical kink (a) and antikink (b) solutions at three different propagation velocities  $v = \{0.1, 0.4, 0.71\}$ . The first two velocities are subsonic, i.e. lower than the sound velocity of  $v_s \approx 0.52$ . The last velocity is supersonic with an velocity slightly larger than sound velocity in an isolated Q-sublattice:  $v_Q = 0.707$ . The other parameters are chosen as:  $\xi = 0.9$ ,  $\bar{K} = 1$ ,  $\bar{k} = 0.2$  and  $\mu = 2$ .

# Chapter 4

## Simulating Dynamics

Numerical investigations help to go beyond the scope of the linear theory, which has been studied in the previous chapter. For instance, it is possible to excite pulses with different amplitudes and observe their dynamics as will be done in section 4.3. By varying the amplitudes, the analytical result will be reflected on the one side, whereas nonlinear effects will be seen on the other side of the amplitude range. The temporal evolution of the pulse profile will greatly differ depending on the amplitude and phase. The same holds for the sound velocity as an experimentally observable quantity. It will be studied as the velocity of the pulse.

Another often experimentally examined feature is the dispersion relation. The section 4.4 is devoted to the dispersion relation obtained numerically ranging also from linear regime up to the nonlinear one. Here a system closer to thermal equilibrium is used, as the initial excitation energy is homogeneously spread over the whole chain. The nonlinear regime will show as a spreading of the dispersion relation by approaching higher energy densities.

A more systematic view on the nonlinear influence follows in section 4.5. The first one is a quantification of the nonlinear or chaotic behavior by using the maximum Lyapunov exponent. It uses again a state with a homogeneous energy density.

Finally in 4.6, more details on the relaxation towards thermal equilibrium, i.e. thermalization, are revealed. One starts with a far-from-equilibrium state with only two excited phonon modes. Due to the nonlinear interaction potential, these phonon modes will couple. This coupling is expected to be large close to the phase transition.

However, before one can start with the simulation, the simulations itself and some technical aspects shall be shortly introduced in the first section 4.1. This includes the equations of motion. A very important point is the initial condition. Some efforts have to be made on this topic in section 4.2.

### 4.1 Simulation Procedure

The numerical integration has been written in C++ and is called as a .mex function within MATLAB. A MATLAB script provides the preparation of the

initial state and commits all parameters to the .mex file including a time vector. This time vector defines the times at which the .mex function takes a snapshot of the actual state until it reaches the last value in the time vector. A matrix including all displacements and velocities at these times is returned to the script and can be evaluated including spatial or temporal Fourier transforms depending on what in particular is investigated.

The differential equation to simulate is of second order in time. It is basically a sum of forces occurring for each oscillator based on its actual displacements  $Q_n$  and  $q_n$ :

$$\begin{aligned}\mu\ddot{Q}_n &= \bar{K}(Q_{n+1} - 2Q_n + Q_{n-1}) + F_M(Q_n - q_{n-1}) - F_M(q_n - Q_n) \\ \ddot{q}_n &= \bar{k}(q_{n+1} - 2q_n + q_{n-1}) + F_M(q_n - Q_n) - F_M(Q_{n+1} - q_n)\end{aligned}$$

$\bar{K}$  and  $\bar{k}$  are the rescaled spring constants and  $\mu$  is the mass ratio. They have been introduced in section 3.2.1.  $F_M$  is the force acting on two neighboring constituents caused by the Morse potential

$$F_M(x) = -\frac{\partial}{\partial x}V_M(x) = -\frac{e^{-x}}{\alpha} \left(1 - \frac{e^{-x}}{2\alpha}\right).$$

Two boundary conditions will be used. One of them is the periodic chain with periodic boundaries implemented by adding the following fictitious constituents at the beginning and end of the chain:

$$\begin{aligned}Q_{N+1} &= Q_1 & q_{N+1} &= q_1 \\ Q_0 &= Q_N & q_0 &= q_N.\end{aligned}$$

The second one is the free chain with open boundary condition. It can be implemented again by adding two fictitious constituents at the beginning and end of the chain, but now with the substitution

$$\begin{aligned}Q_{N+1} &= Q_N & q_{N+1} &= q_N \\ Q_0 &= Q_1 & q_0 &= q_1,\end{aligned}$$

where  $N$  is the number of unit cells of the chain.

This gives a differential equation system with  $2N$  equations. They are numerically integrated by a fourth order Nyström method with six function calls [LR05, Ch. 6.2]. It belongs to the parted Runge-Kutta Methods. The key feature of this method is its symplecticity implying that the total energy of the chain is conserved up to a small error. The temporal evolution of the relative error is illustrated in figure 4.1. A step size of  $h = 0.1$  gives a relative error of  $< 10^{-7}$  and seems to be a reasonable choice for the simulations.

## 4.2 Initial Condition

Before getting to the simulations, it is important to discuss the preparation of the initial state of the chain. The basic idea is to set the displacements  $q_n$

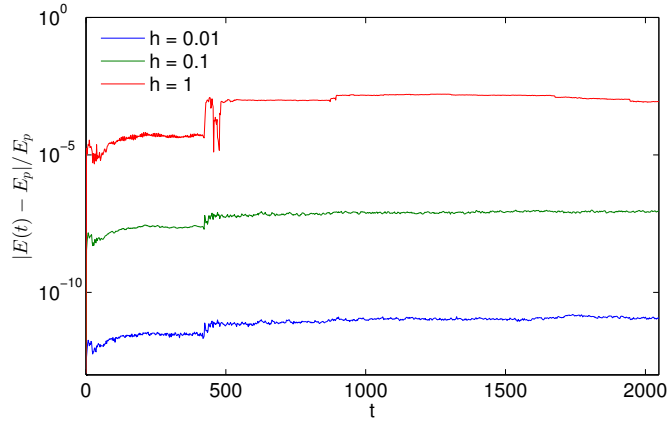


**Figure 4.1:** Temporal evolution of the error of the total energy relative to the pulse energy. The dynamics are simulated with a fourth order Nyström method at three different step sizes  $h = \{0.01, 0.1, 1\}$ . The same chain as in section 4.3.3 and following with an high energy pulse  $E = 10$  is used. The step before  $t = 500$  is caused by the collision of two pulses. See also section 4.3.

and  $Q_n$  in the lowest energy state, which is also a steady state with initial velocities set to zero.

The dynamic variables  $u_n$  for the displacement of the inner ion and  $\rho_n$  have been introduced in section 3.3 as:

$$\begin{aligned}\rho_n &= Q_{n+1} - Q_n \\ u_n &= q_n - \frac{1}{2}(Q_{n+1} + Q_n)\end{aligned}$$

They have been used to show analytically, that this ground state depends on the boundary conditions. Periodic boundaries require that  $Q_{N+1} = Q_1$ . Hence the sum over all unit cell deformations  $\rho_n$  has to be zero. This leads to non-deformed unit cells as a ground state, which has been derived in 3.3.2. In the same section it has been revealed, that open boundaries result in a polynomial dependence (3.11) and (3.13) of  $\rho_0$  on  $\xi$  with the longest contraction at the phase transition. Remember the definition (3.10) of  $\xi$  connecting  $\rho_0$  and  $\alpha$  to one phase transition tuning parameter. The phase transition occurs at  $\xi = 1$  either due to changing  $\rho_0$  or by varying  $\alpha$ . For  $\xi < 1$  the chain is in ferroelectric phase and it is in the paraelectric phase for  $\xi > 1$ . The results are summarized as

$$\rho_0 = 0 \qquad \xi = \frac{1}{\alpha}$$

for the periodic chain and as

$$\rho_0^{fe} = -\frac{\xi^2}{2(\bar{K} + \bar{k})} \quad \rho_0^{pe} = \frac{\xi^2 - 2\xi}{2(\bar{K} + \bar{k})} \quad \xi = \frac{1}{\alpha} e^{-\frac{\rho_0}{2}} \quad (4.1)$$

for the free chain. A differentiation of the ferroelectric and paraelectric phase is necessary. They are denoted with the subscripts  $fe$  and  $pe$ .  $\bar{K}$  and  $\bar{k}$

are the rescaled spring constants of the next-nearest neighbor interactions. Irrespective of the boundary, the ground state position of the central ion is either zero in the paraelectric phase or  $u_0 = \operatorname{arccosh}(1/\xi)$  in the ferroelectric case.

The contraction (4.1) of the free chain can be numerically proven for sufficiently long chains. The analytically derived contractions in both phases, (3.11) and (3.13), are plotted in figure 4.2a together with the numerical results for a chain with 512 and a chain with 32 unit cells. They agree nicely for the long chain, but significant differences exist for the 32 unit cell short chain. This is caused by boundary effects, which have been neglected in the derivation. They are illustrated in the upper figure of 4.2b for  $\xi = 1$ , where the spatial unit cell deformation after the relaxation for both chain lengths are plotted. To ensure a better comparability, the position is normalized to  $[0, 1]$ . The contraction is lower at both ends than the contraction in the middle, which approaches the theoretical value of  $\rho_0$  plotted as a dotted line. Relative to the whole chain, the borders have a larger influence on the small chain.

The numerical procedure for getting the ground state is as follows. The chain is initially prepared with  $\rho_n = 0$  and  $u = -u_0$ .  $\alpha$  is calculated by assuming that the analytical  $\rho_0$  for the free chain holds. The simulation runs  $2^{14}$  time steps with  $2^{13}$  interrupts at which the velocities are set to zero. This leads to a decreasing of the total energy and therefore to a relaxation. Just for validation, the temporal evolution of the kinetic energy density is plotted in the lower figure of 4.2b. For any numerical investigation of the free chain, this relaxation process will be done before adding the excitation and starting the simulation.

In summary the general initial displacements of sufficiently long chain are

$$\rho_n = \rho_0 \qquad u_n = -u_0.$$

Thus the displacements used in the simulation are given by

$$q_n = \left(n + \frac{1}{2}\right) \rho_0 - u_0 \qquad Q_n = n\rho_0. \quad (4.2)$$

An additional freedom of the center of mass motion of the whole chain exists, but is, without loss of generality, neglected. The same holds for the center of mass velocity, which is also set to zero.

With a chain being in the lowest energy state one can start to think about the excitation. Two ways are possible. The excitation could be either a perturbation in the displacements or alternatively a velocity could be added. With the nonlinear interaction terms and the requirement to change the energy of an excitation in a controlled way, it is favorable to use the second way of adding initial velocities. Different excitations will be investigated. They range from independent identically distributed random noise over a pulse with a gaussian spatial distribution to periodic excitations. The first one is closer to thermal equilibrium, whereas the latter two resemble far-from-equilibrium states. In all cases the energy or the energy density is used as a control parameter to manipulate the influence of the nonlinearity. The excitation used in particular will be introduced at the point there are used.

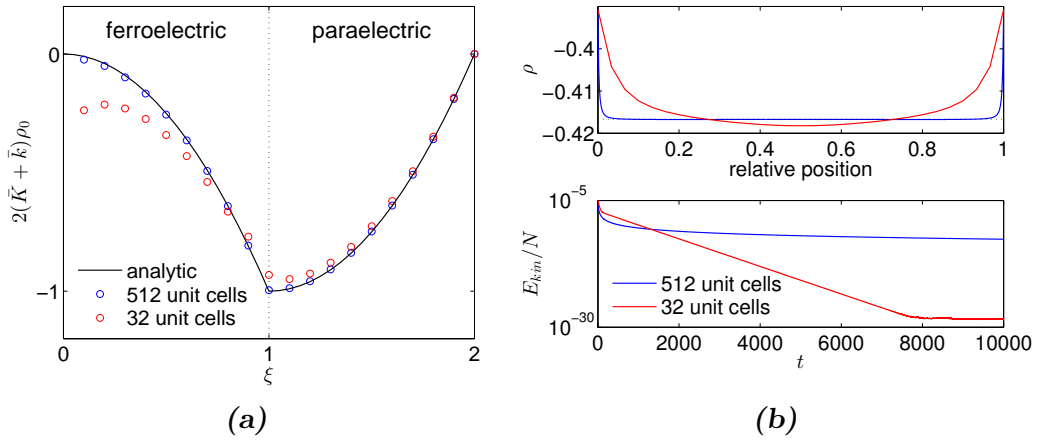


**Figure 4.2:** The left plot (a) shows the contraction of a free chain. The solid black line resembles the analytical solution, whereas the circles denote the numerically calculated contraction for two different chain length of 512 unit cells (blue) and 32 (red). The upper plot of (b) illustrates the difference in the unit cell deformation  $\rho_n$  depending on the relative position in the chain with respect to the analytical value (dotted black line). The saturation of the chain is shown in the lower plot in terms of the kinetic energy in the chain.

## 4.3 Pulse Propagation

### 4.3.1 Pulse Excitation

As mentioned before, the initial displacements are given in the general form (4.2) valid for both boundary conditions and the excitation is done by adding a spatial velocity distribution. The shape of the pulse shall be of a gaussian profile given by

$$\dot{q}_n = \epsilon_q e^{-\frac{(n+\frac{1}{2}-n_0)^2}{2\sigma^2}} \quad \dot{Q}_n = \epsilon_Q e^{-\frac{(n-n_0)^2}{2\sigma^2}}, \quad (4.3)$$

where the initial position of the pulse  $n_0$  and the pulse width  $\sigma$  shall be the same for both subchains. The additional term  $\frac{1}{2}$  takes care of the relative shift of the q-subchain with respect to the Q-subchain. These initial velocities would lead to a moving chain as the mean velocity is different from zero. In order to avoid this, all velocities are subtracted by its mean. This is not an issue because all dynamics will be investigated with the dynamic variables  $\rho_n$  and  $u_n$ . These variables only show the relative dynamics and hence they are not influenced by the mean velocity of the whole chain. However, a small contribution to the total energy exists as the kinetic energy of the center of mass motion vanishes.

Using the variables  $\rho_n$  and  $u_n$ , the initial velocities (4.3) change to

$$\dot{u}_n = e^{-\frac{\nu_n^2}{2\sigma^2}} \left( \epsilon_q - \epsilon_Q e^{-\frac{1}{8\sigma^2}} \cosh\left(\frac{\nu_n}{2\sigma^2}\right) \right) \quad (4.4)$$

$$\dot{\rho}_n = -2\epsilon_Q e^{-\frac{\nu_n^2 + \frac{1}{4}}{2\sigma^2}} \sinh\left(\frac{\nu_n}{2\sigma^2}\right), \quad (4.5)$$

whereas  $\nu_n$  has been introduced as  $\nu_n := n + \frac{1}{2} - n_0$  in order to simplify the expression.

It is possible to manipulate whether more acoustic phonons or more optical phonons will be excited by varying  $\epsilon_q$  and  $\epsilon_Q$ . E.g. by setting  $\epsilon_Q$  zero the initial  $\dot{\rho}_n$  vanishes and only optical phonons will be excited. However, the opposite is only possible in the limit of an infinitively wide pulse, which is the case for  $\sigma$  approaching infinity.

The following investigations are all done with a  $\sigma$  of 5 corresponding to a full width half maximum of approximately 11.8 unit cells. Each quoted energy denotes the integrated energy of the pulse

$$E = \sum_{n=1}^N \frac{\dot{q}_n}{2} + \frac{\mu \dot{Q}_n}{2}.$$

### 4.3.2 Temporal Pulse Profile Evolution

The main focus of this section is the temporal change of the pulse shape. After exciting a pulse in the middle of a 512 unit cell long chain by adding the previously mentioned velocity distribution, its space time map is computed for a total time of 1024. Remember that the time is dimensionless due to the rescaling applied in section 3.2.1. The temporal evolution of the unit cell deformation and the displacement of the central ion can be derived from the space time map with the help of (3.5) and (3.6). Figures 4.3, 4.5 and 4.7 show such maps of  $\rho_n$  (upper plot) and  $u_n$  (lower plot) for different phase parameter  $\xi$  and excitation energies  $E$ . There are simulated using the following parameter. The rescaled next-nearest neighbor spring constants are  $\bar{K} = 1$ ,  $\bar{k} = 0.2$ . The mass ratio is  $\mu = 2$ . These values for the spring constants lie at the lower border for a stable unit cell and assess the influence of the Double-Morse potential.

In general, the excitation leads to two pulses. One pulse is tensile and propagates from the middle towards zero, the left end of the chain. The second pulse propagates to the right end and compresses the unit cell. The pulse profiles are plotted in figures 4.4, 4.6 and 4.8 for two times marked as the dashed and the solid green line within the corresponding space-time maps 4.3, 4.5 and 4.7 to reveal more details. The edge of the pulse is determined by the first  $\rho_n$  beginning from left for the tensile pulse or from right for the compressive pulse, that exceeds a certain threshold. Here this threshold is set to one tenth of the maximal compression or tension and is denoted as the origin of the x-axis in all pulse profile plots and as a cross in the space-time maps. The arrows illustrate the propagation direction. Similar to the space

time map, the dotted lines belong to the first time  $t = 50$ , while dashed and solid lines belong to the second time  $t = 250$ . Additionally both boundary conditions will be compared at the end of this section. That is why a further differentiation in blue for the periodic chain and red for the free chain exists.

The features will be described in the following order. First a qualitative overview of the pulse propagation and its temporal evolution is investigated for one  $\xi$  each in the ferroelectric phase, at the phase transition and in the paraelectric phase. The next part continues with a more systematic view on the pulse velocity. At last comes a evaluation of the differences between free and periodic chain.

### 4.3.3 Ferroelectric Phase

The ferroelectric phase, discussed here for  $\xi = 0.95$ , exhibits two ground states separated by a potential barrier. The excitation energy and thus the amplitude determines which phenomena occur. In the case of low energies, plotted for  $E = 0.1$  in figure 4.3a, the small amplitude approximation holds and the pulse propagates regularly with only a slight dispersion of the compressive pulse. In contrast, domain walls are introduced, when exciting with sufficient energy to overcome the potential barrier. An energy of  $E = 10$  is chosen and the corresponding space-time map plotted in figure 4.3b. The interaction between domain walls and the pulse lead to a fast decay of the pulse and the dynamics get rather chaotic. Note, that the sound velocities for compressive and tensile part differ in the high energy case. The compressive part propagates faster than the tensile part.

The pulse profiles are shown the figures 4.4. The upper row belongs to the low energy excitation with the left propagating tensile pulse in the left column and the right propagating compressive pulse in the right column.

The tensile pulse shows a very regular behavior with a gaussian shape and almost no difference to the profile at the earlier time, whereas the compressive pulse exhibits dispersion and a widening of the pulse. An attenuation of the amplitude can also be noticed. In the ferroelectric phase, the tension leads to an additional separation of the two degenerate wells in the Double-Morse potential. This gives rise to the pulse in the central ion chain  $u_n$  with an increased absolute value. Analogously, a compressive pulse leads to a pulse with a decreased absolute value.

The high energy excitation, shown in figures 4.4c and d, is sufficient to induce nonlinear effects. The tensile pulse gets narrower and grows in amplitude. In other words, the pulse fronts steepen up. A second pulse with lower amplitude follows. This behavior seems to be similar to the splitting of an arbitrary pulse into solitons appearing in the Korteweg-de Vries equation and accordingly for water waves in a channel or river. In fact, the system has the same ingredients: A nonlinearity responsible for an amplitude dependent propagation velocity causing the steepening and dispersion.

The compressive pulse has an amplitude sufficient to change the potential of the central ion from two separate ground states to only one. In other words,

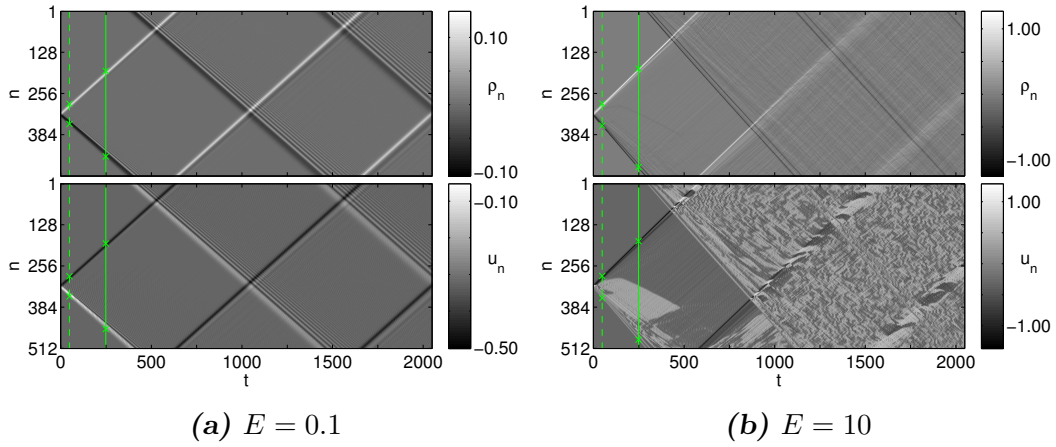


**Figure 4.3:** The space-time maps of the unit cell deformation  $\rho_n$  and the central ion displacement with respect to the middle of the unit cell  $u_n$  within the ferroelectric phase  $\xi = 0.95$  and with two different pulse energies.

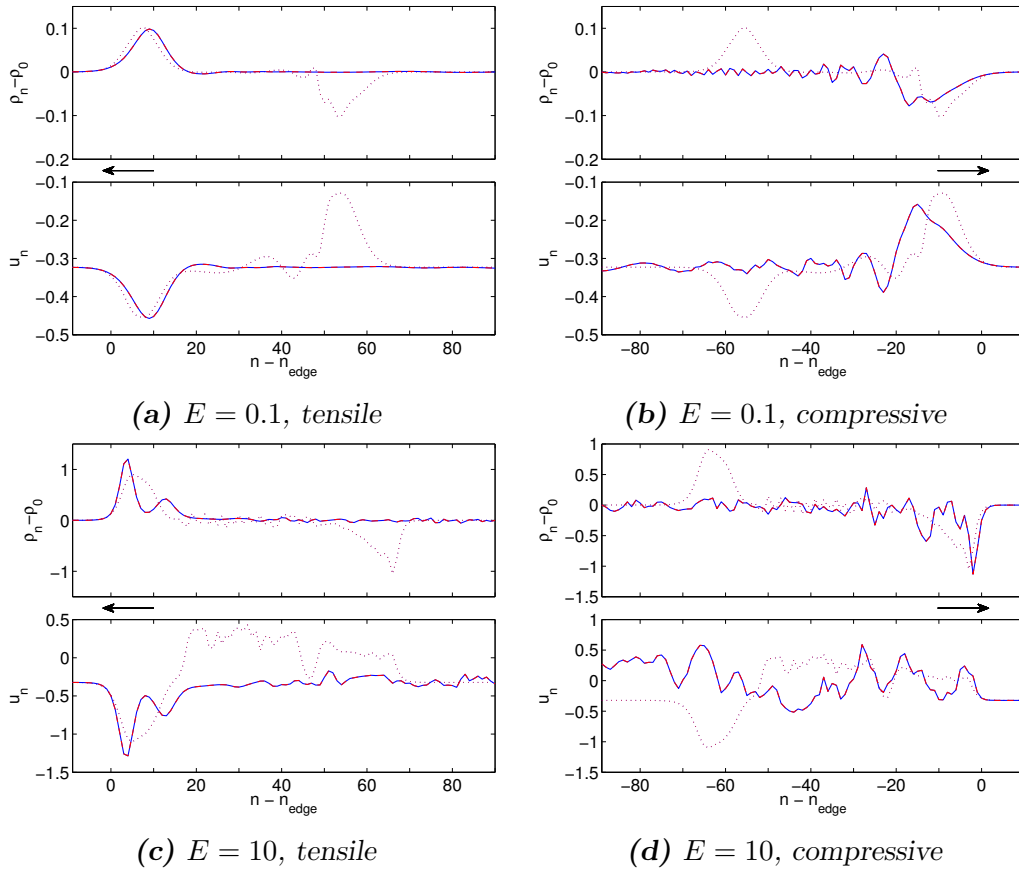


**Figure 4.4:** Pulse profiles corresponding to the times illustrated as dashed and solid line within the space-time maps of figure 4.3. The upper plot shows the pulse profile of  $\rho_n$  and the lower plot shows pulse profile of the central ion  $u_n$ . The origin of the x-axis belong to the cross in 4.3. The black arrow marks the propagation direction. Periodic boundaries are used for the red lines and open boundaries for the blue lines.

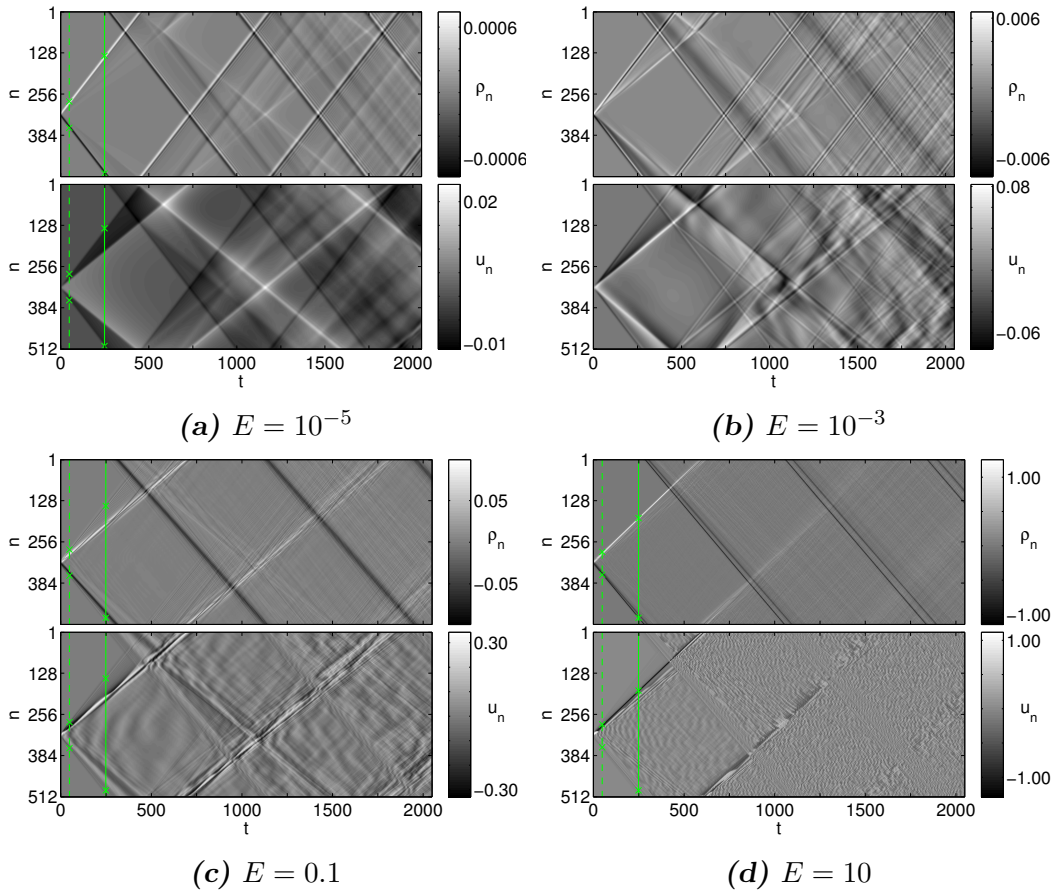


**Figure 4.5:** The space-time maps of  $\rho_n$  and  $u_n$  directly at the phase transition  $\xi = 1.0$  and with four different pulse energies.

a transition from the ferroelectric to the paraelectric phase takes place within the pulse. This transition seems to be responsible for the strong fluctuations in both subchains, which follow the pulse. The central ion oscillates several times from one well to the other until it resides in the opposite well. Thus, the pulse induces domain walls. The pulse itself gets narrow and grows slightly in amplitude. Hence, also a steepening occurs.

#### 4.3.4 Phase Transition

The phase transition occurs at  $\xi = 1$ . The behavior changes depending on the pulse amplitude and energy. To illustrate this, four different pulse energies  $E = \{10^{-5}, 10^{-3}, 0.1, 10\}$  are chosen. Their space-time maps are shown in figure 4.5. In the case of the lowest energy, two different characteristic velocities exist. One fast and regular propagating pulse within the Q-subchain visible in the  $\rho_n$  plot. The second velocity can be noticed in the  $u_n$  plot implying a slower pulse within the chain of central ions. The pulses interact only weakly. This behavior can be explained by the coupling between both subchains, which is of fourth order and thus very small for such low energies. Remember the analytic approximation of the Double-Morse potential in section 3.3.4. When going to

higher energies and amplitudes, the interaction gets stronger and the dynamics become chaotic. At an energy of  $E = 10^{-3}$  the influence of both subchains is still visible, but a collective compressive pulse appears. This pulse is even more pronounced and stable at a pulse energy of  $E = 0.1$ . However, the tensile pulse decays rapidly and the dynamics of the inner ion start to be rather chaotic. The compressive pulse splits at the highest energy of  $E = 10$ . The dynamics of the inner ion are strongly chaotic except around the compressive pulse. This can be explained by remembering what happens with the Double-Morse potential if the unit cell is compressed. These unit cells get off the phase transition into the regime of one well and a second order interaction between the subchains arise leading to smaller oscillations of the central ion around  $u_n = 0$ . In the case of a tensile stress, two minima exist enabling stronger fluctuations and a strong attenuation.

The pulse profiles for the three energies  $E = 10^{-5}$ ,  $0.1$  and  $10$  are plotted in figure 4.6. The first row includes the lowest pulse energy  $E = 10^{-5}$ . The shape of the pulse in the unit cell deformation does not alter much between both times. Tensile and compressive pulse propagate regularly. A second pulse propagates in the chain of the central ions. It is slower and lags behind the first one. Comparing  $\rho_n$  and  $u_n$ , the faster pulse is more pronounced in  $\rho_n$  and thus in the Q-subchain, whereas the slower pulse is more pronounced in  $u_n$  and thus in the q-subchain. This confirms the idea of two almost non interacting linear chains.

At an energy of  $E = 0.1$ , both, the compressive and the tensile pulse, show strong deviations from the initially excited gaussian pulse. The tensile, left propagating, pulse has two parts, a faster low amplitude one with nearly no influence on the central ion displacements and a second part with higher amplitude, that propagates more slowly, but with a stronger displacement of the central ion. This part would show a stronger polarization, when including charge effects. But remember, that charges are not directly included in the model. They are included indirectly by contributing to the effective potential. The compressive, right propagating, pulse does not show such a pronounced sectioning, but a tendency is still noticeable. Still, the edge propagates faster than the peak. This reveals a strong asymmetry, which will be confirmed by studying the pulse velocities more systematically. In addition to the unit cell deformation, the amplitude of the inner ion is larger for the left propagating tensile pulse. This can again be explained by the effect on the Double-Morse potential. Tension leads locally to a transition in the ferroelectric phase. Hence, the central ion starts to move towards and to oscillate around one of the two wells and a higher amplitude is achieved. On the contrary, the compressive pulse leads to a stabilization of the one well in the middle of the unit cell, explaining also, why the pulse in the central ion displacement follows the compressive pulse.

The tensile pulse excited with the highest energy of  $E = 10$  exhibits the same self-steepening as in the ferroelectric phase, but without the second pulse and with stronger fluctuations, especially in the central ion subchain. The chain within the pulse is effectively in the ferroelectric phase with an high

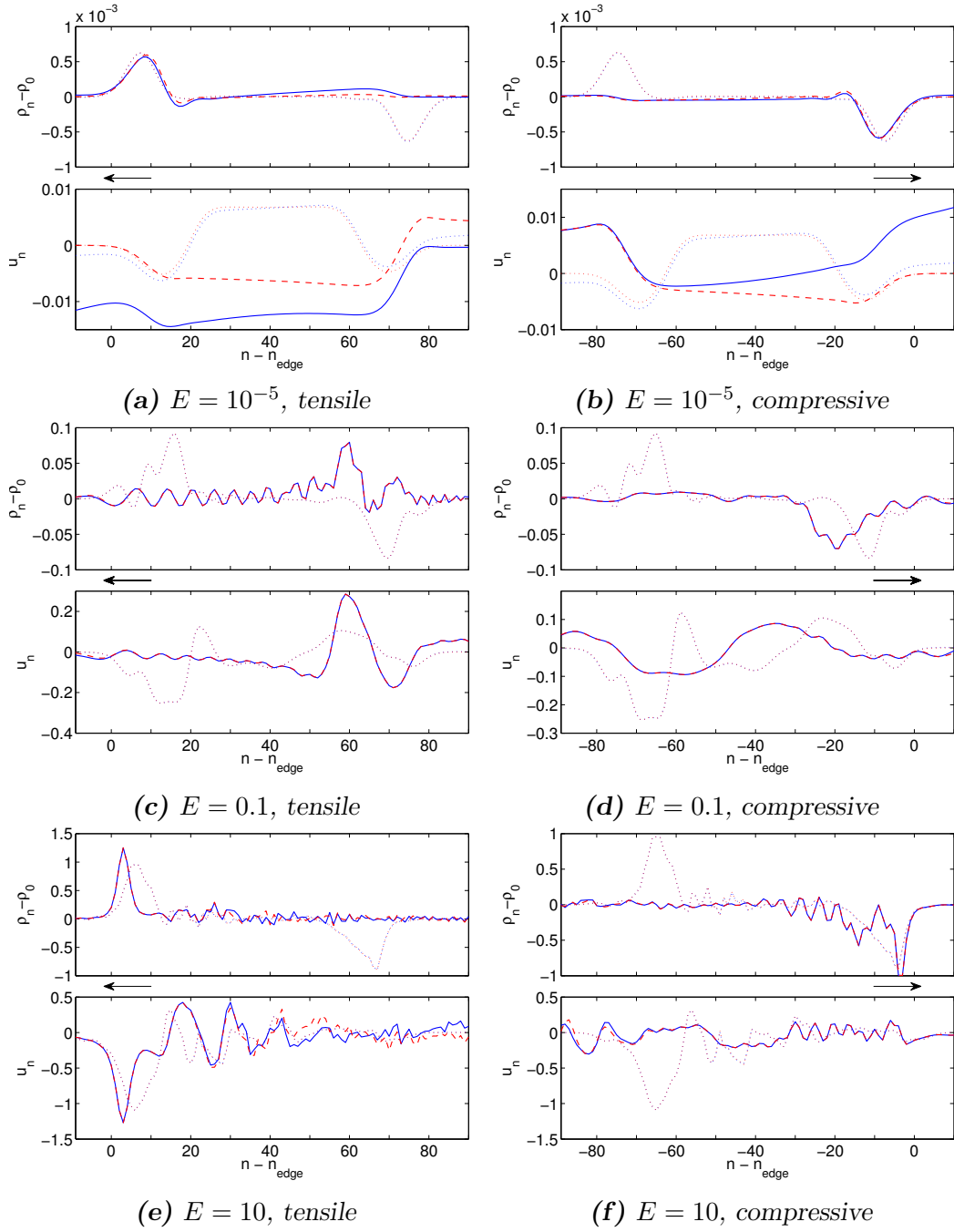


**Figure 4.6:** Pulse profiles corresponding to the times illustrated as dashed and solid line within the space-time maps of figure 4.5. The upper plot shows the pulse profile of  $\rho_n$  and the lower plot shows pulse profile of the central ion  $u_n$ . The black arrow marks the propagation direction. Periodic boundaries are used for the red lines and open boundaries for the blue lines.

amplitude pulse in the central ion displacement. The compressive pulse shows stronger fluctuation in  $\rho_n$ , but much less in  $u_n$  due to being effectively in the paraelectric phase. A steepening does also occur suggesting an amplitude dependent velocity.

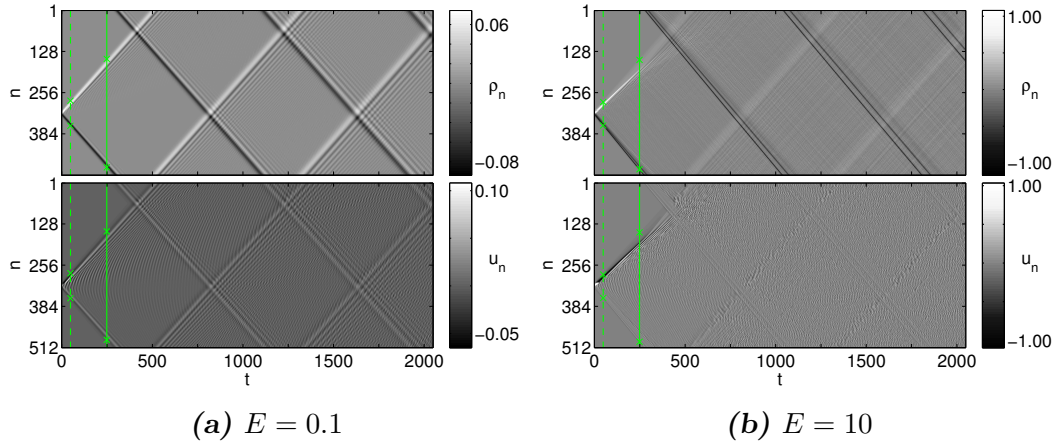
### 4.3.5 Paraelectric Phase

Figure 4.7 shows  $\rho_n$  and  $u_n$  for  $\xi = 1.05$ , which lies in the regime of only one minimum in the Double-Morse potential. The same two pulse energies  $E = 0.1$  and  $E = 10$  as for the ferroelectric phase are used. The low energy pulse shows some dispersion, whereby more for the tensile than for the compressive pulse. Also an optical mode is excited due to the gaussian excitation, which can be seen in the  $u_n$  plots in between the left and right propagating pulse. The excitation of an optical mode has been predicted by the equation (4.4). The high energy pulse has a tension sufficient to get over the phase transition, which exhibits a strong attenuation of the tensile pulse. The compressive pulse instead propagates regularly with a stronger dispersion as in the case of the low energy excitation.

The same is observed, when looking at the pulse profiles in figures 4.8. At low energies, the tensile part shows dispersion and additional fluctuations of the central ions behind the pulse in  $\rho_n$ . Energy transfers from the pulse to the central ions lead to an attenuation. The compressive pulse looks more regular with only a slight dispersion and attenuation. The reaction of the central ion seems to lag slightly behind the unit cell deformation. Getting to the high energy excitation, the tensile pulse has enough amplitude to get into the ferroelectric phase. The velocity is much slower and thus the pulse decays rapidly. The wide but low amplitude pulse in front of the oscillations confirms this idea. Due to reaching the ferroelectric phase, strong oscillations in  $u_n$  are excited suggesting an energy transfer to optical phonons. The compressive pulse exhibits self-steepening and dispersion with relatively small oscillations of the central ions.

In conclusion, the dispersion is stronger, when the pulse leads to a shift of the local  $\xi_n$  towards the phase transition, that means compression in the ferroelectric and tension in the paraelectric phase. An effective  $\xi_{eff}$  depending on the amplitude and the initially used  $\xi$  can be introduced. This  $\xi_{eff}$  corresponds to the sound velocity of the pulse, as can be seen in the following section or by going back to figure 3.7. Additionally, it lets one analyze the stability of the pulse. If  $v(\xi_{eff}) > v(\xi)$ , the peak propagates faster than the front and self-steepening occurs. The spectral weight shifts to higher wavenumbers, which have lower group and phase velocity due to the dispersion. Thus the dispersion counteracts the steepening. If  $v(\xi_{eff}) < v(\xi)$ , then the pulse widens and has a higher attenuation. Additional strong fluctuations get involved, if the excitation is strong enough to get from one phase to the other.

The idea of the effective  $\xi_{eff}$  will be checked in the following by studying the front velocity.



**Figure 4.7:** Space-time maps of  $\rho_n$  and  $u_n$  within the paraelectric phase  $\xi = 1.05$  and with two different pulse energies.

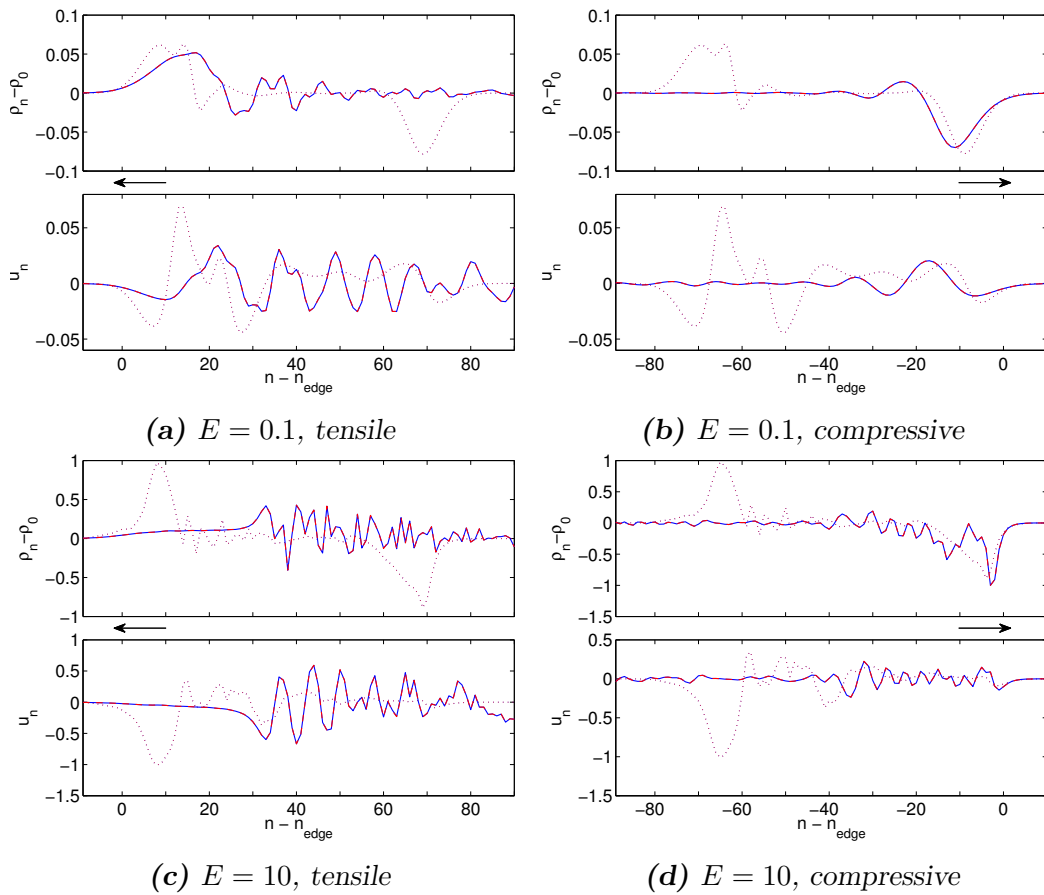


**Figure 4.8:** The pulse profiles belong to the space-time maps of 4.7. The black arrow marks the propagation direction. Periodic boundaries are used for the red lines and open boundaries for the blue lines.

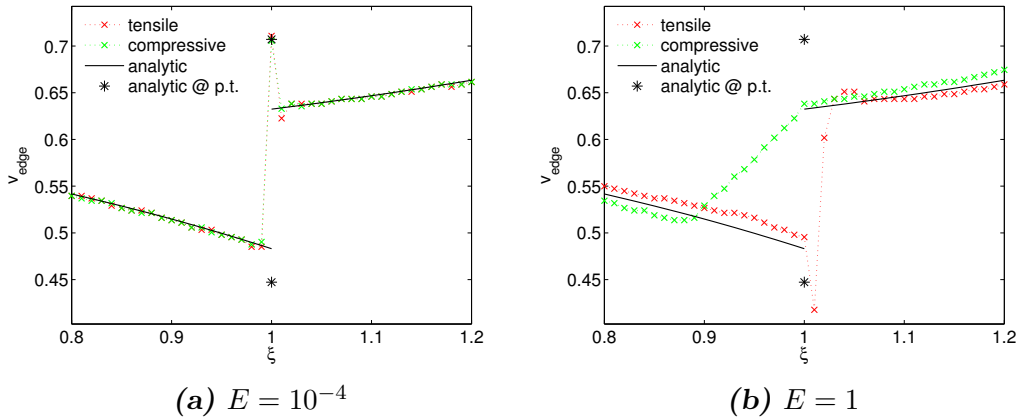


**Figure 4.9:** Both plots show the pulse front velocity obtained numerically in comparison to the analytically derived one. A low energy pulse has been excited for the left plot (a) confirming the analytical results. The velocity of a high energy pulse is plotted in (b) showing a symmetrical velocity splitting on the sides and an asymmetric splitting around the phase transition.

### 4.3.6 Pulse Front Velocity

The method of finding the edge or front of a pulse can be used to compute the sound velocity and its depends on  $\xi$ . If the edge at two times is known, then follows

$$v_s = \left| \frac{n_2 - n_1}{t_2 - t_1} \right|,$$

where  $n_1$  and  $n_2$  are the positions of the edge at the corresponding times  $t_1$  and  $t_2$ . The sound velocity has been derived in section 3.4.5 within the small wavenumber limit. But this limit leads to two twofold singularity, that the left and right limit differ each and from the value directly at the phase transition. The behavior of small but finite wavenumber might not be reflected properly. However, also in the case of the numerical study, difficulties and a strong influence of the used threshold exist for a  $\xi$  close to one. Known from the previous section, look for instance at figure 4.6c, two characteristic velocities exist, but only the faster front can be detected with confidence.

Only the periodic chain with 1024 unit cells is simulated for a time of 512. Both were increased by a factor of two to get a better accuracy. The same parameters  $K = 1$ ,  $k = 0.2$  and  $\mu = 2$  at two different energies are used. The threshold is set to be half of the peak compression and half of the peak tension. The sound velocities are presented in figure 4.9 together with the analytical results.

The low amplitude pulse in figure 4.9a confirms the analytical derived sound velocity. At the phase transition the numerical result depends on, whether the fast part or the slow part is detected. In the case of the low energy excitation, the faster part is detected confirming the analytical result of its velocity marked as a asterisk.

The right plot of 4.9 shows the pulse velocities of large amplitude pulses excited with an higher energy. Far from the phase transition exists a clear trend, that the tensile pulse exhibits a larger and the compressive pulse a lower velocity split symmetrically around the analytic solution. This splitting depends on the amplitude with a larger splitting observed for the high energy excitation, i.e. the large amplitude pulse. Compression and tension cause an effective shift of  $\xi$  towards larger values and smaller, respectively. Around the phase transition is a continuous transition from the lower velocity in the ferroelectric phase to the higher velocity in the paraelectric case observed for the compressive pulse. This transition already starts at  $\xi = 0.9$  implying that the amplitude of the compressive pulse is high enough to get in the paraelectric phase and sense the higher velocity. The tensile pulse has a dip at a  $\xi$  slightly above  $\xi = 1$  down to a velocity even lower than the analytic one for the softer subchain of the central ions.

This asymmetric velocity splitting of second kind around the transition can be observed qualitatively when going back to figures 4.6c and 4.6d on page 49. Compressive and tensile pulses propagate differently far. This can also be explained by effective  $\xi_{eff} := \frac{1}{\alpha} e^{-\frac{\rho_{eff}}{2}}$  introduced previously, where  $\rho_{eff}$  is either the maximal for a tensile or the minimal value for a compressive pulse.  $\xi_{eff}$  is either larger one for tension or smaller one for compression. The pulses feel therefore different sound velocities.

In summary, two kinds of velocity splitting occur. The first one exhibits a symmetrical shift for compressive and tensile pulse with respect to the low amplitude value. This shift crosses at the phase transition. In the ferroelectric phase propagates the compressive pulse slower than the tensile pulse and vice versa within the paraelectric phase. The velocity splitting of second kind occurs around the phase transition and is a nonlinear effect with a strongly asymmetric splitting.

### 4.3.7 Breather

Equation (4.4) suggests the possibility of exciting mostly optical modes. By choosing  $\epsilon_q = -\epsilon_Q$  with a pulse energy of  $E = 10^{-2}$  not large enough to get over the barrier and being in the regime of two degenerate ground states  $\xi = 0.95$ , a breather mode is excited. Breathers cannot be described within a small or a large amplitude approximations. They occur for instance in the Sine-Gordon equation [DP06]. The Sine-Gordon equation also exhibits kink and antikink solitons, which correspond to the class of topological solitons. If kink and antikink solitons have an attractive interaction, a bounded state, i.e. the breather mode, can exist. A decaying breather mode has been noticed by Zolotaryuk [ZPS91] using the same Double-Morse potential as in this thesis, when a kink and an antikink soliton with a certain velocity collide. It shows up as a local oscillation of the lighter subchain corresponding to the dynamics of the central ion. The heavy subchain deforms accordingly but not fast enough, so that the central ion remains in its initial potential well.

Note, that the breather mode shows a small shift with time. For the case

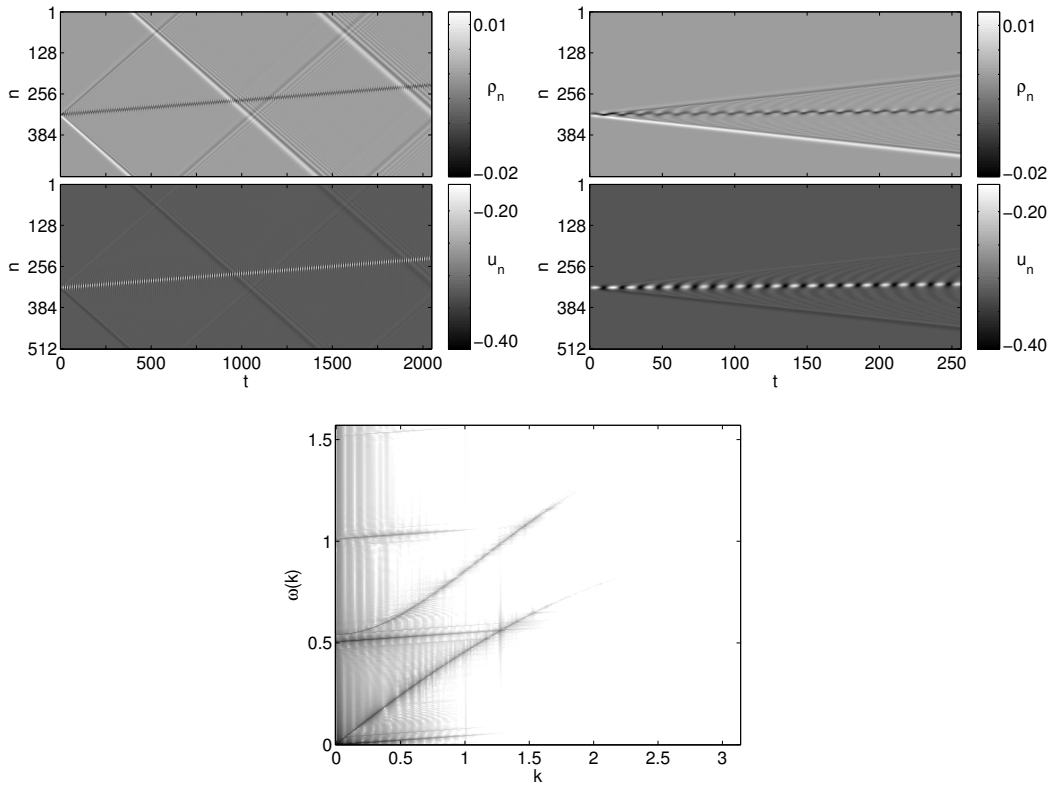


**Figure 4.10:** An complementary excitation of both subchain with  $E = 10^{-2}$  within the ferroelectric phase  $\xi = 0.95$  leads to a locally oscillating breather mode. The complete space-time map is shown in the upper left plot and a cut-off of the first quarter in time in the upper right plot. The lower plot contains the numerically obtained dispersion relation. The nearly horizontal line at  $\omega = 0.5$  and its second harmonic belong to the breather mode.

of two potential wells the initial condition, that all central ions sit in the left well already marks a symmetry break. A preferred direction of the breather can therefore exist. The picture can be mirrored by choosing the other well as initial condition for the central ion and mirroring the initial velocity distribution. The breather mode appears as a nearly horizontal line at  $\omega \approx 0.5$  and its second harmonic at  $\omega \approx 1$  in the dispersion relation. The steepness determines the group velocity and thus the propagating velocity of the breather. The numerical method of gaining the dispersion relation will be introduced in the next section, but shall be used here without further explanations.

### 4.3.8 Comparison of Periodic and Open Boundaries

All pulse profile plots do not reveal any significant difference between both boundary condition. However, there are some small differences in the initially prepared ground state right at the phase transition as seen for example in figure 4.6a and b. But the pulses and their propagation are similar. Differences will arise for sure, when the pulse arrives at one of the ends. The pulse swaps at an

open end from being compressive to tensile or vice versa, whereas such a swap does not occur for a periodic chain. Thus, the long time behavior is different. In conclusion one can say, that both behave the same as long as the pulse does not reach one of the ends.

## 4.4 Numerical Dispersion Relation

The dispersion relation for the Double-Morse chain has been derived for small amplitude vibrations in section 3.4 in a completely analytical way based on the Hamiltonian calculus. This section deals with the numerical determination of the dispersion relation and shall confirm the main results gained by the analytical calculation. The main feature is the softening of the optical mode by applying an external pressure or changing  $\alpha$ . Both have been merged to the general parameter  $\xi$ .

The velocity splitting noticed in the prior section lets one expect, that the eigenfrequency of a vibration mode depends on its amplitude. This leads together with the random distribution of amplitudes in the chain to a wider spectral distribution of the excited frequencies compared to the sharp eigenmodes obtained in the linear theory.

The procedure is as follows. The chain is set in the ground state explained in section 4.2. A chain with 512 unit cells is used. Then random noise with a gaussian distribution is added to the velocities. The velocity distribution is scaled to give a desired energy density. A simulation for  $t = 1024$  time steps is carried out and the temporal evolution is recorded in a space-time map. A Fourier transform in space and time gives a map of Fourier coefficients depending on frequencies  $\omega$  and wavenumbers  $k$  as exemplary shown in figure 4.11a using an energy density of  $\frac{E}{N} = 10^{-5}$ . Doing this 32 times and taking the average of the same Fourier coefficient from different runs, yields a smooth dispersion relation and decreases the noise. The Fourier coefficients are plotted logarithmically for a better visualization. Black corresponds to the maximal value of the whole Fourier map and white belongs to a ten orders of magnitude smaller value. The same can be done for the dynamic variable  $u_n$  and  $\rho_n$ , which leads to the figures 4.11b in the second column and 4.11c the third column. Three different  $\xi = \{0.95, 1, 1.05\}$  corresponding to the ferroelectric phase, the phase transition and the paraelectric phase are used. They have the same order starting from the top row.

The ferroelectric phase is shown in the upper row. Both branches can be seen in the Fourier map suggesting, that the unit cell deformation and the central ion motion are strongly correlated. Indeed, a change of  $\rho_n$  always leads to a different equilibrium position  $u_0(\rho_n)$  of the central ion according to what has been seen for a propagating pulse in section 4.3.3.

Both branches behave like acoustic modes at the phase transition. The central ion Fourier map has a strong spectral weight at the small wavenumbers, which could be due to the existence of domains and could be a hint of a central peak. Only a slight tension is sufficient to induce domains, which are spread over several unit cells and thus contribute to the small frequency and

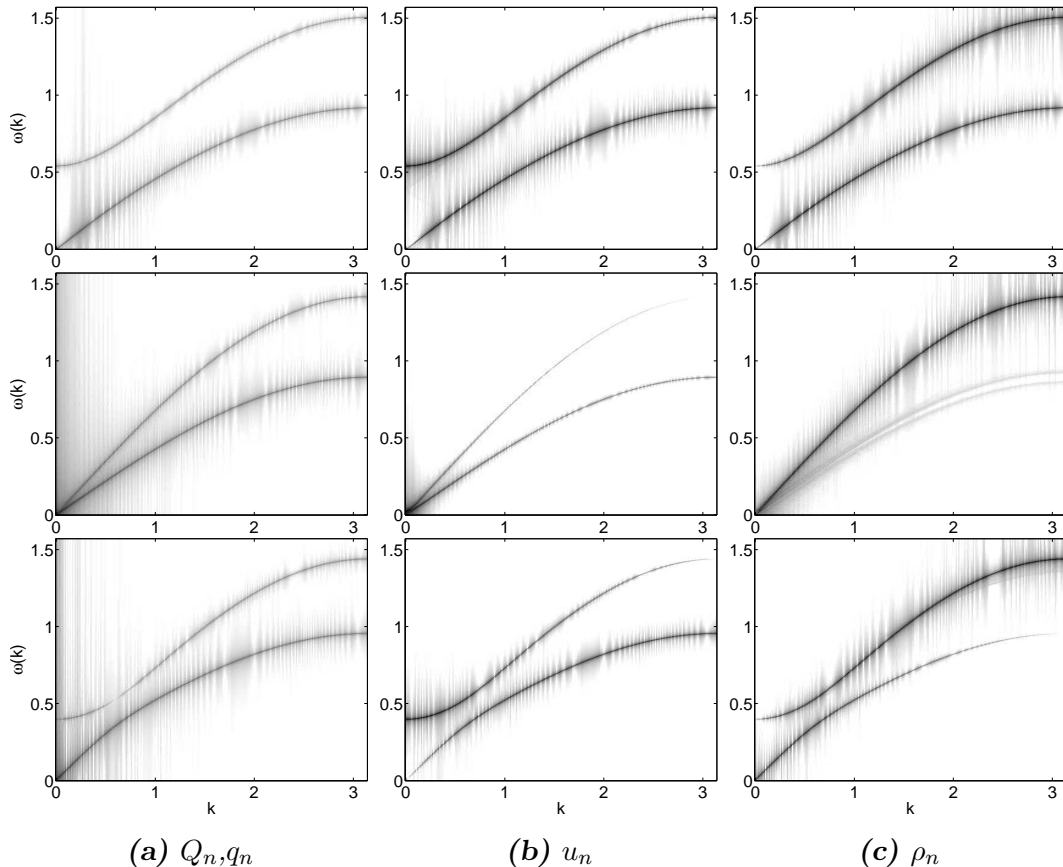


**Figure 4.11:** Dispersion relations for the complete displacement map (a), for  $u_n$  (b) and for  $\rho_n$  (c).  $u_n$  reflects the optical mode and  $\rho_n$  the acoustic phonon mode.  $E = 10^{-5}$  and from top row to bottom row  $\xi = \{0.95, 1.0, 1.05\}$ . The grayscale in (a) ranges over ten orders of magnitude, whereas in (b) and (c) over six orders.

wavenumber spectrum. Schneider and Stoll [SS78] argue, that moving domains and domain walls give rise to a central peak in the frequency spectrum at a wavenumber of zero. However, a more detailed view on the spectra would be necessary to conclude, that the same phenomenon occurs in this model. Nevertheless the central peak was observed in several perovskites by neutron scattering methods in the 1970s [SASR72, KSMS73]. It appears as a narrow peak around  $\omega = 0$ , i.e. the elastic scattering, and was first attributed to the elastic scattering on impurities, which turned out to not be the whole picture and the dynamics of domains as stated above has to be taken into account.

The last plot containing the Fourier map of the unit cell deformation indicates, that the upper branch belongs to the unit cell deformation and thus to the more rigid Q-subchain.

The last row, the paraelectric phase, reveals an avoided crossing. The oscillations of the central ions with respect to the unit cell  $u_n$  belong to the optical mode, which goes from an approximate frequency of 0.4 via the crossing to around 0.95. This is shown by a darker line corresponding to higher Fourier coefficients. For  $\rho_n$  its acoustic behavior can be seen, as the darker line in-

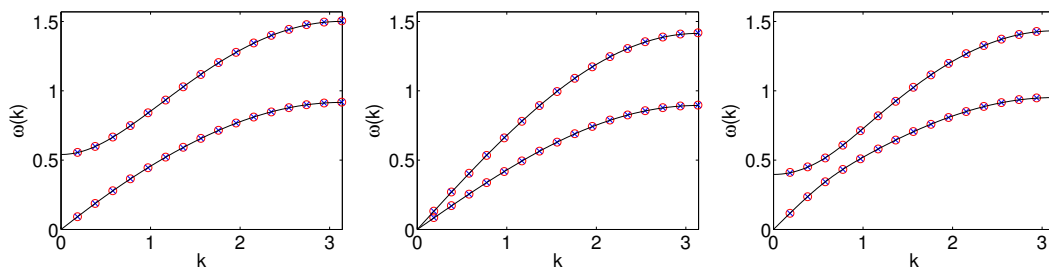


**Figure 4.12:** The plots give a comparison of the analytical dispersion relation (solid black line) with the numerical results obtained in an 512 unit cell chain with either periodic boundaries (red circles) or open boundaries (blue crosses) at three different  $\xi$  (f.l.t.r.):  $\xi = 0.95$ ,  $\xi = 1.00$  and  $\xi = 1.05$ .

creases linearly towards the crossing. After the crossing it belongs to the upper branch reaching a frequency slightly below 1.5.

Going back to figure 4.11a and determining the two maxima in the frequency distribution for some wavenumbers  $k$ , gives the opportunity to compare analytical and numerical dispersion relation. The standard Matlab function `findpeaks()` serves well for getting the frequencies belonging to these maxima. A comparison of analytical, open boundaries and periodic boundaries can be seen in figure 4.12. The red circles belong to the numerical dispersion relation gained for the periodic chain. Blue crosses are used for the free chain and the analytical result is plotted as a solid black line. Both, the numerical results for periodic and free chain as well as numerical and analytical results agree nicely and confirm the analytical calculation with its small amplitude approximation.

An interesting question to ask is, how the dispersion relation changes reaching the nonlinear regime. Figure 4.13 gives an overview. Five  $\xi$  including the three previously chosen are used:  $\xi = 0.90$ ,  $0.95$ ,  $1.0$ ,  $1.05$  and  $1.1$  ordered from top to bottom. Each  $\xi$  is simulated at three different energy densities beginning from left:  $\frac{E}{N} = 10^{-5}$ ,  $10^{-3}$  and  $0.1$ . The dashed green lines correspond to the analytic solution.

The left column confirms again the linear limit, as analytical and numerical dispersion relation agree. The dispersion relation starts to smear out, when going to the intermediate energy density. This effect is most pronounced at the phase transition, the middle row, and decreases with increasing distance from the phase transition. Both modes start to form one joint mode for small wavenumbers directly at the phase transition. It expands to larger wavenumbers and even to a wider range of  $\xi$  in the high energy case shown in the right column. This mode lies between both small amplitude modes and splits into two strongly blurred modes. A strongly blurred optical mode for small wavenumbers can also be noticed and is shifted to lower frequencies for  $\xi = 1.1$  and to higher frequencies for  $\xi \leq 1.0$ .

The joint acoustic mode suggests a collective but chaotic phonon mode. The nonlinearity leads to scattering events of the phonons, but as they cannot

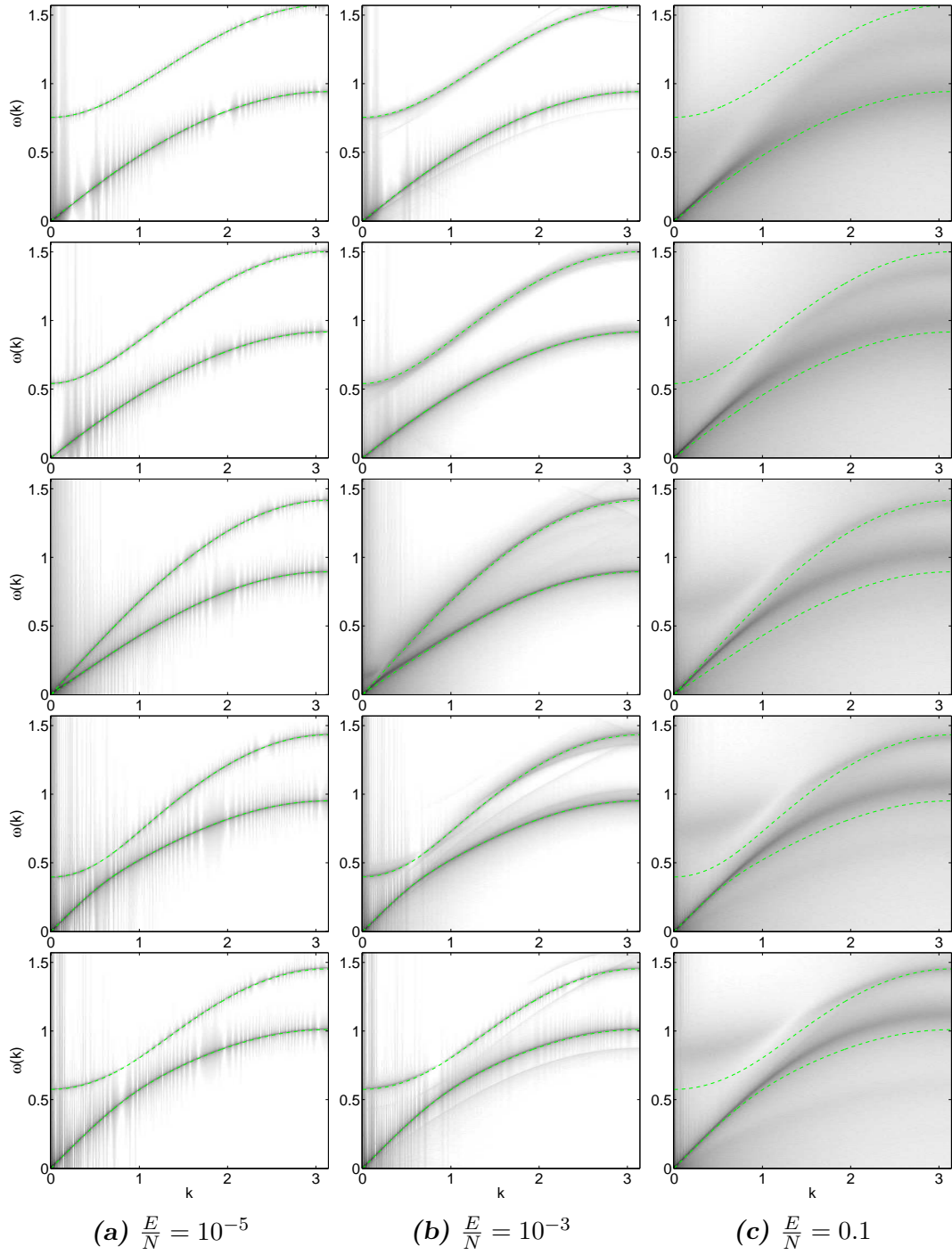


**Figure 4.13:** Dispersion relation at five  $\xi$ :  $\xi = 0.90, 0.95, 1.0, 1.05$  and  $1.1$  ordered from top to bottom and at three different energy densities beginning from left:  $\frac{E}{N} = 10^{-5}, 10^{-3}$  and  $0.1$ . The dotted blue line corresponds to the analytic solution. Shown are the logarithms of the Fourier coefficients obtained by a discrete Fourier transform in time and space of the displacements. The gray code ranges over ten orders of magnitude with black being the highest value.

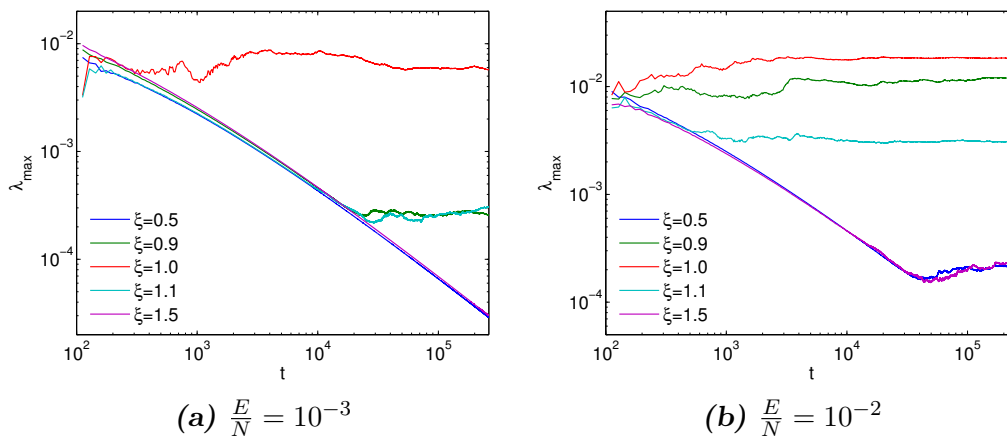


**Figure 4.14:** The temporal evolution of the maximum Lyapunov Exponents five different  $\xi = \{0.5, 0.9, 1.0, 1.1, 1.5\}$  and at two different energy densities  $\frac{E}{N} = 10^{-3}$  (a) and  $\frac{E}{N} = 10^{-2}$  (b).

transfer energy to impurities or even to the lattice via an umklapp process, the momentum and energy is conserved. This would be the regime of Second Sound, whose existence in perovskites such as  $\text{SrTiO}_3$  is controversial [SCL00, KTS07].

The widening of the spectral lines and the existence of excited states far from the dispersion relation, which has been obtained in the linear theory, imply fluctuations and chaotic dynamics, which will be studied systematically in the next section.

## 4.5 Lyapunov-Exponent Analysis

The main concern of this section is the characterization of the chaotic behavior of the chain based on the maximal Lyapunov Exponent, in the following abbreviated as mLE. The mLE is a measure of how fast a perturbation grows with respect to original phase space trajectory. The theory on this is described in section 2.4. As the system has to evolve for long times, only a short chain of 16 unit cells is simulated. Periodic boundaries are used, thus no contraction of the whole chain occurs and  $\xi = \frac{1}{\alpha}$  holds as shown in section 3.3.2.

The initial conditions are similar to what has been used for determining the dispersion relation numerically. The displacements are again in a ground state and random noise is added to the initial velocities, which are normalized to the desired total energy. This gives a energy density homogeneously distributed over the whole chain. The deviation vector characterizing a perturbation is also randomly chosen, but normalized to unity.

Figure 4.14 shows the temporal evolution of the mLE for different  $\xi$  and at two different initial energies. If the dynamics are chaotic, then the mLE saturates to a finite value. In the case of regular dynamics, the mLE decreases linearly in the log-log plot and thus corresponds to a power-behavior. It can be seen, that there is a lower bound for the smallest achievable mLE depending

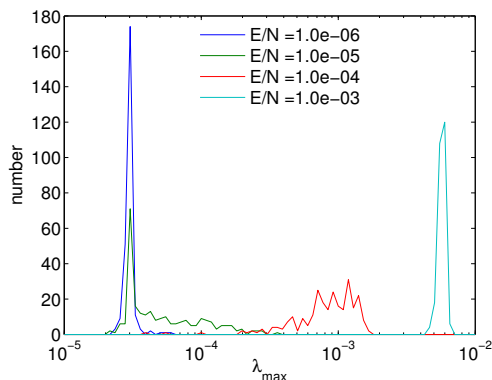


**Figure 4.15:** The histogram shows the distribution of the maximum Lyapunov Exponents at different energy densities. The used parameters are:  $\xi = 1$ ,  $\bar{K} = 1$ ,  $\bar{k} = 0.2$  and  $\mu = 2$ . The lowest achieved mLE is determined by the total time, the simulation runs. That is why a sharp distribution at  $2 \cdot 10^{-5}$  occurs for lowest energy.

on the total time the simulation runs. At both energy densities the mLE takes its maximal value at or slightly above the phase transition, in particular at  $\xi = 0.9$  and  $1$  for the higher energy density of  $E = 10^{-2}$  and at  $\xi = 1$  for the lower energy density of  $E = 10^{-3}$ . Less chaotic or even regular behavior shows up for both far from the phase transition  $\xi = 0.5$  and  $1.5$ .

As the initial conditions are random, the mLE fluctuates and it is favorable to get some statistics. In order to achieve that, the simulations were done 256 times for the same  $\xi$  and total energy. This leads to a distribution shown in the histogram in figure 4.15 for different energies directly at the phase transition  $\xi = 1$ . The lowest energy density has a sharp distribution of the mLEs around the lowest achieved mLE determined by the total simulated time. Regular dynamics are observed. Whereas at the highest energy density the largest mLEs of around  $4 \cdot 10^{-2}$  appear, which are sharply distributed again. For the intermediate energy densities, the mLE distribution is wider. But it is obvious, that the mLE increases with the initial energy density due to stronger nonlinear coupling. One could also argue, that more phonon scattering events per time occur.

For determining whether chaotic dynamics occur or not, a threshold mLE of  $\lambda_t := 10^{-4}$  is chosen and the probability of chaos can be introduced as:

$$p_{chaos} := \frac{1}{N} \sum_{n=1}^N \Theta(\lambda_n - \lambda_t), \quad (4.6)$$

where  $N$  is the total number of trials and  $\Theta(x)$  is the Heaviside function, which is either zero, if the argument is negative or one, if the argument is positive. Thus, the definition (4.6) counts the number of trials with a mLE larger than the threshold divided by the number of trials. This was done for several energy densities at five different  $\xi$  and is plotted in figure 4.16.

One can clearly see, that for each  $\xi$  a transition exists. The lowest energy density that is necessary for chaotic dynamics grows with getting away from

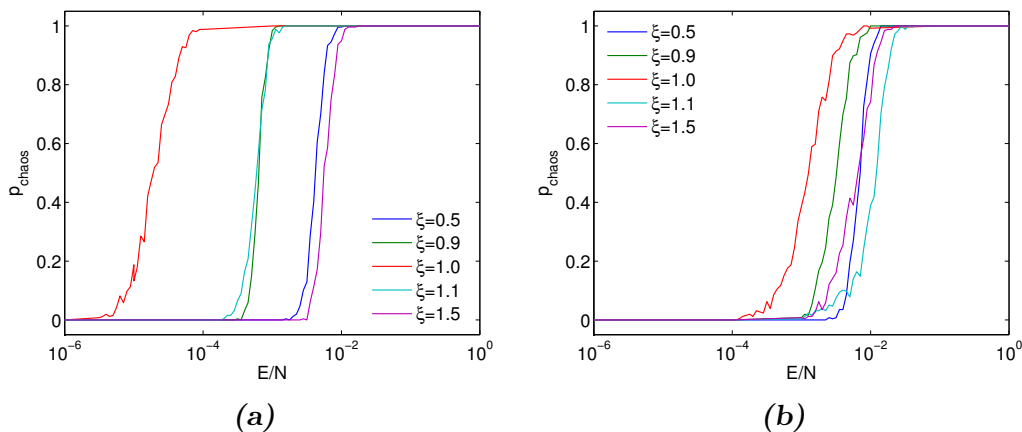


**Figure 4.16:** Plot of the chaos probability based on 4.6 depending on the initial energy density. For each  $\xi$  exists an energy threshold between regular and chaotic dynamics. This threshold is smallest directly at the phase transition point  $\xi = 1$ . A chain with  $\bar{K} = 1$ ,  $\bar{k} = 0.2$  and  $\mu = 2$  is used for the left plot and  $\bar{K} = 10$ ,  $\bar{k} = 2$  and  $\mu = 2$  for the right one. The threshold shifts to higher energy density, when the influence of the Double-Morse potential is lowered by using higher  $\bar{K}$  and  $\bar{k}$ .

the phase transition. The transition is slightly sharper in the ferroelectric phase, which might be due to the potential barrier between the two wells.

Again a second chain with one order of magnitude lower weighting on the Double-Morse potential is used. It shows in comparison a shift of the chaos probability threshold towards higher energies. Henceforth, the thresholds move closer together.

We have seen, that the dynamics are more chaotic around the phase transition. This is caused by a larger influence of the nonlinearity of the Double-Morse potential. Imagine now a far-from-equilibrium state. Due to the stronger nonlinearity and hence a interaction of vibration modes, this state would relax faster towards a thermal equilibrium and an energy density distributed homogeneously over the whole chain. We will check this behavior in upcoming section.

## 4.6 Mode Interaction

The excitation is done by choosing an appropriate initial condition. The desired wavenumber  $k$  and the total energy of that excitation can be achieved by using a certain periodicity and amplitude. Due to the nonlinear nearest neighbor interaction, there is no analytic way to find an initial condition of the displacements with a sine periodicity based on the wavenumber and energy. Therefore it is favorable to choose an initial spatial momentum distribution. However, this already excites higher harmonics in the Fourier transform of the spatial displacement distribution, that is in the  $k$ -spectrum, due to the nonlinear interaction potential.

All oscillators are initially set in the ground state introduced in section 4.2. Only the periodic chain is used. For controlling the initial energy per mode, a mode is excited by adding a spatial momentum distribution with the corresponding periodicity. Therefore the initial velocities reads as

$$\begin{aligned}\dot{q}_n &= \epsilon_q \sin \left( a \frac{\pi}{N} n + \phi_q^{(0)} \right) \\ \dot{Q}_n &= \epsilon_Q \sin \left( b \frac{\pi}{N} n + \phi_Q^{(0)} \right).\end{aligned}$$

The amplitudes are given by  $\epsilon_q$  and  $\epsilon_Q$ , respectively.  $a$  and  $b$  have to be integers and stand for the periodicity determined by the wavenumber by  $k_q = \frac{a\pi}{N}$  and  $k_Q = \frac{b\pi}{N}$ . For generality, also the phases  $\phi_q^{(0)}$  and  $\phi_Q^{(0)}$  are denoted, but these are set to zero in all simulations.

As already mentioned, the amplitude is related to the total energy. The energy deposited in one subchain is given by equation (4.7).

$$E_Q = \sum_{n=1}^N \frac{\mu \dot{Q}_n^2}{2} = \frac{\mu}{2} \sum_{n=1}^N \epsilon_Q^2 \sin^2 \left( b \frac{2\pi}{N} n \right) \quad (4.7)$$

For simplicity and without loss of generality the phase  $\phi_Q$  is assumed to be zero. A continuous approximation in the limit of  $N \rightarrow \infty$  transforms the sum in (4.7) into an integral (4.8) over  $x = \frac{\pi n}{N}$  on the interval  $(0, \pi]$ .

$$E_Q \approx \frac{\mu \epsilon_Q^2}{2} \int_0^\pi \sin^2(x) dx \quad (4.8)$$

It can be transposed to get the amplitude-energy relation (4.9) used for the initial condition.

$$\epsilon_Q = \sqrt{\frac{4E_Q}{\mu}} \quad (4.9)$$

The same derivation can be done for the amplitude in the q-subchain:

$$\epsilon_q = \sqrt{4E_q}. \quad (4.10)$$

### 4.6.1 Thermalisation

The initial condition introduced previously represents a state far from equilibrium. The system may tend towards an equilibrium, but depending on the coupling between modes, this occurs on different time scales. Figure qualitatively 4.17 shows the time-evolution for the k-spectrum for exemplary chosen parameters. Their exact values shall not be of interest here. The initially excited modes are  $k_1 \approx 0.4$  and  $k_2 \approx 0.6$ . Modes with  $k = mk_1 + nk_2$ ,  $m, n \in \mathbb{Z}$  are already excited, partly due to the initial condition together with the non-linear potential as stated in the previous section and partly due to mode coupling. They form a discrete spectrum that vanishes later. A quasi-continuous spectrum grows on the long timescale. Note, that the spectrum is still discrete

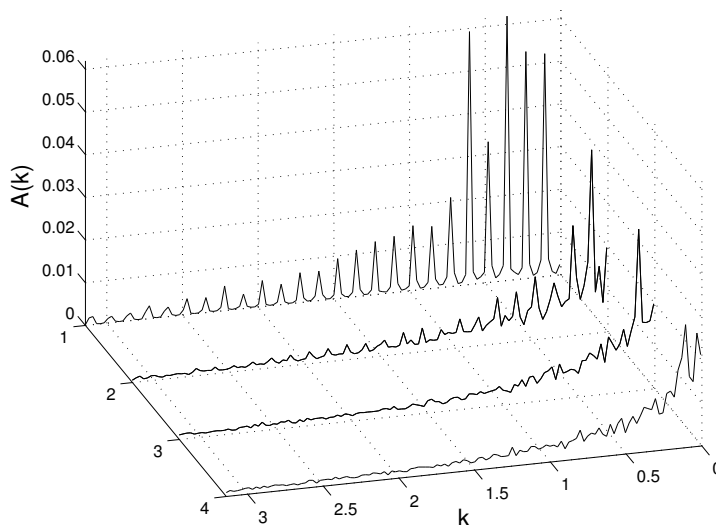


**Figure 4.17:** An over four consecutive time intervals averaged  $k$ -spectrum for arbitrarily chosen parameters is shown.  $k_1 \approx 0.4$  and  $k_2 \approx 0.6$  are initially excited. Shortly after excitation these both modes couple and modes with  $k = mk_1 + nk_2$ ,  $m, n \in \mathbb{Z}$  grow and forming a discrete spectrum. This discrete spectrum vanishes at later times and a quasi-continuous spectrum evolves.

due to the finite length of the chain, but in contrast to the discrete spectrum due to interaction between two excited modes, the grid is much smaller.

It is an interesting question to ask, whether a Boltzmann distribution evolves exhibiting an effective temperature and if a measure of the distance of a state from the equilibrium could be found. This would involve a thermodynamic point of view like for the Aubry model in section 2.3, but goes beyond the scope of this thesis.

## 4.6.2 Entropy of the Wavenumber Spectrum

In order to characterize the evolution of the  $k$ -spectrum, one may use the entropy, also used within the frame of computer sciences and in that context known as Shannon entropy. The entropy of the wavenumber spectrum can be defined as

$$S = -\frac{1}{\ln(N)} \sum_k A_k \ln(A_k). \quad (4.11)$$

The sum is carried out over all wavenumbers within the Brillouin zone and the  $A_k$  are the Fourier coefficients of a discrete Fourier transform with respect to the displacements. The  $A_k$  itself are normalized by  $A_k = \frac{\hat{A}_k}{\sum_k \hat{A}_k}$ , so that the sum over all  $A_k$  is unity.  $N$  shall be the number of discrete modes due to the finite length of the chain. Thus the prefactor  $\frac{1}{\ln(N)}$  normalizes the entropy to the interval  $[0, 1]$ . The maximal value of one will be reached, if all  $A_k$  are

uniformly distributed, that is  $A_k = \frac{1}{N}$ . The entropy is zero in the case where only one mode is excited and all other modes are zero.

By exciting a low entropy state, e.g. two modes, and looking at the time evolution of the entropy, it is possible to obtain a measure of how strong different modes interact. This is done for different  $\xi$  and energy densities illustrated in figures 4.18 as a map of entropy. The parameters of the chain are the same as in the previous sections:  $\bar{K} = 1$ ,  $\bar{k} = 0.2$  and  $\mu = 2$ . The map of entropy is obtained by spatial Fourier transform of the space-time map computed by the numerical integration of the equations of motion. The obtained k-time-map is split into four consecutive time intervals and for each time interval the k-spectrum is averaged. The entropy (4.11) can now be calculated and is plotted against the energy density on the y-axis and the general phase-transition tuning parameter  $\xi$  on the x-axis. As shown in section 3.3.2,  $\xi = \frac{1}{\alpha}e^{-\rho_0}$  holds. By using the periodic boundary condition, this reduces to  $\xi = \frac{1}{\alpha}$ . The energy density is given by the initial condition and does not change during the numerical integration due to using a symplectic Nyström method. The blue regions in figure 4.18 depict low entropy, meaning regular behavior and low coupling, whereas the red regions correspond to high entropy. These choices of  $\xi$  and energy density lead to a strong coupling and fast thermalisation. Especially for  $\xi$  very close to 1 the coupling exists even for lowest energies. Note that the energy is plotted in  $\log_{10}$ -scale. For  $\xi$  far from the phase transition the energy threshold between regular and chaotic regime shifts towards higher energies. At least for the case of two minima ( $\xi < 1$ ) this shift can be explained by the growing barrier height

$$E_B = (1 - \xi)^2. \quad (4.12)$$

At later times this energy threshold moves slightly towards smaller energies suggesting, that there is a timescale of thermalisation involved. This means, that one only has to wait long enough for the thermalisation to happen.

When shifting the weighting of the interaction terms towards the next-nearest neighbor interactions, i.e. when the Double-Morse potential has lower influence on the dynamics, the threshold shifts towards higher energy densities as well. It is shown in figure 4.19 for the parameters  $\bar{K} = 10$ ,  $\bar{k} = 2$  and  $\mu = 2$ . The steepness of the threshold between regular and chaotic behavior is slightly lower. That means, the shift is more pronounced around the phase transition, than at some distance from it.

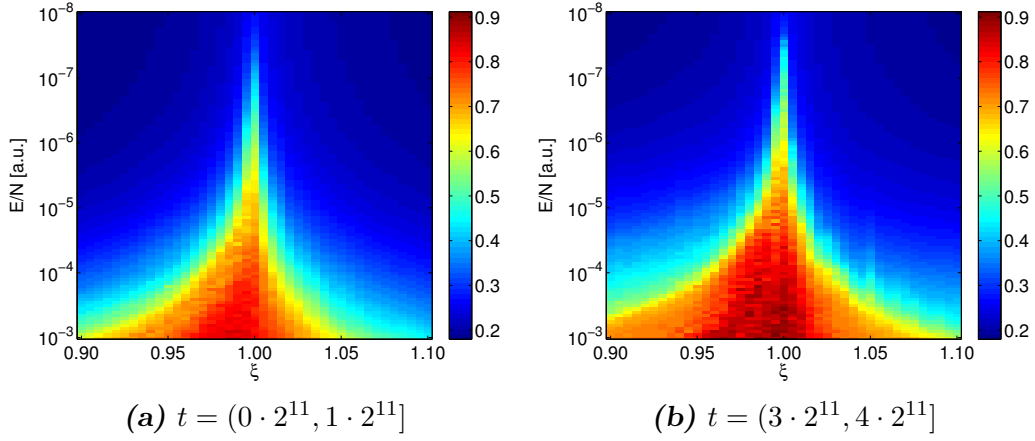


**Figure 4.18:** Entropy map for the chain with  $\bar{K} = 1$ ,  $\bar{k} = 0.2$  and  $\mu = 2$ . The total integration time is divided into four equal sections. The  $k$ -spectrum, the spatial Fourier transform of the displacements, is averaged over one section and its entropy calculated. (a) belongs to the first time interval, whereas (b) belongs to the last one.

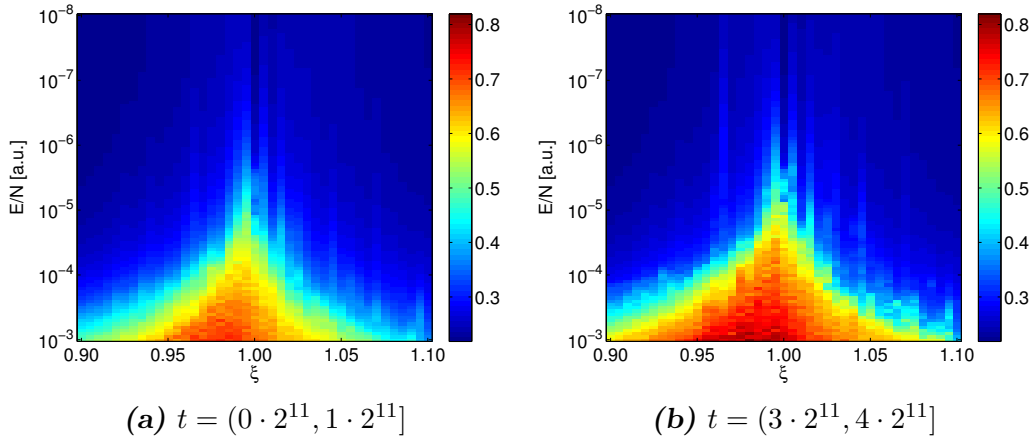


**Figure 4.19:** Entropy map for the chain with  $\bar{K} = 10$ ,  $\bar{k} = 2$  and  $\mu = 2$ . (a) belongs to the first quarter, whereas (b) to the last quarter.

# Chapter 5

## Summary and Outlook

### Summary

In summary, the present model reveals a lot features of ferroelectric materials and suggests further possible phenomena. In the linear theory, the model performs a continuous phase transition from a paradiortive phase at high temperatures to a ferrodistorive phase at low temperatures. These correspond to paraelectric and ferroelectric phases, if one assigns opposite charges to the two components of the chain. The softening of an optical phonon mode, as a characteristic feature of a structural phase transition, is reproduced. Additionally, the experimentally detectable sound velocity in the long wavelength limit has been calculated and reveals a twofold discontinuity. The left and right limit differ and directly at the transition two velocities exist. Here, the central ion motion is only weakly coupled to the unit cell background.

The numerical simulations confirm the linear theory, but also enable studying nonlinear effects. It has been shown, that the nonlinearity caused by the two back-to-back Morse potentials strongly influences the dynamics around the phase transition. Looking at the qualitative behavior of the pulse, either a strong attenuation due to an amplitude dependent dispersion or even a steepening and growing of the pulse has been observed. In fact, the ingredients for Korteweg-de Vries solitons, nonlinearities leading to the steepening and the counteracting dispersion, are available. They would add to the topological solitons corresponding to domain walls, which has been studied a lot in the literature. The velocity and attenuation of compressive and tensile pulses differ. In contrast to what has been observed considering a linear chain with up to third order nearest neighbor interactions [BHS<sup>+</sup>12] the velocity changes for compressive and tensile strain are not equal in magnitude. The pulse velocities obtained numerically show that two nonlinear regimes exist. One exhibiting a strongly asymmetric velocity splitting around the phase transition. Additionally, this regime increases with a larger amplitude. The second regime appears sufficiently far from the phase transition and shows a symmetrical velocity splitting. However, this is cannot be assigned one to one to the pulse attenuation. Here, the steepness of the sound velocity depending on general phase transition parameter  $\xi$  is crucial. A compressive (tensile) pulse feels an effective increase (decrease) of  $\xi$  and does influence the actual sound velocity. For

---

instance, a compressive pulse within the paraelectric phase propagates faster, when it has a larger amplitude and gives rise to a self-steepening. On the other side, the tensile pulse will decay. Within the first regime, the effective  $\xi$  changes from one phase to the other phase leading to the mentioned strong nonlinearity.

The nonlinearity also emerges in the simulated dispersion relation. At higher energy densities the two distinct branches merge to one very pronounced acoustic branch with a wide spreading and a less pronounced optical phonon mode appears. This starts for long wavelengths around the phase transition, but extends to shorter wavelengths and a wider regime around the transition. The dispersion relation of the central ion exhibits even at low energies, when the branches match with the linear theory, a strong spectral weight on the long wavelengths, which is caused by moving domains and domain walls and suggesting a central peak.

At high energy densities, the dispersion relation spreads due to the dependence of the vibration frequency on the amplitude. This spreading is most pronounced around the transition and suggests a strong nonlinearity and chaotic dynamics. A study of the Lyapunov exponent confirms this strong interacting regime. With increasing the energy density a clear transition to chaos is observed. This energy threshold is significantly lower at the transition and increases with getting away from transition point.

Within the picture of a phonon perturbation theory, one says, that the nonlinearity leads to interaction of phonons. An entropy of the Fourier spectrum of the displacements has been introduced and temporal evolution starting with an low entropy state was analyzed. The conclusion is, that these interactions are strong around the phase transition even for lowest energies. This would show up in an experimental measurement as a strong attenuation of the modes excited initially. Thus the model explains attenuation within a limited spectrum even though the model is conservative and without dissipation. That means the experimentally observed attenuation has to be divided in either being caused by nonlinearity or by dissipation.

## Outlook

As always with such models the work can be extended in various directions. One, to my view most interesting, would be to include an external (electric) field, which tilts the Double-Morse potential. This could give further insights into the behavior of domains and the dynamics of domain walls. A similar extension was already done on the Aubry model [PF87] and could be applied to the present model.

The thesis on hand has focused on the dynamical features. A thermodynamic view, as summarized for the Aubry chain, is lacking. Question in this context, which one might ask are: Does the far of equilibrium chain approach a thermodynamic equilibrium consistent with the Boltzmann distribution? What would be the temperature? According to the thermodynamic view on the Aubry model, one should also think about the influence of noise and how it correlates to the temperature. To stretch this thought, does the noise

---

influence, in which thermodynamic regime the chain currently is?

It would also be interesting to find realistic parameters, which could resemble experimental behavior of for instance lead titanate. Nonlinear effects of sound propagation as the self-steepening and the sound velocity splitting have already been observed. Do they agree with the same features occurring in the model? Realistic parameters have to be found to be able to answer this question.

Leaving the thermodynamic view and getting back to the dynamics, the long time pulse propagation including the temporal evolution of the spectrum would be of interest. Especially whether the model could also explain the nonlinear phonon propagation observed in SrTiO<sub>3</sub> [BHS<sup>+</sup>12].

When remembering the observations, some applications come into mind. It has been shown, that external pressure will influence how “deep” the chain is in one of the phases. Assuming the chain is in the ferroelectric phase, applying external pressure or initiating a strong pulse could decrease the electrical field necessary to swap the polarization. This would be a pulse or pressure assisted polarization switching. Secondly, the asymmetric pulse propagation suggests the possibility of an acoustic rectifier. Imagine a monodomain substrate and a pulse propagating parallel or antiparallel to the polarization. They would feel a different attenuation. However, the strength of this effect for realistic parameters remains to be investigated.

# Bibliography

- [Aub75] S. Aubry. A unified approach to the interpretation of displacive and orderdisorder systems. I. Thermodynamical aspect. *The Journal of Chemical Physics*, 62(8):3217, 1975.
- [Aub76] S. Aubry. A unified approach to the interpretation of displacive and orderdisorder systems. II. Displacive systems. *The Journal of Chemical Physics*, 64(8):3392, 1976.
- [B82] H. Böttger. *Principle of the Theory of Lattice Dynamics*. Akademie-Verlag Berlin, first edition, 1982.
- [Bak54] A. N. Baker. A Quantum Mechanical Treatment of the Symmetrical Hydrogen Bridge. *The Journal of Chemical Physics*, 22(9):1625, 1954.
- [BH54] M. Born and K. Huang. *Dynamical Theory of Crystal Lattices*. Clarendon Press, first edition, 1954.
- [BHS<sup>+</sup>12] A. Bojahn, M. Herzog, D. Schick, I. Vrejoiu, and M. Bargheer. Calibrated real-time detection of nonlinearly propagating strain waves. *Physical Review B*, 86(14):144306, 2012.
- [BS73] G. Burns and B. A. Scott. Lattice Modes in Ferroelectric Perovskites: PbTiO<sub>3</sub>. *Physical Review B*, 7(1):3088, 1973.
- [Coc59] W. Cochran. Crystal stability and the theory of ferroelectricity. *Phys. Rev. Lett.*, 3(9):412, 1959.
- [Cow62] R. A. Cowley. Temperature Dependence of a Transverse Optic Mode in Strontium Titanate. *Physical Review Letters*, 9(4):159, 1962.
- [Dav73] A. S. Davydov. The theory of contraction of proteins under their excitation. *Journal of theoretical biology*, 38(3):559, 1973.
- [DP06] T Dauxois and M Peyrard. *Physics of solitons*. Cambridge University Press, first edition, 2006.
- [GM12] R. Gross and A. Marx. *Festkörperphysik*. Oldenbourg Wissenschaftsverlag, first edition, 2012.

- [HM01] H.-Y. Hao and H. Maris. Experiments with acoustic solitons in crystalline solids. *Physical Review B*, 64(6):064302, 2001.
- [KH07] K. Kopitzki and P. Herzog. *Einführung in die Festkörperphysik*. Lehrbuch Physik. Vieweg+Teubner Verlag, 2007.
- [KS75] J. A. Krumhansl and J. R. Schrieffer. Dynamics and statistical mechanics of a one-dimensional model Hamiltonian for structural phase transitions. *Physical Review B*, 11(1):3535, 1975.
- [KSMS73] J. K. Kjems, G. Shirane, K. A. Müller, and H. J. Scheel. Soft-Phonon Response Function: Inelastic Neutron Scattering from  $\text{LaAlO}_3$ . 8(3):1119, 1973.
- [KTS07] A. Koreeda, R. Takano, and S. Saikan. Second Sound in  $\text{SrTiO}_3$ . *Physical Review Letters*, 99(26):265502, 2007.
- [KZ02] VM Karpan and Y Zolotaryuk. Discrete kink dynamics in hydrogen-bonded chains: The one-component model. *Physical Review E*, 66(6):066603, 2002.
- [KZ04] V. M. Karpan and Y. Zolotaryuk. Discrete kink dynamics in hydrogen-bonded chains: The two-component model. *Physical Review E*, 70(5):056602, 2004.
- [LL90a] L. D. Landau and E. M. Lifschitz. *Elektrodynamik der Kontinua*. Akademie-Verlag Berlin, 1990.
- [LL90b] L. D. Landau and E. M. Lifschitz. *Statistische Physik Teil I*. Akademie-Verlag Berlin, 1990.
- [LR80] M. C. Lawrence and G. N. Robertson. Estimating the barrier to proton or deuteron tunnelling in hydrogen-bonded crystals. *Ferroelectrics*, 25(1):363, 1980.
- [LR05] B. Leimkuhler and S. Reich. *Simulating Hamiltonian Dynamics*. Cambridge University Press, 2005.
- [PF87] M. Peyrard and N. Flytzanis. Dynamics of two-component solitary waves in hydrogen-bonded chains. *Physical Review A*, 36(2):903, 1987.
- [RAT07] K. M. Rabe, C. H. Ahn, and J. M. Triscone. *Physics of ferroelectrics: a modern perspective*. Springer Berlin Heidelberg, 2007.
- [SASR72] S. M. Shapiro, J. D. Axe, G. Shirane, and T. Riste. Critical Neutron Scattering in  $\text{SrTiO}_3$  and  $\text{KMnF}_3$ . *Physical Review B*, 6(11):4332, 1972.
- [SCL00] J. F. Scott, A. Chen, and H. Ledbetter. The myth of second sound in strontium titanate. *Journal of Physics and Chemistry of Solids*, 61(2):185, 2000.

- [Sco92] A. Scott. Davydov's soliton. *Physics Reports*, 217(1):1, 1992.
- [Sko10] C. Skokos. *The Lyapunov Characteristic Exponents and Their Computation*, volume 790 of *Lecture Notes in Physics*. Springer Berlin Heidelberg, Berlin, Heidelberg, 2010.
- [SNM66] G. Shirane, R. Nathans, and V. J. Minkiewicz. Temperature Dependence of the Soft Ferrelectric Mode in KTaO<sub>3</sub>. *Phys. Rev.*, 157(2):157, 1966.
- [SS78] T. Schneider and E. Stoll. Molecular-dynamics study of a three-dimensional one-component model for distortive phase transitions. *Physical Review B*, 17(3):1302, 1978.
- [SZ91] A. V. Savin and A. V. Zolotaryuk. Dynamics of ionic defects and lattice solitons in a thermalized hydrogen-bonded chain. *Physical Review A*, 44(12):8167, 1991.
- [vCD10] P. J. S. van Capel and J. I. Dijkhuis. Time-resolved interferometric detection of ultrashort strain solitons in sapphire. *Physical Review B*, 81(14):144106, 2010.
- [ZPS91] A. V. Zolotaryuk, S. Pnevmatikos, and A. V. Savin. Two-sublattice kink dynamics and ionic defects in hydrogen-bonded chains. *Physica D: Nonlinear Phenomena*, 51(1-3):407, 1991.
- [ZPS00] A. V. Zolotaryuk, M. Peyrard, and K. H. Spatschek. Collective proton transport with weak proton-proton coupling. *Physical Review E*, 62(4):26, 2000.

# Declaration of Authorship

I, Matthias Gohlke, declare that the work presented here is, to the best of my knowledge and belief, original and the result of my own investigations, except as acknowledged, and has not been submitted, either in part or whole, for a degree at this or any other University.

Formulations and ideas taken from other sources are cited as such.

Location, Date:

---

Signature:

---